LIQUID ATOMIZATION FOR AEROSOL APPLICATIONS

by

Tingbao Chen
B.Eng., Beijing Agricultural Engineering University, 1983

A Thesis Submitted in Partial Fulfillment of the
Requirements for the Degree of
MASTER OF APPLIED SCIENCE
in the
Department of Mechanical Engineering.

We accept this thesis as conforming
to the required standard

[redacted]

Dr. Xianguo Li, Supervisor (Department of Mechanical Engineering)

[redacted]

Dr. Allan Doige, Departmental Member (Department of Mechanical Engineering)

[redacted]

Dr. James Haddow, Departmental Member (Department of Mechanical Engineering)

[redacted]

Dr. Rolf G. Lueck, Outside Member (School of Earth and Ocean Sciences)

© TINGBAO CHEN, 1997

University of Victoria

All rights reserved. This thesis may not be reproduced in whole or in part, by
photocopy or other means, without the permission of the author.

QC882
C46

Supervisor: Dr. Xianguo Li

Abstract

Liquid atomization from pressure-swirl atomizers has been investigated experimentally in order to establish the possibility of using pure water solution as a substitute for hydrocarbon propellants for aerosol applications, because of environmental concerns and poor spray performance of the present products.

It is shown that the pressure-swirl nozzle alone is not adequate in meeting the atomization requirements for aerosol applications at low injection pressures. Studies have also been carried out for external acoustic excitations exerted on the baseline pressure-swirl nozzle. It is found that the acoustic effect on the disintegration of the conical liquid sheet is observable by flow visualization techniques and measurable by phase Doppler particle analyzer (PDPA), however, the reduction of droplet sizes from PDPA measurements is not significant. Furthermore, considerable variations of droplet diameters along the radial and axial directions have been measured.

To achieve better performance such as spray symmetry, spray penetration and smaller droplets, modified pressure-swirl atomizers with different insert geometry have been designed and the effect of external acoustic disturbances have also been investigated. More symmetrical spray pattern and some reduction of droplet sizes are achieved and more visible disturbance waves on the liquid sheet are observed. Investigations on both the baseline pressure-swirl nozzle and the modified pressure-swirl atomizers still show difficulties in meeting Johnson's droplet size requirement at low injection pressures without chemical additives.

A new-concept atomization technique has been developed for aerosol applications and a dramatic reduction in droplet sizes and almost complete spatial uniformity of mean droplet diameters has been achieved. The line-averaged mass mean diameter of droplets (which is the key parameter that Johnson expects) in the spray produced by the new-concept impaction atomizer is about 45 μm, a value meeting Johnson's specification of 50 μm or less. The maximum variation of the droplet mass mean diameter in the whole spray is less than 5 μm, under the specified injection pressure of 0.4 MPa (60 psi). On the other hand, the variations of the droplet mass mean diameter are more than 20 μm for sprays produced by both the baseline and the modified pressure-swirl nozzles measured at the axial locations of 203.2 mm (8 inches) downstream of the nozzle. However, the impaction atomization results in significant amount of liquid dripping-off, which is not atomized. Preliminary analysis indicates that either using the Venturi tube or simply the hand-pump pressurization system, the dripping fluid of the new-concept impaction atomizer can be recirculated or reutilized completely. A prototype of the impaction atomizer has been designed and

built in house, that fits onto the existing aerosol products. It is foreseen that the impaction atomizer could become a new atomization system for aerosol applications with quality spray performance but no negative environmental impact.

Examiners:

[redacted]

Dr. Xianguo Li, Supervisor (Department of Mechanical Engineering)

[redacted]

Dr. Allan Doige, Departmental Member (Department of Mechanical Engineering)

[redacted]

Dr. James Haddow, Departmental Member (Department of Mechanical Engineering)

[redacted]

Dr. Ron G. Laeek, Outside Member (School of Earth and Ocean Sciences)

Table of Contents

List of Tables

List of Figures

Nomenclature

a	radius of minor axis of ellipsoid (mm)
A_{p_i}	probe area at point i
b	radius of major axis of ellipsoid (mm)
b_n	constant in Fourier series expansion
c	speed of light waves (m/s)
d	liquid jet diameter (mm)
dr_i	distance between point i and $i+1$ along radial direction (mm)
D	droplet diameter (μm)
D_{10}	mean diameter (μm)
D_{20}	area mean diameter (μm)
D_{30}	mass mean diameter (μm)
D_{32}	Sauter mean diameter (μm)
$\overline{D_{30}}$	line-averaged mass mean diameter (μm)
$\overline{D_{32}}$	line-averaged Sauter mean diameter (μm)
D_{20_i}	measued D_{20} at point i (μm)
D_{30_i}	measured D_{30} at point i (μm)
d_i	nozzle orifice diameter (mm)
d_L	diameter of the laser beam (mm)

d_t	diameter of unfocused laser beam (mm)
E_s	potential surface energy
f_a	acoustic frequency (Hz)
f_L	focal length of transmitter lens (mm)
f_s	signal frequency from the photodetector (Hz)
κ	dimensionless axial wave number, $\kappa = \pi d/\lambda$
L_p	sound decibels
m_0	mass of one single droplet before impaction
m_1, m_2	masses of two objects
m_i	mass of the ith droplet after impaction
m_s	mass of the amount of liquid un-atomized after impaction
M	total number of droplets after impaction
n	tangential wave number
$\mathbf{n}$	unit vector
N	total number of data points along radial direction
N_f	number of fringes
N_i	validated droplet number counts at point i
p	injection pressure (Pa)
r	radius of the liquid jet (mm)
R_e	Reynolds number
s	beam separation at transmitter lens (mm)
t	time (s)
t_i	elapsed measurement time at point i (s)
u	velocity (m/s)
u_p	paticle velocity
$\mathbf{u}$	velocity vector

$\mathbf{u_1}, \mathbf{u_2}$	velocity vectors of two objects before collision
$\mathbf{u_1'}, \mathbf{u_2'}$	velocity vectors of two objects after collision
U_1, U_2, U_3	high voltages of photodetectors (V)
W_e	Weber number
w_i	weighting factor for line-averaging
x, y, z	coordinate axes
Z	Ohnesorge number

Greek Symbol

α	angle of the laser beam intersection
β	dimensional factor
δ	fringe spacing
λ	wave length
ω, Ω	dimensionless wave growth rate
Φ_{i-j}	phase difference between ith and jth photodetectors
ρ_g	gas density (k_g/m^3)
ρ_ℓ	liquid density (k_g/m^3)
σ	surface tension (N/m)

Acknowledgements

I would like to express my deepest thanks to Dr. Xianguo Li who gave me encouragement, instruction and academic advice in the first place and gave me financial support for my completion of this thesis. His sincere help and friendship will be beneficial to me for the rest of my life.

I would also like to thank Lily Wang, my sister-in-law, who supported me financially and spiritually. Her encouragement and advice are appreciated greatly.

Rodney Katz's help with the design and construction of the experimental devices is gratefully acknowledged.

Finally, I'd like to address my thanks to Mr. Hongzhi Guo, ex-president of BESTOC Machine Inc. in China, who gave me sincere help during my stay there.

To my parents and my wife

who have been always standing behind me to give me support when I need it.

This is also a special gift dedicated to my cute little son, Jeffrey.

Chapter 1

INTRODUCTION

Aerosol space spray products such as room air fresheners are consumer products with extensive daily usage. The aerosol spray is usually generated by using chlorofluorocarbon (CFC) propelled systems to achieve consumer acceptable spray characteristics, such as droplet diameters, spray cone angles and spray penetrations, under strict design and operating conditions. In 1978, the U. S. Environmental Protection Agency, Food and Drug Administration and Consumer Product Safety Commission banned the use of CFC as propellant for aerosol spray products because they were believed potential contributor to ozone depletion and air pollution. After that, virtually all American aerosols are believed CFC-free but the manufacturers still have to use hydrocarbon compounds as additives to achieve consumer acceptable spray performance. However, the hydrocarbon additives are still believed to be air polluters, and environmental concern dictates the use of non-hydrocarbon propellants for the space spray products, preferably the direct use of liquid water solution. However, liquid water has much higher values of surface tension, resulting in relatively large liquid droplets being produced in the spray. In addition, the volatility of liquid water is much lower than that of hydrocarbons. The combination of large droplet sizes and

low volatility leads to long liquid droplet lifetime, during which the large droplets may fall onto floor/carpet due to gravity effect, creating unacceptable performance of the aerosol products. Because the surface tension and volatility of water are its physical properties, they can not be changed without adding to it chemical substances such as hydrocarbon compounds which are undesirable. On the other hand, the problem associated with high surface tension and low volatility may be resolved if, by proper atomizer structure design and operation of liquid atomization processes, sufficiently small droplets are produced. Because droplet lifetime is dependent on the droplet surface area, which is proportional to the square of droplet diameter, a reduction in droplet diameter will decrease significantly the droplet lifetime, hence the amount of rain fallout. Clearly, the droplet diameter is one of the key parameters in measuring the spray characteristics and aerosol product performance.

1.1 Background and Literature Review

The purpose of liquid atomization and spray formation is to increase the liquid surface area for a given amount of liquid mass such that the subsequent mass transfer processes (such as evaporation of spray droplets) can be significantly enhanced. In practice, there are variety of ways to generate liquid atomization and sprays [1]. However, due to the specific requirements and constraints of Johnson's aerosol space spray products, it had been agreed upon during the two meetings held in Johnson's premises on June 20 and October 1, 1994 that the best possible atomization configuration for Johnson's aerosol applications is the pressure-swirl atomization as well as other possible solutions. Because of practical and safety consideration, the technique for droplet size reduction by increasing injection pressure has been ruled out. Therefore, pressure swirl atomization with a limited injection pressure is NOT adequate in meeting the

performance requirements of aerosol products.

Fundamentally, for pressure-swirl atomization the liquid, upon exiting the atomizer, forms a hollow-cone liquid sheet due to the centrifugal motion developed in the swirling chamber of the atomizer. The conical liquid sheet so formed is unstable to interfacial disturbances, which is often known as the Kelvin-Helmholtz instability (Squire [2]; Li and Tankin [3]; Jazayeri and Li [4]). This instability is convective in nature [5], meaning that the disturbance amplitude increases as the instability propagates in the downstream direction much like the wave motion. When the disturbance amplitude reaches certain critical value, the continuous liquid sheet breaks up into discrete forms at approximately half wavelength interval (Dombrowski and Johns [6]; Jazayeri and Li [4]), the discrete pieces of liquid contract, under the influence of surface tension, into ligaments. The ligaments thus formed are unstable to disturbances (which may be referred to as secondary instability) and further break up into individual parcels of liquid at one wavelength interval. These parcels of liquid then contract into individual droplets due to surface tension effect. The secondary instability mentioned above is often referred to as Rayleigh instability (Rayleigh [7]). Therefore, the diameter of droplets formed in this process is related to the ligament diameter and wavelength of secondary Rayleigh instability, both of these are in turn connected with the liquid sheet thickness and wavelength of the primary instability on the liquid sheet. In principle, the droplet diameter can be reduced by using a smaller atomizer opening. However, a small atomizer flow passage will incur excessive pressure loss, which limits the amount of liquid flow rate, and high tendency of atomizer clogging. Typically, atomizer diameters are in the range of a fraction of 1 mm, leaving practically not much room for further reduction.

However, the liquid sheet is inherently unstable for a range of wavelengths, droplet sizes in a spray tend to be controlled by the dominant wavelength at which the dis-

turbance growth rate is a maximum. But because the liquid sheet instability is convective, it complies well with the externally imposed disturbances. That is, the frequency or wavelength of the disturbances on the liquid sheet will be equal to that of the external disturbances (or excitations). Therefore, the droplet sizes can be controlled by the wave frequency (which is inversely proportional to the wavelength) of the externally-induced disturbances. In principle, the higher the frequency, the smaller the droplets would be, provided that the frequency is in the unstable range of the liquid sheet instability. The unstable frequency (or wavelength) range is dependent on the liquid flow conditions (typically liquid velocity or liquid flow rate), atomizer structures (especially atomizer diameter), and physical properties of the atomizing liquid and surrounding gas medium. Therefore, the optimal external disturbances (amplitude and frequency) for a given liquid to be atomized will be a function of liquid flow conditions and atomizer structures, and an appropriate combination of external disturbances and atomizer structures will be required to achieve certain desired spray characteristics for a given kind of liquid and given amount of flow rate.

The external disturbances can be generated by ultrasonic devices such as those driven by piezoelectric systems. This technique has been used for the generation of monodisperse sprays (e.g., Berglund and Liu [8]; Warnica, et al. [9]). Ultrasonic atomizers have also been developed for low fuel flow rates particularly suited for domestic oil burners (Young, et al. [10]; Locklin [11]). More recent work on sprays under piezoelectric-induced disturbances has been carried out by Takahashi, et al. [12] and Dressler and Anderson [13]. On the other hand, external excitation can also be induced by acoustic devices such as loudspeakers (Rutland and Jameson [14]), which is relatively simple and easy for both design and operation of the disturbance generation system and atomizer assembly.

It should be pointed out that the liquid sheet breakup process, especially close to the breakup region, is highly nonlinear, depending on the evolution of wave motion, the interaction among various wave elements, and the initial disturbances (amplitudes and frequencies). The initial disturbances may originate from inside the atomizer itself, such as liquid turbulence, cavitation, or even molecular motion, and can in no way be known in practice. Generally, initial disturbances may possess various values of amplitudes and frequencies, leading to random-like and chaotic droplet formation processes, and broad size distributions of the subsequently formed droplets. Therefore, external disturbances should be sufficiently strong in order to overshadow the growth of internally-generated disturbances and become predominant influence. Because both internal and external disturbances grow with downstream distances, monodisperse sprays are usually achieved for relatively low liquid velocities, and practical sprays typically exhibit distributions of droplet sizes over a wide diameter range. Hence some average diameter, such as mass mean diameter, is often used to describe and evaluate practical sprays. In addition, liquid sheet breakup occurs at about half-wavelength interval preceding the droplet formation, the subsequently formed droplets tend to be concentrated in packets (or clusters), thereby making the spray structure unsteady and nonuniform both spatially and temporally. Therefore, droplet sizes are usually measured in (i) time-resolved manner (instantaneous measurements); (ii) spatially-resolved manner (point measurements); (iii) time-averaged measurements; (iv) spatially-averaged measurements; and (v) both time- and spatially-averaged measurements. Therefore, care must be taken when comparison is made for droplet sizes measured by different techniques and instrumentations. For example, the laser diffraction-based measurements (typical Malvern Particle Analyzer, or SYMPA TEC's HELOS Particle Analyzer) yield both temporally- and spatially-averaged results (i.e., average results for all droplets within the laser beam during the interval of measurements), whereas the phase Doppler-based equipment

(such as Phase Doppler Particle Analyzer from Aerometrics and Particle Dynamics Analyzer from Dantec) provides spatially-resolved and time-averaged results. Hence, a direct comparison may not be made for results measured by different techniques and instrumentations, often convoluted data analysis, processing and conversion must be employed if such comparison is absolutely necessary. However, good care must be taken of the choice of data conversion technique and during the data conversion processes.

1.2 Objectives and Thesis Outline

As discussed earlier, the pressure-swirl atomization alone is not adequate in meeting the performance requirements of Johnson's aerosol space spray products without using hydrocarbon propellants. Therefore, some other mechanism must be added onto the base mechanism of pressure-swirl atomization, or other possible atomizer designs, in order to achieve the desired spray characteristics. The present project, based on the fundamental liquid sheet instability mechanism discussed earlier, decided to explore the technique of external acoustic excitations of the conical liquid sheets produced by various atomizers of different design and structure. Consequently, the present project conducts experimental investigations on the liquid atomization processes and spray characteristics and on the various effects, such as atomizer design and external excitations, on the liquid atomization processes and spray characteristics. Eventually, it is aimed that these investigations would provide sufficient information on liquid atomization and spray characteristics such that a new atomizer design would result, which can achieve, by using compressed air propellant, far smaller droplet sizes and equivalent performance levels than Johnson's aerosol space spray products using hydrocarbon propelled systems.

In this thesis, the fundamental aspects of liquid atomization is studied with respect to different atomizer designs and different techniques applied. The baseline pressure-swirl nozzle is investigated together with application of external acoustic excitations. Based on the results of the baseline pressure-swirl nozzle, modified pressure-swirl atomizers with different insert structures are developed and investigated. External acoustic effect is also investigated on the modified pressure-swirl atomization. It is shown that the external acoustic excitations do have effect on the atomization process. Improvement of the spray characteristics is achieved by the modified pressure-swirl atomizers. But significant reduction of droplet diameters has not yet been verified by PDPA measurement for both the baseline and modified pressure-swirl atomizers plus external acoustic excitations.

Based on the concept that the liquid momentum change by impacting on a solid surface can create liquid spray, a new-concept impaction atomizer is developed and studied in order to achieve the droplet diameter reduction with acceptable spray angles and penetrations. The effect of impaction angle and impaction length is studied with theoretical analysis and experimental investigations. A prototype of the new-concept impaction atomizer is also designed and made in house. This new-concept impaction atomization technique gives dramatic reduction in droplet sizes and complete spray uniformity is achieved, compared to those sprays generated by the pressure-swirl atomizers. The dripping fluid created by the new-concept impaction atomizer can be completely recirculated or re-utilized by either the Venturi tube design or simply the hand-pump pressurization system for aerosol applications. Therefore it may be the best substitute for the atomization system of Johnson's aerosol space spray products with quality spray performance but no negative environmental impact.

Chapter 2

EXPERIMENTAL APPARATUS AND INSTRUMENTATION

The overview of experimental apparatus is schematically shown in Figure 2.1. The nozzles used in this experiment are pressure-swirl nozzles (including the modified pressure-swirl nozzles) and the new-concept impaction atomizers. The detailed structures of these atomizers will be respectively described later in the relevant chapters.

2.1 Fluid Delivery System

The liquid delivery system consists of a water supply and collection devices. The supply water in the water tank is pressurized by compressed air and delivered to the nozzle assembly. To keep the pressure steady, a pressure regulator is used such that during any runs of measurement, the pressure fluctuation is kept less than 1%. Also for safe operation, a pressure relief valve is installed in the water tank. Since tap water is used as the atomization liquid, filtering devices are used to prevent the

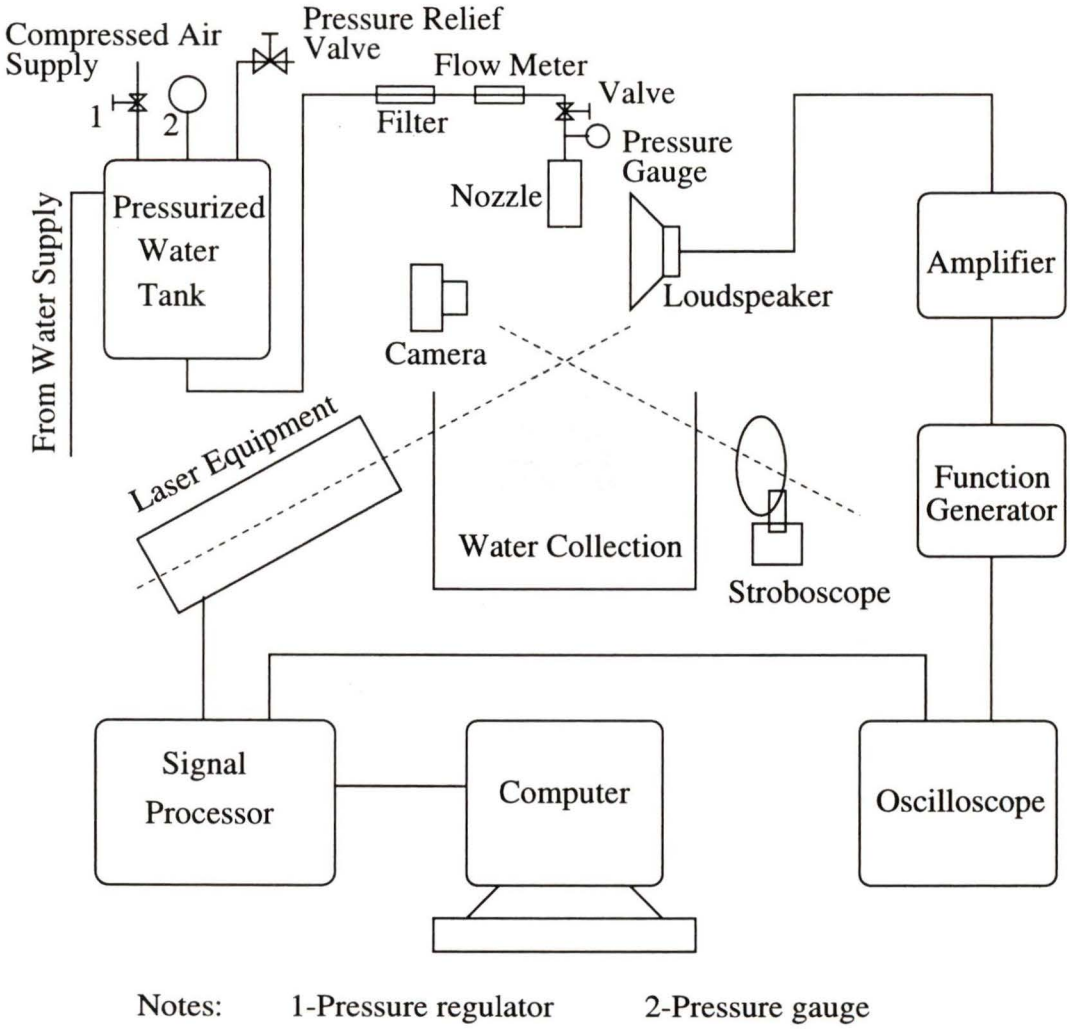

Figure 2.1: Experimental set-up.

nozzle from clogging. Due to friction effect, especially in the water filter, the pressure loss in the water supply line is not negligible. Thus in addition to the pressure gauge in the water tank, a second gauge is installed close to the atomizer to monitor the injection pressure within the required range. The water collection tank is made of plexiglas, and the nozzle as well as the spray is surrounded by a large plexiglas box to prevent the laser system, especially the transmitting and receiving optics, from wetting. Care has been taken that there are no droplets hitting and accumulating on the plexiglas wall such that the scattered lights by the spray particles (reflection and refraction lights) are not interfered.

2.2 Acoustic System

Theoretical studies show that the breakup mechanism of liquid jets or sheets is dominated by a process of the rapid growth of disturbances. Rayleigh [7] first introduced into a cylindrical liquid jet infinitesimal disturbances and found that some of the disturbances damp the wave growth rate but some of them enhance the wave growth rate and the fastest growing disturbances dominate the process and eventually lead to breakup. But Rayleigh's results are relevant only to the case of small values of the Weber number. For a Weber number of order one or greater than one, new faster growing disturbances of much larger wavelengths than those of the Rayleigh mode have been reported by Leib and Goldstein [15][16]. Other researchers [17] observed that the disturbances not only grow temporally but also grow spatially. A number of theories on the mechanism of liquid jet or sheet breakup processes are available, but not many experimental studies have been conducted, partly due to the co-existence of various modes of disturbances leading to difficulties in experimental observation. One of the important tasks of this study is to utilize external acoustic excitations

as disturbances imposed on the spray produced by pressure-swirl atomizers in order to achieve a certain degree of performance of the liquid atomization. The external disturbances are produced by an acoustic signal generation system. It includes a function generator (Wavetek 4 MHz, model 187) for providing different initial electrical signals. The amplifier (NAD stereo amplifier 3240 PE) enhances the electrical signals to a certain desired power output level before driving a loud speaker (6" $\times$ 9" coaxial horn), which is positioned close to the nozzle exit to create perturbations on the conical liquid sheet surface. The electrical signals used in this investigation from the function generator and after the amplifier are sinusoidal, and these signals are also monitored on an oscilloscope (Tektronix 7854). When the amplifier output is high, some distortions of the signal wave forms are observed, probably partly due to the speaker loading and partly due to clipping by the amplifier.

2.3 Instrumentation

2.3.1 Flow Rate Measurement

Since the liquid flow rate is very low in this experiment ($\leq$ 1 $m\ell/s$), no flow meter was available in the laboratory. It was therefore necessary to collect the spray water within a certain period (about 5 minutes) and then measure the liquid volume. Since the room temperature is around 20^o (the laboratory temperature being centrally controlled), the final error for the calculation of liquid flow rate is then negligible.

2.3.2 Visualization Techniques

The overall flow field characteristics are investigated by flow visualization techniques which consist of photography and video. Observations show that both the lighting

and the visualization devices are very important, even the method for visualization plays an important role in the measurements.

Photography

Photographic observations in this experiment are made by using backlighting provided by a stroboscope (STROBOTAC 1531-AB), as shown in Figure 2.1. A photographic camera (PENTAX K1000 SE) is mounted opposite to the stroboscopic light source for picture taking. Electrical connections are made between the stroboscope and the camera shutter, such that when the shutter is released, the stroboscope will emit one pulse of light (one flash) to illuminate the spray. To obtain more uniform illumination and clearer pictures, a piece of semi-opaque glass is placed between the stroboscope and the spray. The synchronized backlighting integrates the light scattering effect of all the droplets in the spray, thus capturing essentially all the spray characteristics on photographic film. The light pulse duration for each flash is short, in the order of a few microseconds, thus essentially freezing the droplet motion, and showing the instantaneous spray characteristics. This is clearly shown in the photographs obtained, some of which are presented later in relevant chapters. The camera uses PENTAX-A ZOOM lens (1:3.5~4.5, 28~80 mm) with +1 to +7 close-up filter lens combinations. Kodak Tri-X pan black-and-white film (ASA 400) is used to record the spray images with sufficient spatial resolution (as will be seen from the photographs presented in later chapters), and Kodak polycontrast III RC paper and Kodak D-76 developer and Kodak fixer are used for developing the final photographs.

Video

A X12 two-speed power zoom Panasonic video camera (X12 optical lens 5.4-64.8 mm) is also used for spray visualization. As mentioned before, the images captured by the

standard video camera are limited in both spatial and temporal resolutions leading to the loss of some spray pattern information, as it is viewed by slow speed replay. But qualitatively the overall characteristics of the spray can be obtained. For a single droplet stream produced by the single droplet generator (A special nozzle with a small orifice opening of 76.2 μm (0.003 in.) diameter to create single uniform droplets for PDPA calibration. This will be discussed later in the laser equipment calibration section), clear long-wave-length wave motion of the droplet stream was captured under acoustic excitation which is difficult to catch by photographs, because the photographic images are limited in their field view for such small and dynamic particles. Therefore, video and still photographic images are complementary in revealing spray structure and dynamics.

2.3.3 Phase Doppler Particle Analyzer (PDPA)

Overview

The droplet diameter and velocity of the spray are measured simultaneously by a one-component Phase Doppler Particle Analyser (PDPA), also referred to as Particle Dynamic Analyzer (PDA), which is very similar to a conventional laser Doppler velocimeter (LDV) except that three photo-detectors are used in the receiver unit, as shown in Figure 2.2. This PDPA system is a non-contact non-intrusive measuring device which has many advantages over the conventional measurement techniques (hot-wire anemometry, pitot tube, etc.), and is becoming the standard instrument for spray measurements.

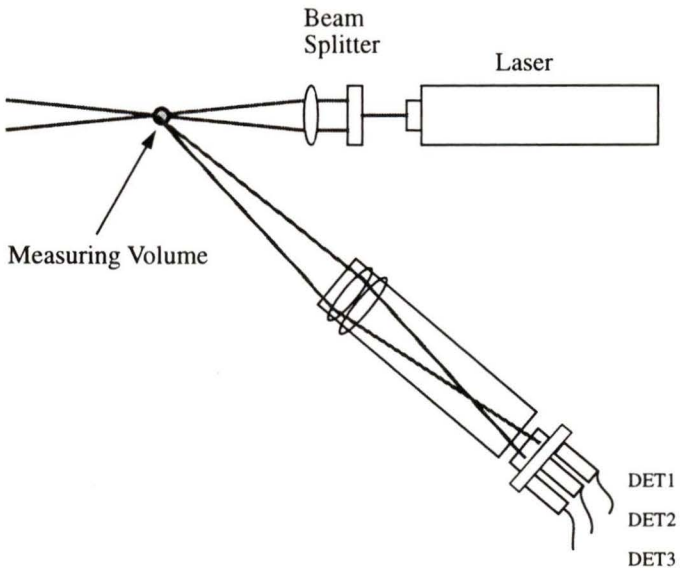

Figure 2.2: Schematic of Phase Doppler Particle Analyser system.

Principles of Operation

The principles of PDPA can be described by two models: the fringe or light interference model and the phase Doppler model. Both models give the same results for droplet diameter and velocity calculations. The fringe model is easier to understand, however, it can not be used to describe all the aspects of the equipment[18][19].

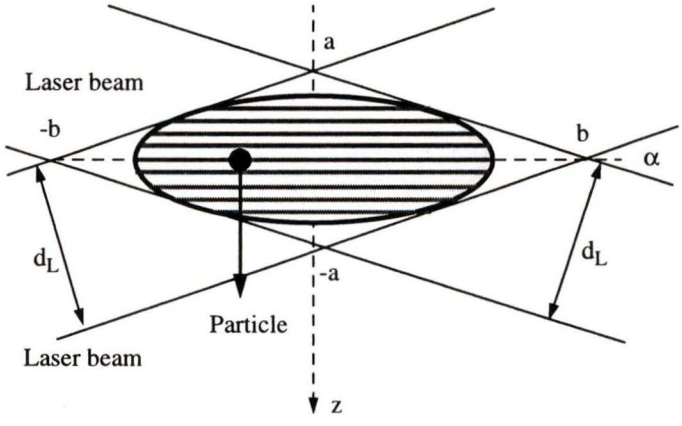

Figure 2.3: Fringe pattern formed by two crossing laser beams.

i) Fringe Model

The most common Phase Doppler Particle Analyser uses dual beam system. The transmitting optics of PDPA split the laser beam into two parallel light beams of equal intensity that are focused to cross at the point where measurements are taken. The crossing point of the two beams is often referred to as measuring volume. The measuring volume thus formed is a three-dimensional ellipsoid. Its major axis (or the ellipsoid length) is $2b$ shown in Figure 2.3. Its minor axis (or the ellipsoid diameter because of its circular cross section) is $2a$. Since the laser produces coherent light, the two beams will interfere with each other at the intersection point such that bright and dark fringes are formed. The constructive interference of the lights forms bright fringes and deconstructive interference forms dark fringes [20], as shown in Figure 2.3. The fringe spacing (distance between two adjacent fringes) is given by [20]:

$$\delta = \frac{\lambda}{2\sin(\alpha/2)} \tag{2.1}$$

where λ is the wave length of the laser beam which is 632.8 μm for Dantec Model PDA N10 55X57 [21], and α is the angle of the laser beam intersection which can be easily measured and adjusted.

The velocity of the particles passing through the measuring volume can be calculated from the fringe spacing divided by the time taken for the particle to travel from one fringe to another. This time can be calculated from the frequency of the signal detected by the photodetector from the light signal scattered by the particle (There are three scattering regions: forward scattering ($10^o \sim 50^o$); backward scattering ($130^o \sim 170^o$); and at 90^o location [22]). Thus the particle velocity can be expressed by

$$u_p = \frac{\delta}{t} = \frac{f_s\lambda}{2\sin(\alpha/2)} \tag{2.2}$$

where u_p is the particle velocity normal to the fringe plane, and f_s is the signal frequency from the photodetector.

The velocity measured through the measuring volume in which the fringes are formed by two laser beams with the same frequency will be correct in magnitude but the direction of particle motion will be ambiguous because the fringes so formed are stationary. This ambiguity problem is resolved by introducing a frequency shift which is basically the phase Doppler model. In Dantec PDPA, Model 57X10, a frequency shift of 40 MHz is produced by a Bragg cell.

The particle diameter is obtained by calculations of the scattered light signals from two photodetectors positioned at different locations. According to optical theory, the droplet diameter is proportional to the phase difference of signals from the two photodetectors and a third detector is needed to remove the phase ambiguity from the phase difference larger than 360^o.

ii) Phase Doppler Model

In 1842, Christian Doppler presented his famous paper "On the Colored Light of Double Stars". He first proposed in his paper the Doppler effect which is now widely used in many areas. The core of the Doppler theory is that if the light source and the observer are both at rest, then the observed and the emitted light frequencies are the same; if the observer moves towards the source, however, the light frequency will increase, and if he moves away it will decrease. With the Doppler effect, additional phenomena occur and they must be considered in practice. Figure 2.4 gives an example of a stationary observer recording a distance of the light wave emitted from a moving source travelling to observer. $\mathbf{u}$ is the velocity of the moving source and apparently the recorded distance by the stationary observer is $(c - \mathbf{u} \cdot \mathbf{n})t$, whereas for a stationary source, the equivalent distance is given by ct. Thus the wave length recorded from the moving source by the stationary observer is then:

$$\lambda' = \frac{c - \mathbf{u} \cdot \mathbf{n}}{f} \tag{2.3}$$

The corresponding wave frequency is:

$$f' = \frac{f}{1 - \frac{1}{c}(\mathbf{u} \cdot \mathbf{n})} \tag{2.4}$$

where c is the speed of the light waves, f the frequency, λ the wavelength and t the travelling time.

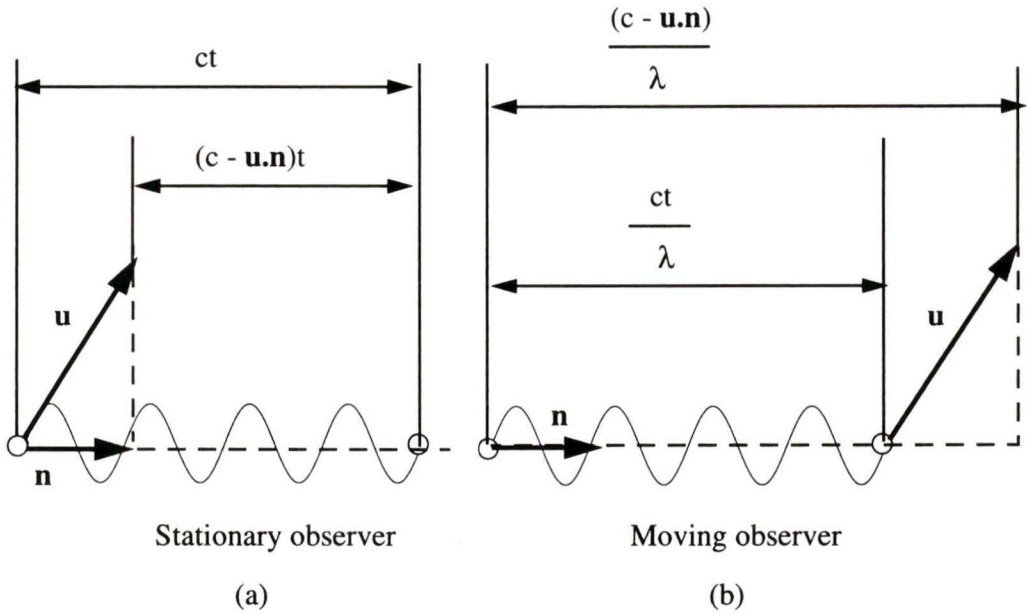

Figure 2.4: Doppler effect caused by a moving source and a moving observer.

The particle velocity and direction can both be determined by Doppler effect because both the particles (as receivers and transmitters of light waves) and the fringes are moving. If the particles are moving in the same direction as the fringes, the detected frequency of the scattered light signals will be lower, otherwise, it will be higher.

Since the droplet diameters are linearly related to the spatial frequency of the interference pattern produced by the scattered light (Figure 2.5), the droplet sizes can be accurately measured by the optical geometrical description [22]. The ambiguity caused by phase difference larger than 360^o can be avoided by using a third detector.

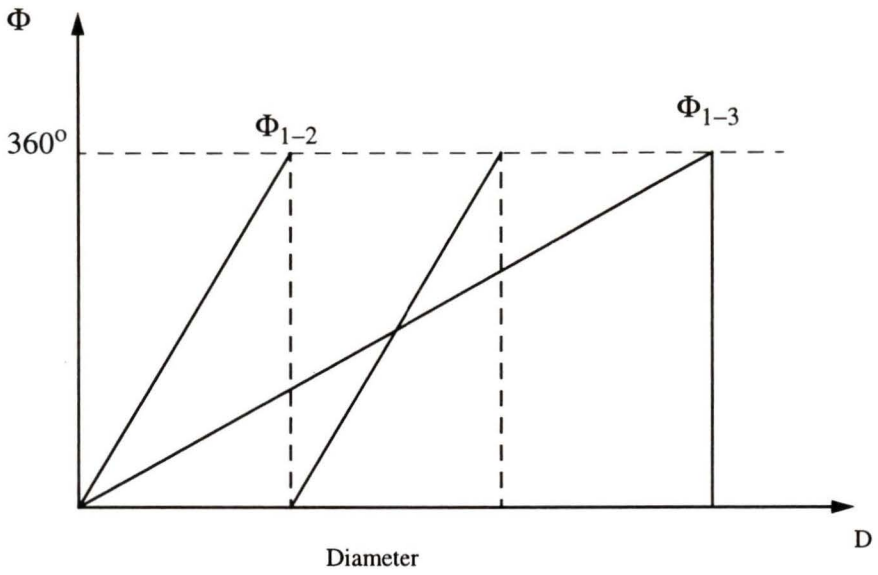

Figure 2.5: Detector phase responses.

Geometry of the Measuring Volume

The particle diameters and velocities are measured at the intersection of the two laser beams. As stated, this intersection (measuring volume or probe volume) is a three-dimensional ellipsoid. The geometry of this measuring volume and the parameters of the fringes inside this volume are given as follows [21] [22].

The ellipsoid length:

$$2b = \frac{d_L}{\sin \alpha} \tag{2.5}$$

The ellipsoid diameter:

$$2a = \frac{d_L}{\cos \alpha} \tag{2.6}$$

The fringe spacing:

$$\delta = \frac{\lambda}{2 \sin \alpha/2} \approx \frac{\lambda f_L}{s} \tag{2.7}$$

Number of fringes:

$$N_f = \frac{2a}{\delta} \tag{2.8}$$

Table 2.1: Parameters of the measuring volume of Dantec 57X10 PDPA

Wavelength of laser beam (λ)	632.8 nm
Diameter of unfocused laser beam (d_t)	1.0 mm
Focal length of transmitter lens (f_L)	310 mm
Beam separation at transmitter lens (s)	55 mm
Laser beam intersection angle (α)	10.14^o
Fringe spacing (δ)	3.5807 μm
Diameter of focused laser beam (d_L)	0.25 mm
Diameter of measuring volume ($2a$)	0.25 mm
Length of measuring volume ($2b$)	2.6 mm

where d_L is the diameter of the laser beam, α the beam intersection angle and λ is the laser beam wavelength; f_L is the transmitter lens focal length and s the beam separation at the lens.

The parameters of the measuring volume of Dantec 57X10 PDPA is listed in Table 2.1, from which the measuring volume dimension can be estimated, as given in the table.

Hardware Descriptions

The Dantec 57X10 PDPA system used in the present experiment is schematically shown in Figure 2.1. It is a single component system with Dantec transmitting and receiving optics operating in the backscatter mode (148^o). A 30 mW helium-neon laser supplies the coherent light source. The laser beam is split into two beams with the same intensity by a beam splitter. The beam separation is 55 mm and one beam passes through a Bragg cell where its frequency is shifted by 40 MHz. The parallel beams are focused at the measuring location in the flow field by a 79 mm diameter, 310 mm focal length achromatic lens. Scattered light from the laser beam intersection is collected by the receiving optics which has three photodetectors positioned at fixed

separations. The receiver uses a 79 mm diameter, 310 mm focal length lens and the collected light signals are converted by the photomultipliers to electrical signals with spatial frequencies linearly related to particle velocities and with phase differences are proportional to particle diameters. These electrical signals are then sent to the Dantec 58N10 PDA Signal Processor where the Doppler signals are processed. The processed data are transferred to an IBM computer using Dantec's SizeWare which controls the laser optics and collects the results of the spray measurements. An oscilloscope is also used to monitor the signal from the signal processor.

Traversing System

The traverse system was built with rigid 13 mm thick aluminum and used precision lead screws with anti-backlash nuts. The traverse has three-dimensional moving (x, y and z) ability with a travel of 600 mm, 350 mm and 270 mm in x, y and z directions, respectively. The coordinates of x, y and z are defined in Figure 2.6. The origin is located at the nozzle exit and the z axis coincides with the nozzle centerline and is positive in the flow direction. Each axis is equipped with a steel ruler to locate the laser beam intersection to the nearest millimeter. With a graduated dial on each axis, the measured location can be positioned with a resolution of 0.05 mm in the x direction and 0.013 mm in the y and z directions. This allows accurate positioning of the measuring locations in three dimensions and investigations of the characteristics of the spray can be carried out in the whole horizontal plane as well as in different vertical layers. The accuracy of the traverse movement was checked with a dial indicator and was generally better than 0.025 mm. The laser optics and the traverse were mounted on a wheeled table with lock ability such that the laser can be moved to anywhere necessary and be locked securely during measurement.

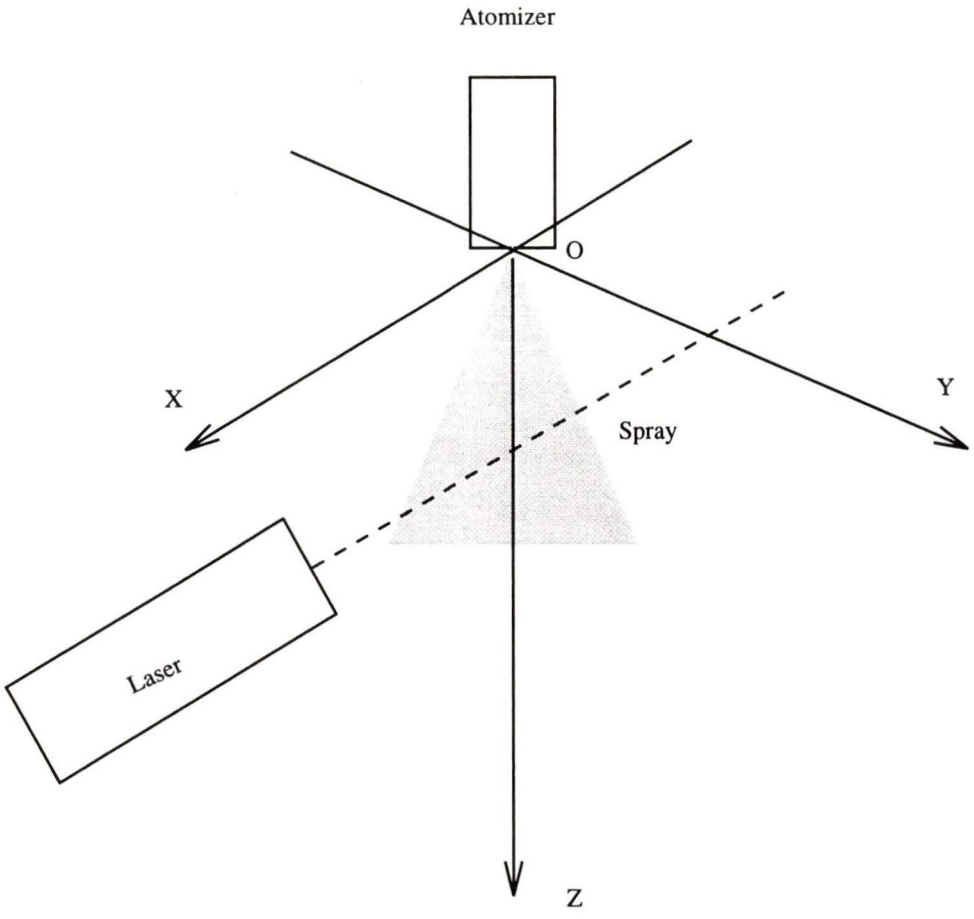

Figure 2.6: Reference coordinates.

Chapter 3

EXPERIMENTAL PROCEDURE

Because the liquid atomization is a complex process in which many factors are involved, care must be taken in every section of the experiment in order to obtain relatively steady and reliable results. In this chapter, detailed procedures of the experiment will be described.

3.1 Apparatus Set-up

Before proceeding to the measurements, careful alignment of the experimental apparatus has been conducted. This includes the water supply system, nozzle assembly, acoustic devices, and the laser equipment. For the liquid supply system, the water tank is a pressure vessel newly designed and made in house, it is flushed with water to ensure there is no dirt or metal dust left inside. Each time an experiment is finished, the tank is completely drained and the compressed air is used to blow it dry so that there is no chance of rust. For the nozzle assembly, every time when a measurement is finished, it is blown dry using compressed air because the brass filter

of the pressure-swirl nozzle is easy to get rusted. After a few measurements, it is cleaned by an ultrasonic cleaner to make sure that dirt or rust does not accumulate in the inner passage of the nozzle.

Since tap water is the liquid used in this experiment, there are minerals and foreign matter as well as charged particles in it. Care is taken on filtering, especially when the single droplet generator (SDG) is used to calibrate the laser equipment. The filter had to be replaced after a period of one month of experiment. During the laser equipment calibration, de-ionized water is used instead of tap water to get rid of the electrically charged particles. Besides an ordinary filter, a very fine stainless steel mesh (A-CX-325) is used right before the SDG's inlet to prevent the generator from clogging and to ensure the single droplet stream is steady. After each run of calibration, the SDG has to be cleaned using the ultrasonic cleaner.

The installation of the nozzle assembly is assured by the mounting plate which fastens together with two screws. The nozzle assembly also has two holes for fastening it to the mounting plate (See Figure 3.1). The nozzle is screwed into a connecting rod which connects to the water supply line (plastic hose). The connecting rod can be moved up and down and be locked at various heights to make the laser measuring volume located in a certain vertical location required from the nozzle exit. With the baseline pressure-swirl nozzle, the spray characteristics was investigated at the locations of 25.4 mm (1 inch) and 203.2 mm (8 inches), respectively, from the nozzle exit.

The Phase Doppler Particle Analyzer (PDPA) is the core part of the equipment as its correct functioning determines the accuracy of this experiment. As mentioned earlier, its alignment is very difficult and great care has to be taken. Even a very minor offset may cause a significant error. To align the transmitting and receiving optics into their right position, first the wheeled table and the laser mounting bench have

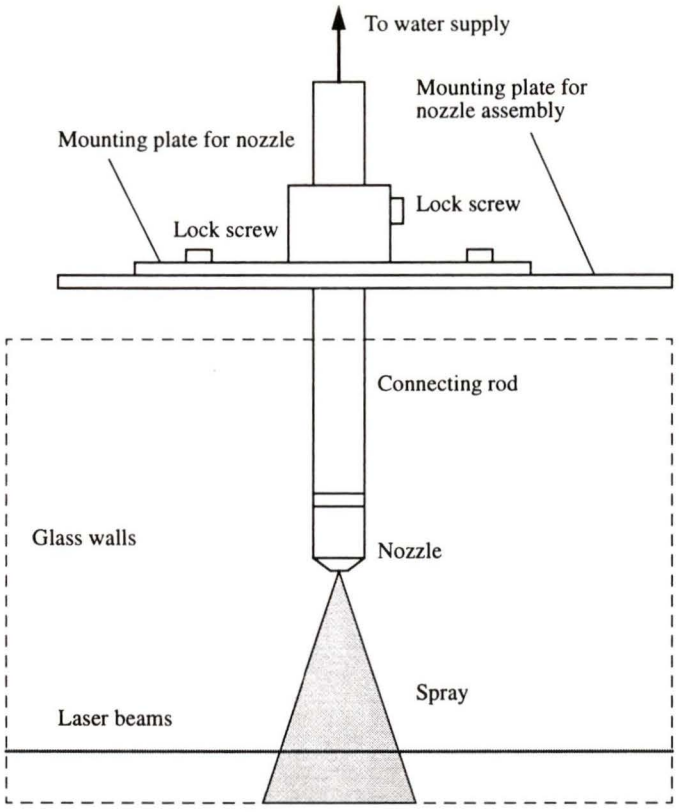

Figure 3.1: Alignment of the nozzle assembly.

to be completely horizontal, especially, the transmitting and receiving optics must be at the same horizontal level. As discussed earlier, off-axis backward scattering mode is used for this experiment. This gives more difficulties for the alignment. The backward scattering mode gives less intensity of the scattered light signal, it is not as easy as the forward scattering mode to align the optical devices. After the optics are leveled, the receiving optics is set at 150^{o} location. Fine adjustment of the receiver is made to get the crossing section of the laser beams to fall right at the crosshairs in the view finder. At the same time, strongest signal can be seen on the oscilloscope. To get the receiver perfectly focused, the crossing laser beams are watched through the view finder while the receiver lens is adjusted until clear image of the crossing beams is seen in the view finder. When the receiver lens is completely focused, the

image of the crossing laser beams in the view finder should be clear and symmetrical relative to the crosshairs (Figure 3.2). To achieve this, the oscilloscope can also be used as a monitor to observe whether all the signals from the three channels are clear or not. If the signal from any channel looks fuzzy, it means the receiver lens is not totally focused.

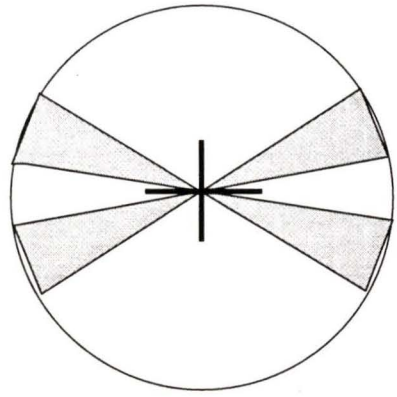

Figure 3.2: Focused laser beams in the view finder of the receiving optics.

Velocity measurement is not the key parameter in this experiment. But to obtain the best indication of reasonable measurement results, for example, using the velocity to confirm the flow rate obtained by collecting the spray water, the correct velocity values are needed. For this reason, the transmitting optics must be aligned correctly. Since the spray is flowing downwards, the main component of the velocity is vertically downward. Thus the fringe planes formed by the crossing laser beams has to be perpendicular to the flow direction (horizontal). To do this, the laser generator is rotated until the largest amplitude of signals on the oscilloscope is obtained.

3.2 PDPA Settings

Except the hardware of the laser operating system, there are many user-selected parameters that must be set when operating the PDPA system. During this experiment,

the priority was to set all the parameters as consistently as possible for all operating conditions. But unfortunately, different bandwidths which related to velocity measurements had to be used when the spray was measured at different vertical locations. At 25.4 mm (1 inch) from the nozzle exit, the velocity of the particles is higher than that at 203.2 mm (8 inches) down stream. Therefore, different bandwidths have to be chosen and it gives difficulties in measuring the droplet sizes with consistent results. It was observed that with larger bandwidth (which related to higher velocity range), the measured droplet size was larger as well. As some researchers [23][24] reported, it is possible to remove this discrepancy by increasing the high voltage of the photodetectors as much as possible. To do this, the high voltage was gradually increased until signal clipping occurred on the oscilloscope. Then the high voltages were slightly reduced. This may reduce the mass mean diameter deviation to less than 5% (see Table 3.1). But care must be taken that the velocity distribution should fill almost the full measurement range. Otherwise, the measured velocity no longer represents the real velocity of the spray. The sample size is chosen such that with the measurement reaching a steady state, the results are independent of sampling size, or statistically stationary (Figure 3.3). This assessment was done by using the modified pressure-swirl nozzle with an insert of 4 slots. The angle between the slot and the insert axis is 60^{o}. The nozzle housing was the original one of the existing pressure-swirl nozzle with a flow rate of 0.5 (g/s). From Figure 3.3, it is seen that after 30,000 of sample size, the deviation of the measured mass mean diameters from the average value is less than 1%. During all the measurements, the velocity and diameter ranges are chosen following the principle that the accepted samples represent almost the full range without signal clipping. The validated acceptance level achieved was over 85% while the spherical validation was over 90%.

Table 3.1: Bandwidth and high voltage effect on the measured diameters

Test #	Bandwidth	High Voltages (V)			D_{10}	D_{20}	D_{30}
	(MHz)	U1	U2	U3	(μm)	(μm)	(μm)
Run 1	4.0	1200	1304	1488	48.19	54.69	59.28
Run 2	12.0	1200	1304	1488	51.95	56.67	60.30
Run 3	12.0	1296	1400	1592	50.33	55.23	59.08
Run 4	36.0	1200	1304	1488	59.40	62.54	64.94
Run 5	36.0	1496	1624	1848	55.19	58.96	61.74

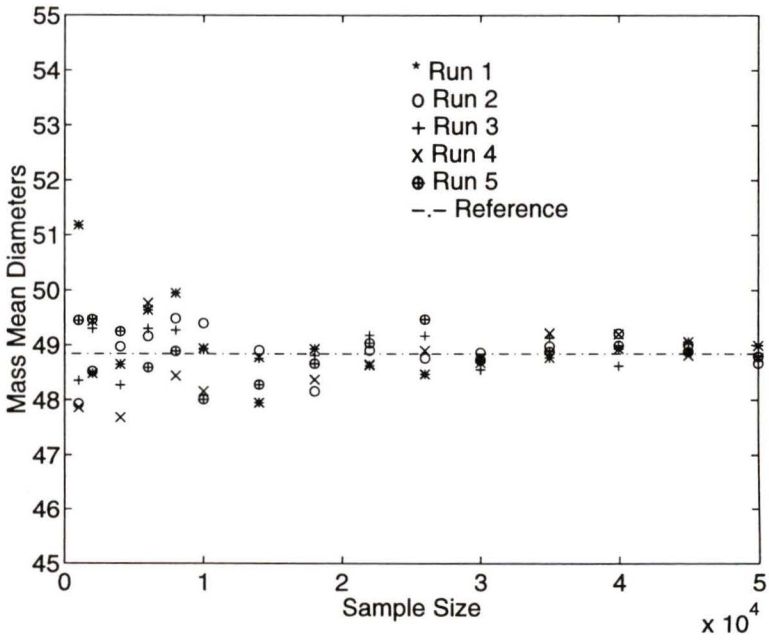

Figure 3.3: Sample size validation measurement.

3.3 Acoustic Excitation

Acoustic excitation is the main focus of this experiment. To investigate the effect of acoustic signals in a wide range of frequencies, a 6" × 9" coaxial horn with maximum power output of 80 Watts is used. The frequency response is between 25 Hz and 20 kHz. According to the studies of many researchers' linear instability analysis, the initial disturbance amplitude does not have to be large since the dominant wave growth rate of disturbances usually grows very fast [3]. But nonlinear analysis [4] suggests that both frequency and amplitude of initial disturbances are important in influencing the atomization processes, unless there is time allowing the initially small disturbances to grow large enough to have significant effect on the liquid disintegration. Experimental evidence [25] shows that the position and the power level of the acoustic excitation is very critical in laboratory experiments. Therefore during this experiment, care was taken for the positioning of the loud speaker and the speaker power output was carefully measured using a decibel meter.

3.4 Photographic Procedure

Prior to taking actual measurements, a series of studies on the visualization of the spray flow field was conducted. Since the conical liquid sheet from the pressure-swirl nozzle used is small, to visualize the wave form on the liquid sheet surface by photographs is quite difficult. At the beginning, different close-up combinations were attempted to make the image caught on the film as larger as possible. Also, to obtain clear pictures, different camera settings, such as aperture and shutter speed, and different ways of lighting were tried. However, it was still difficult to catch every moment of the spray characteristics using an ordinary camera taking discrete pictures of instantaneous flow field. This can be seen in some pictures shown in later chapters.

During photo-taking, an electrical connection between the stroboscope and the camera shutter is used, such that when the shutter is released, the stroboscope will emit one pulse of light to illuminate the spray. But the distance (related to light intensity) between the stroboscope and the spray is very critical for the final images. The use of a semi-opaque glass is necessary to make the stroboscopic light more uniform to enhance the picture quality.

3.5 PDPA Calibration

Even though the laser Doppler equipment has its own built-in calibration system, calibration of the PDPA is necessary to ensure that the alignment and the laser settings are all in proper condition. The calibration was performed using a single droplet generator (SDG) in the following three steps: i) theoretical analysis; ii) visualization; and iii) PDPA measurements.

3.5.1 Theoretical Analysis

In an early mathematical analysis, Rayleigh [7] employed the method of small disturbances to predict the conditions necessary to cause collapse of a liquid jet issuing at low velocity, for example, a low-speed water jet in air. This comprehensive analysis has been reviewed by McCarthy and Molloy [26].

Rayleigh compared the surface energy (directly proportional to the product of surface area and surface tension) of the disturbed configuration with that of the undisturbed liquid column. He then calculated the potential energy of the disturbed configuration (relative to the equilibrium value) as

$$E_s = \frac{\pi\sigma}{2d}(\kappa^2 + n^2 - 1)b_n^2 \tag{3.1}$$

where E_s is the potential surface energy; d the jet diameter (r the radius); b_n a constant in Fourier series expansion; κ dimensionless axial wave number ($2\pi r/\lambda = \pi d/\lambda$); λ wave length of the disturbance; and finally n any positive integer including zero (tangential wave number).

For non-symmetrical disturbances ($n \geq 1$), E_s is always positive, indicating that the liquid jet is always stable for this class of disturbances. When $n = 0$ and $\kappa < 1$, which is the symmetrical case, Eq. (3.1) shows that E_s is negative and the jet is unstable. That means a liquid jet which is affected by surface tension forces will become unstable only to axisymmetrical disturbances whose wave lengths satisfy the following condition

$$\lambda > \pi d \tag{3.2}$$

which corresponds to

$$\kappa < 1 \tag{3.3}$$

The conclusion of Rayleigh's theory is that for an inviscid liquid jet under laminar flow conditions with negligible ambient gas effect only some disturbances whose wave length is greater than its circumference will grow and there is one disturbance will grow fastest and eventually dominate the jet breakup.

From Rayleigh's theory and by assuming that b_n in Eq. (3.1) is proportional to $\exp(\omega t)$, where ω is the exponential growth rate of the disturbance, the exponential growth rate of the fastest-growing disturbance could be given as

$$\omega_{max} = 0.97\left(\frac{\sigma}{\rho_\ell d^3}\right)^{1/2} \tag{3.4}$$

and the λ_{max}, corresponding to ω_{max}, is

$$\lambda_{max} = 4.51d \tag{3.5}$$

After breakup, the cylindrical column of length $4.51d$ contracts into a spherical drop under surface tension, so that by conservation of mass, we have

$$4.51d \times \frac{\pi}{4}d^2 = \frac{\pi}{6}D^3 \tag{3.6}$$

where D is the diameter of the formed drop, and hence

$$D = 1.89d \tag{3.7}$$

Thus for the Rayleigh mechanism of breakup, the average drop size is nearly twice the diameter of the undisturbed jet. But for the actual case, the breakup mechanism is more complex and studies show that under certain conditions even for $n > 0$, disturbances may still be unstable and dominate the jet breakup [27]. The finally formed droplets are actually a combination of completely spherical, non-spherical and satellite droplets of different sizes.

3.5.2 Single Droplet Generator (SDG)

The single droplet generator (SDG) used in the calibration is a 001821-3 Orifice Mount Assembly made by Flow International Corporation. This SDG has an orifice of 76.2 μm in diameter (0.003 in.) (Figure 3.4). To mount this assembly on to our nozzle connecting rod, another piece of housing was made in order to hold the SDG. A very fine filtering mesh (A-CX-325 stainless steel mesh with width of opening of 43 μm (0.0017 in.)) was placed right before the SDG's inlet (See Figure 3.5).

3.5.3 Visualization

The visualization of the single droplet stream generated by the SDG is performed in three steps. Before conducting the visualization, the SDG was tested under regular

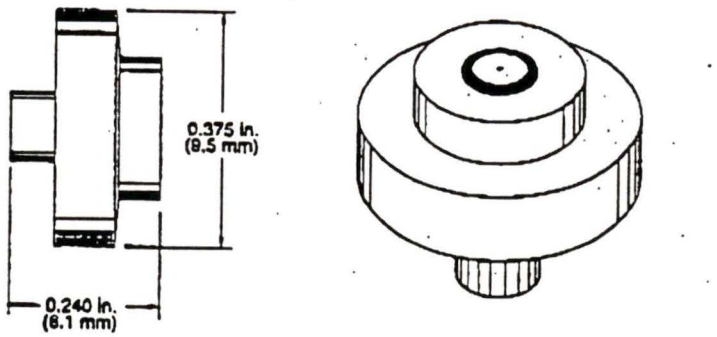

Figure 3.4: Geometry of the single droplet generator (SDG).

conditions (the injection pressure of 0.4 MPa (60 psi), using tap water as the liquid, and using the normal filter system). It was found that the SDG could not give a steady single droplet stream and it was clogged very easily because of its small opening. After careful cleaning by the ultrasonic cleaner (usually over 2 hours), de-ionized water was used and a stainless steel mesh (A-CX-325) as the final filter was placed right before the SDG inlet. The generated droplet stream was then observed to be very steady. Under the stroboscopic lighting, the main droplet stream (at this stage we could not tell the satellite droplets because the drop size is so small) and clouds of very fine drops were observed. Then an 10X20 microscope was used. The liquid stream was placed horizontally through the viewing region of the microscope. The satellite droplets between the main drops were observed under the microscope. Photographs were also taken under the microscope using backlighting. The main droplets and the satellites were caught on the photographs, some perfectly spherical and some not. Due to the high speed of the droplet stream and the limitation of viewing region, only a few drops were caught on every single photograph (on some pictures actually only one drop was caught). See Figures 3.6~3.9.

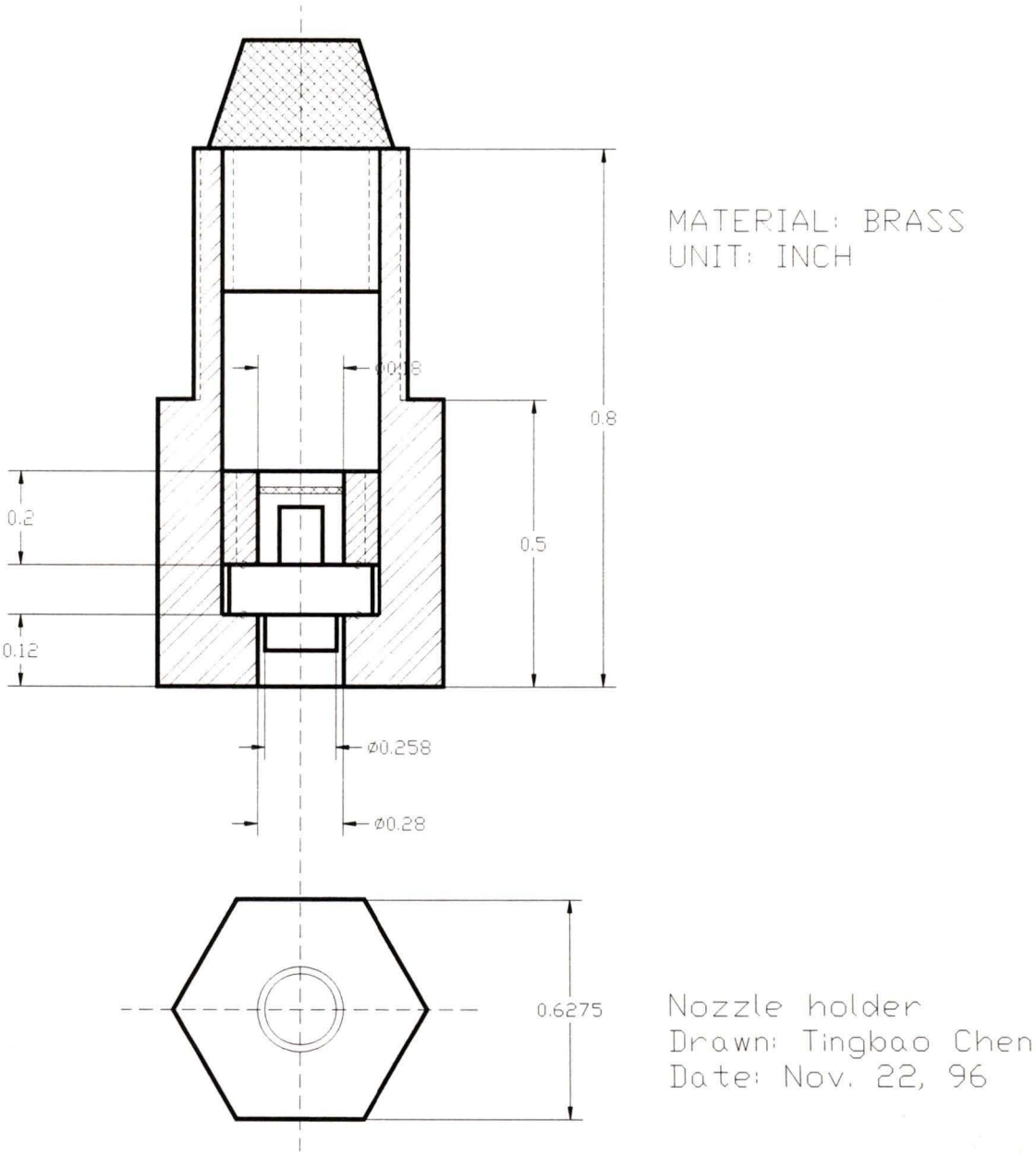

Figure 3.5: Holder of the single droplet generator (SDG).

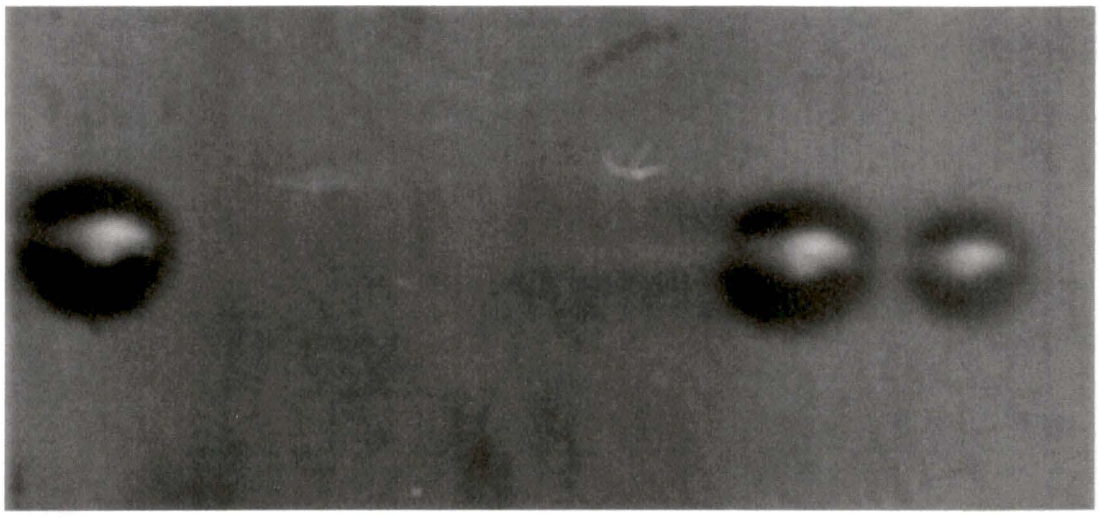

Figure 3.6: Photographs of droplets generated by the SDG. The primary droplets and the satellite droplets are captured in this picture. Injection pressure $\approx$ 0.07 MPa (10 psi). Axial distance from the nozzle exit $\approx$ 76.2 mm (3 inches). The droplet stream moves from left to right. The photograph is taken under the microscope of 10 $\times$ 20 times of magnification.

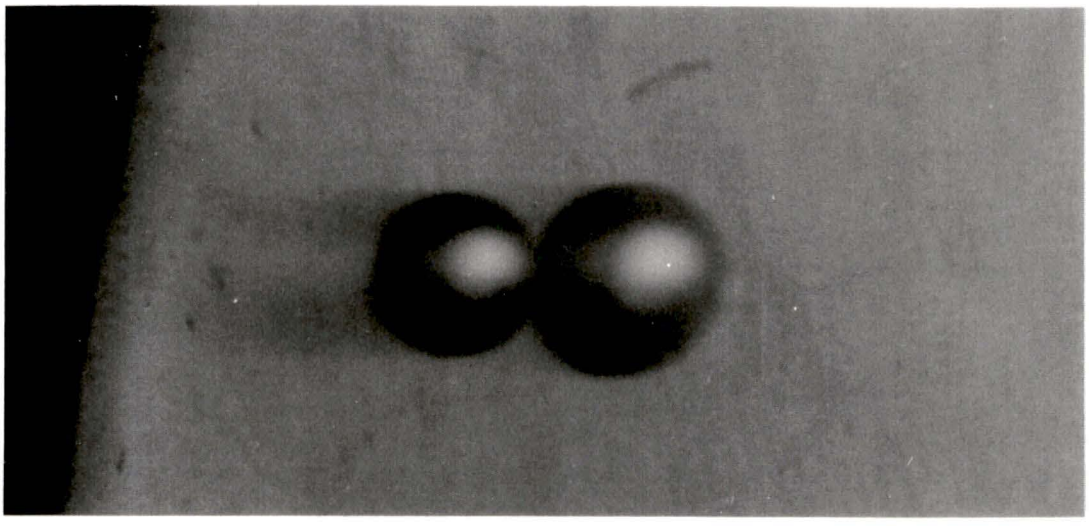

Figure 3.7: Photographs of droplets generated by the SDG. One primary droplet and one satellite droplet coalesces together. Injection pressure $\approx$ 0.07 MPa (10 psi). Axial distance from the nozzle exit $\approx$ 76.2 mm (3 inches). The droplet stream moves from left to right. The photograph is taken under the microscope of 10 $\times$ 20 times of magnification.

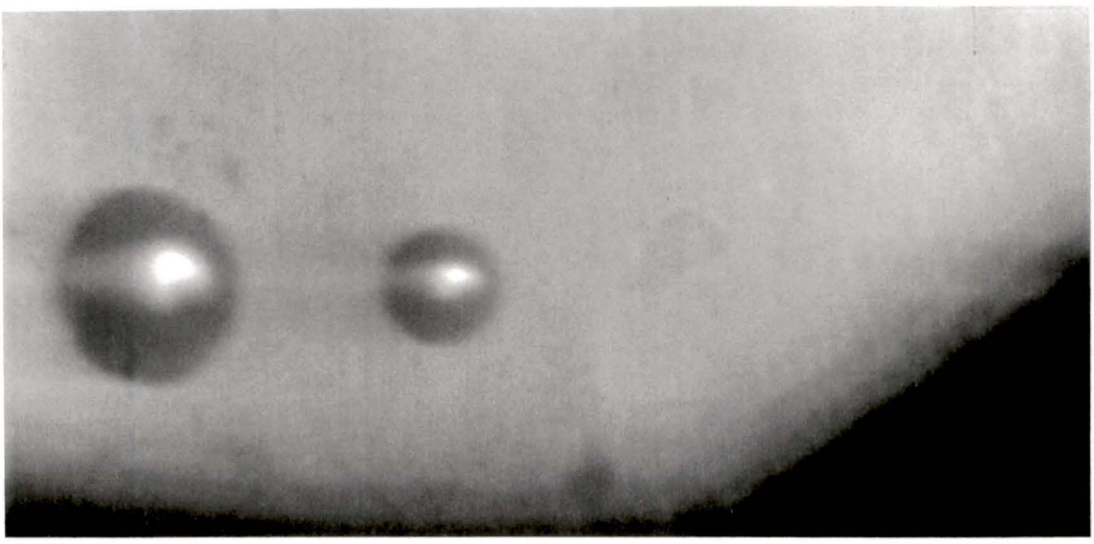

Figure 3.8: Photographs of droplets generated by th SDG. Injection pressure $\approx$ 0.07 MPa (10 psi). Axial distance from the nozzle exit $\approx$ 25.4 mm (1 inch). The droplet stream moves from left to right. The photograph is taken under the microscope of 10×20 times of magnification.

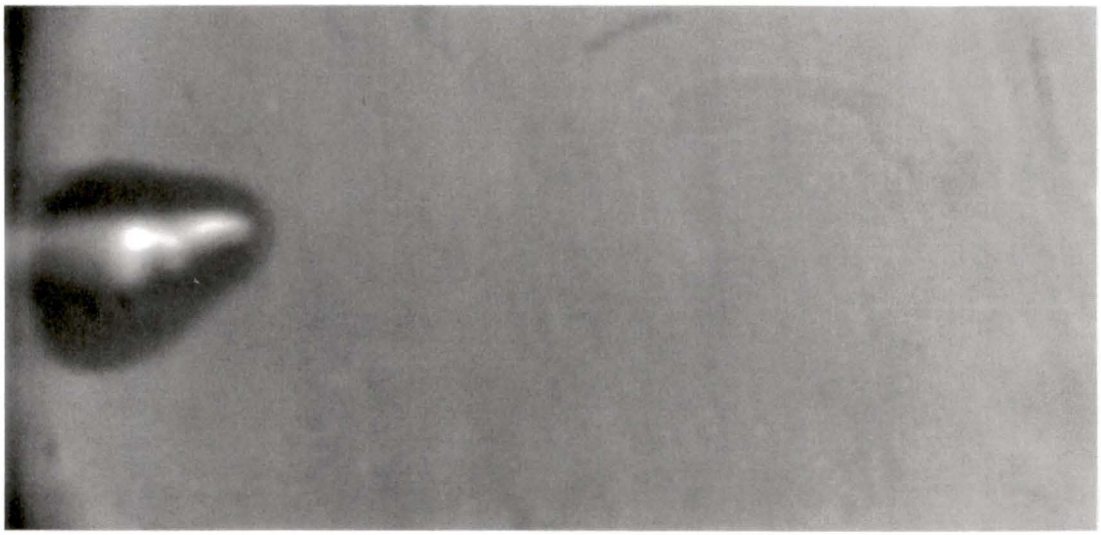

Figure 3.9: Photographs of droplets generated by the SDG. A non-spherical droplet is captured in this picture. Injection pressure $\approx$ 0.07 MPa (10 psi). Axial distance from the nozzle exit $\approx$ 50.8 mm (2 inches). The droplet stream moves from left to right. The photograph is taken under the microscope of 10×20 times of magnification.

3.5.4 PDPA Measurement

In order to calibrate the PDPA equipment using Rayleigh's theory, PDPA measurements of the SDG stream was conducted. At the beginning it was difficult to measure the droplet sizes by ordinary laser settings. Afterwards it was found that this was due to high injection pressure used (60 psi), as the velocity of the droplets so formed was too high and the presence of more droplets passing the measuring volume at one time and the collection of scattered light signals from the receiver caused interference. Also, the breakup mechanism was no longer in Rayleigh's breakup regime. By reducing the injection pressure (it was difficult to record the exact pressure value due to the resolution of the pressure gauges used: one is ENFM 7X100 kPa (100 psi) and another is ARO 160 psi), the PDPA measurements were conducted under different conditions, for example, a different injection pressure and different vertical locations from the nozzle exit. It was found that below 5 psi of injection pressure and at about 2 inches from the nozzle exit the measured results completely agreed with Rayleigh's prediction. The difference between the PDPA measurement and the prediction of Rayleigh's theory is less than 0.5% (See Table 3.2). At injection pressure of $5 \sim 10$ psi, the measurements confirmed the observations that the droplet size distributions have three peaks (Figure 3.10). The highest peak with narrow diameter range represents the main drops corresponding to Rayleigh's theory ($D \approx 1.89d$). The second peak, which falls into the middle size range corresponds to the satellite drops. The percentage of these drops is much lower. The third peak whose number density is even lower than the second peak represents the fine drop clouds. But under certain conditions, it is possible to get rid of those two peaks and make the jet breakup almost ideal as Rayleigh's prediction, an example is shown in Figure 3.11.

It should be pointed out that from the histogram of the measured droplet size distributions, the diameter range seems not as narrow as was expected, even though

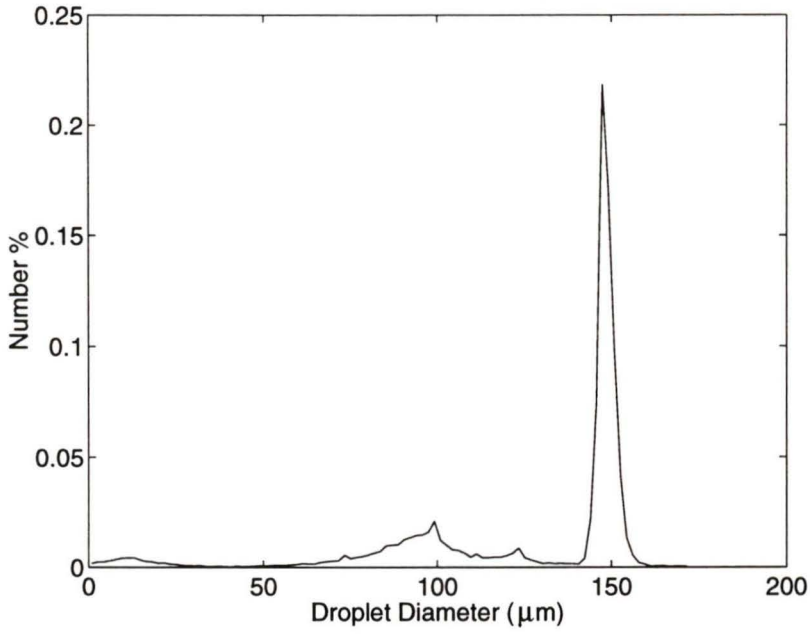

Figure 3.10: Diameter distributions of the droplets produced by the SDG.

the average diameter agrees perfectly with Rayleigh's theory. This may be caused by the oscillation of the droplet shapes. Photograph (Figure 3.9) shows that many of the droplets are not perfectly spherical and the PDPA settings gives a validation criterion that allows accepting some droplets which are non-spherical in a certain degree.

Table 3.2: The Measured Diameters of the SDG Compared with Rayleigh's Prediction

Measured Diameters of SDG					Rayleigh's Prediction
p (psi)	u (m/s)	D_{10} (μm)	D_{20} (μm)	D_{30} (μm)	$D = 1.89d$
≈ 1	6.7074	143.560	144.060	144.240	144.018 μm
≈ 2	7.1560	143.133	143.367	143.533	
≈ 5	8.2326	144.300	144.640	144.780	
≈ 8	9.2820	144.500	144.700	144.833	

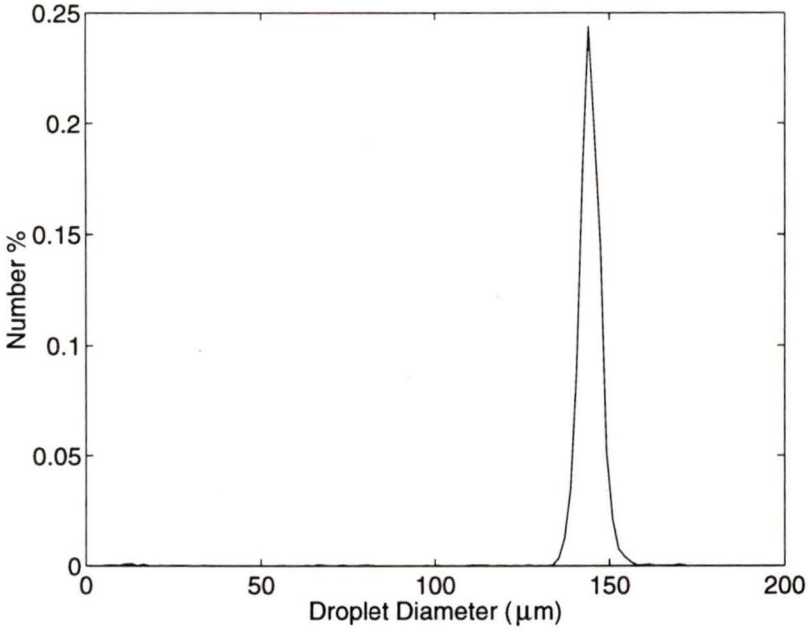

Figure 3.11: Diameter Distributions of the droplets produced by the SDG.

3.5.5 Acoustic Excitation on the SDG Stream

Besides the calibration performance using the SDG, the acoustic excitation effect on the SDG stream was also observed. Even though this phenomenon could not be caught by photographs, it could be observed on the SDG stream under stroboscopic backlighting and be caught on video. Under the acoustic excitation, clear wave forms of the stream could be seen similar to the forced vibration of a solid beam. The higher the frequency, the shorter the wave length. By adjusting the speed of the stroboscopic light, the wave forms of all frequencies could be seen.

Chapter 4

BASELINE PRESSURE-SWIRL NOZZLE

The baseline pressure-swirl nozzle is a commercial product made for applications with high injection pressure. In this chapter, the baseline pressure-swirl nozzle is tested under the injection pressure of about 0.4 MPa (60 psi) and the results of visualization and PDPA measurement are presented.

4.1 Introduction

Pressure-swirl nozzle is usually structured with a circular outlet opening preceded by a swirling chamber into which liquid flows through a number of tangential holes or slots (Figure 4.1). The pressurized liquid obtains axial and tangential velocities through the swirling chamber such that a thin conical liquid sheet is formed at the nozzle exit, and it eventually breaks up into droplets (Figure 4.2). Due to the effect of centrifugal forces, the spray angles may vary from a few degrees to almost 180°,

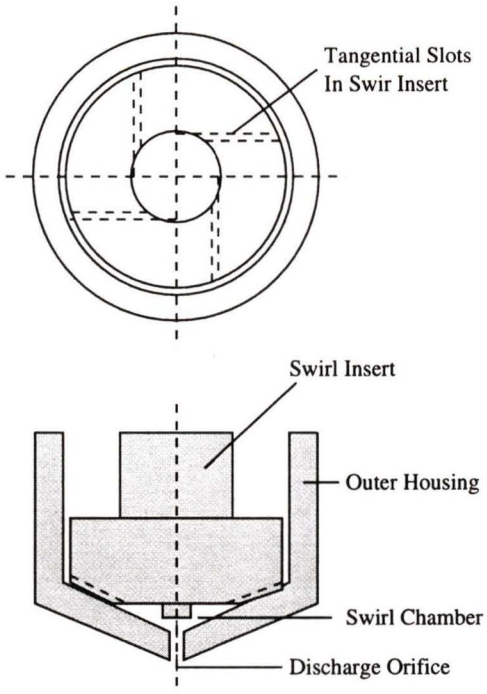

Figure 4.1: Schematic of the structure of the pressure-swirl nozzle.

depending on the nozzle designs and operating conditions. The droplet size in the spray is inversely proportional to the injection pressure and the spray angle, while the spray angle is dependent with the pressure differential and the ambient gas properties. The finest atomization of pressure-swirl nozzle occurs at high injection pressures and wide spray angles. But due to the pressure limitation for aerosol applications, the pressure-swirl nozzle can not meet the performance requirements of Johnson's aerosol space spray products at low injection pressures ($\leq$ 0.4 MPa (60 psi)) without chemical additives and other techniques applied.

In this chapter acoustic effect on the breakup mechanism of the baseline pressure-swirl atomizer is investigated. As will be seen later on, the acoustics does have effect on the breakup process of the conical liquid sheet created by the pressure-swirl nozzle, but significant reduction of droplet size has not yet been verified by the PDPA

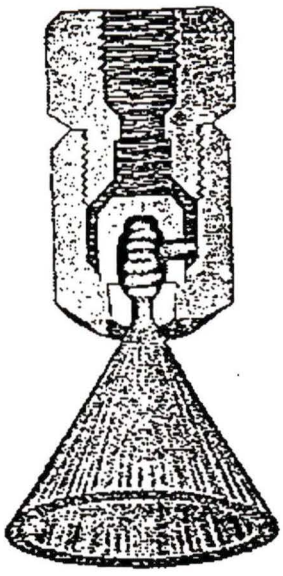

Figure 4.2: Schematic of the pressure-swirl nozzle assembly and the conical liquid sheet produced by the atomizer.

measurement in this experiment.

4.2 Test Conditions

Throughout the experiment for the baseline pressure-swirl nozzle, the test conditions are:

- Liquid: tap water
- Injection pressure: 0.4 MPa (60 psi) provided by compressed air
- Temperature: room temperature ($\approx 20^{o}C$)

Both flow visualization and PDPA measurement are used to investigate the spray characteristics with/without external acoustic excitations. The PDPA measurements

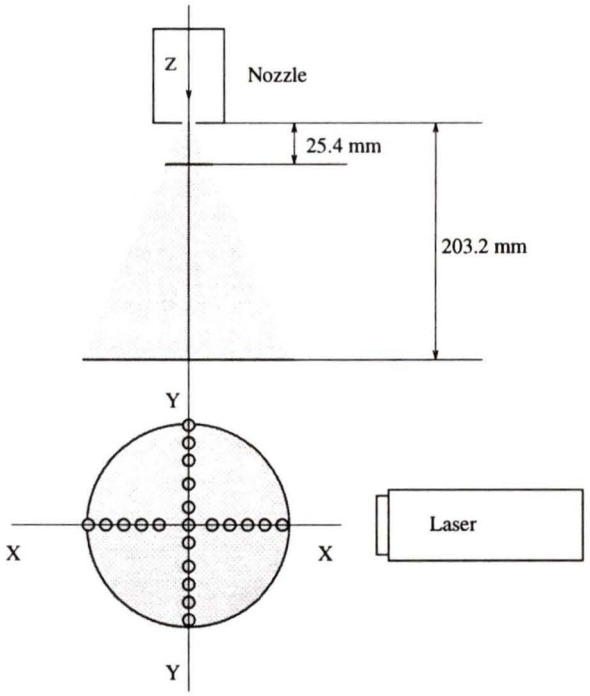

Figure 4.3: Schematic of PDPA measurement locations.

are carried out in two perpendicular radial directions at two axial locations of the spray field (25.4 mm (1 inch) and 203.2 mm (8 inches) from the nozzle exit), as schematically shown in Figure 4.3. For the case with acoustic excitations, the effect of acoustic frequency and power output amplitude is investigated on the spray angle and droplet size, as well as droplet size distributions and other characteristic parameters.

The apparatus setup for acoustic excitations was discussed earlier in Chapter 2, section 2.2. A 6" $\times$ 9" coaxial horn, driven by the amplified sinusoidal signal from the signal generator, was used to provide external perturbation on the conical liquid sheet surface. The frequency is set from the function generator. The power output level is set through the dial of the amplifier, which is calibrated by a decibel meter to determine the sound pressure. The power level calibration is made by setting the dial to a certain location, such as power level 1, 2, and so on, and measuring the sound

decibels at a distance of 127 mm (5 inches) from the speaker with different signal frequencies. The sound decibels are then converted to sound pressure by

$$p = p_0 10^{(L_p/20)} \tag{4.1}$$

where L_p is the measured decibels, p the relevant sound pressure (Pa), and $p_0 = 20 \times 10^{-6}$ Pa is a reference pressure equivalent to the sound decibels produced by a calibration sound generator. The power level calibration results are listed in Table 4.1.

4.2.1 Diameter Analysis

The mass mean diameter (D_{30}) is a key parameter in measuring the quality of atomization. It is defined by

$$D_{30} = \left(\frac{\int_0^\infty D^3 f(D) dD}{\int_0^\infty f(D) dD} \right)^{\frac{1}{3}} \tag{4.2}$$

where $f(D)$ represents the number-based probability density function for the droplet size distribution over the droplet diameter space. The third power over the diameter D makes the mass mean diameter very sensitive to the presence of large droplets.

The Sauter mean diameter (D_{32}) is equal to the ratio of liquid volume to surface area for all the droplets in a spray, and is a representative mean diameter of droplets. It is defined as

$$D_{32} = \frac{\int_0^\infty D^3 f(D) dD}{\int_0^\infty D^2 f(D) dD} = \frac{D_{30}^3}{D_{20}^2} \tag{4.3}$$

The PDPA can provide point measurement of D_{30} and D_{32}. In order to compare with Johnson's Malvern line-of-sight measurements and provide more representative mean droplet diameters in the spray, The point measurements of D_{30} and D_{32} are converted

Table 4.1: The sound pressures relevant to different power levels and different frequencies.

Power level in dB

Freq. (kHz)	P. Level 1.0	P. Level 1.5	P. Level 2.0	P. Level 3.0	P. Level 4.0	P. Level 5.0
1.0	94.75	104.8	118.4	127.5	128	129.2
2.0	95.4	106.7	118.5	128	129.7	132.5
3.0	93.5	105	116.7	127.7	131.6	132.3
4.0	88	97.5	110.8	119.2	121.9	122
5.0	80.5	82.8	102.1	107.7	100.5	105
6.0	76	88.2	101.7	112.4	113.4	109.2
7.0	74	84	95	103.2	104.6	104.4
8.0	56.2	67.2	72.8	89.7	92.5	101.2
9.0	63.1	78.5	86.2	93.6	86.2	94.6
10.0	61.5	72.6	83	92	93.6	93
11.0	52.4	65.1	79.2	88.1	85.5	88.1
12.0	41.2	52.7	64.7	71.2	75.3	76.3
13.0	46.4	59.4	69.7	79.6	83.6	84.2
14.0	41.5	52.6	65.4	71.4	72.2	74.3
15.0	42	51.5	59.5	65.5	70.2	72.5

Power level in Pa

Freq. (kHz)	P. Level 1.0	P. Level 1.5	P. Level 2.0	P. Level 3.0	P. Level 4.0	P. Level 5.0
1.0	1.093	3.476	16.635	47.427	50.238	57.681
2.0	1.178	4.325	16.828	50.238	61.098	84.339
3.0	0.946	3.557	13.678	48.532	76.038	82.420
4.0	0.502	1.500	6.935	18.240	24.890	25.179
5.0	0.212	0.276	2.547	4.853	2.119	3.557
6.0	0.126	0.514	2.432	8.337	9.355	5.768
7.0	0.100	0.317	1.125	2.891	3.396	3.319
8.0	0.013	0.046	0.087	0.611	0.843	2.296
9.0	0.029	0.168	0.408	0.957	0.408	1.074
10.0	0.024	0.085	0.283	0.796	0.957	0.893
11.0	0.008	0.036	0.182	0.508	0.377	0.508
12.0	0.002	0.009	0.034	0.073	0.116	0.131
13.0	0.004	0.019	0.061	0.191	0.303	0.324
14.0	0.002	0.009	0.037	0.074	0.081	0.104
15.0	0.003	0.008	0.019	0.038	0.065	0.084

to the line-averaged diameters as follows [28] [29]

$$\overline{D_{30}} = \left(\frac{\sum_{i=1}^{N} w_i D_{30_i}^3}{\sum_{i=1}^{N} w_i} \right)^{\frac{1}{3}} \tag{4.4}$$

and

$$\overline{D_{32}} = \frac{\sum_{i=1}^{N} w_i D_{30_i}^3}{\sum_{i=1}^{N} w_i D_{20_i}^2} \tag{4.5}$$

where the weighting factor is defined as

$$w_i = \frac{N_i dr_i}{t_i A_{p_i}} \tag{4.6}$$

Other parameters are defined below:

$\overline{D_{30}}$ = Line-averaged D_{30}

$\overline{D_{32}}$ = Line-averaged D_{32}

N = Total number of data points along radial direction

D_{30_i} = Measured D_{30} at point i

D_{20_i} = Measured D_{20} at point i

N_i = Validated droplet number counts at point i

dr_i = Distance between point i and $i+1$ along radial direction x or y

t_i = Elapsed measurement time at point i

A_{p_i} = Probe area at point i

4.3 Results and Discussion

4.3.1 Photographic Observations

Photographic observations are made using backlighting technique with a stroboscope as the pulsed light source, as described earlier. Figures 4.4~4.9 show the typical back-lit stroboscopic photographs of the sprays with and without external acoustic excitations at a fixed acoustic power output level from the amplifier. The conical spray without external acoustic excitations, as shown in Figure 4.4, exhibits a liquid sheet with the development of unstable waves due to the Kelvin-Helmholtz instability [2][3][4], and eventual disintegration into individual droplets. The unstable waves of the liquid sheet surface are less pronounced and clearly not symmetrical, and their shape seems more irregular and random-like. Figure 4.4 exhibits not only non-symmetrical liquid sheet and the unstable waves on its surface, but also non-symmetrical liquid sheet breakup region as well. It is seen that left-hand side of the liquid sheet disintegrates into droplets closer to the atomizer exit than the right-hand side. The chaotic irregular disruption of the liquid sheet segments and droplet formation processes appears to cause droplets to group into clusters. Bachalo, et al. [30] investigated the characteristics of pressure-swirl atomization and resulting sprays by using a fast Fourier transform analysis of the time-of-arrival data in the phase Doppler measurement, and found that the droplet arrival at the measurement location was essentially random and the dominant frequency of the droplet clusters was about 55 Hz if the spray was in a swirling airflow field. This is particularly true when the measurement location is far away from the liquid sheet breakup region due to the droplet motion, aerodynamic drag effect and air entrainment by the spray droplets. The ambient air motion tends to dominate the characteristics of droplet motion because of the small inertia each individual droplet possesses. Because liquid sheet breakup

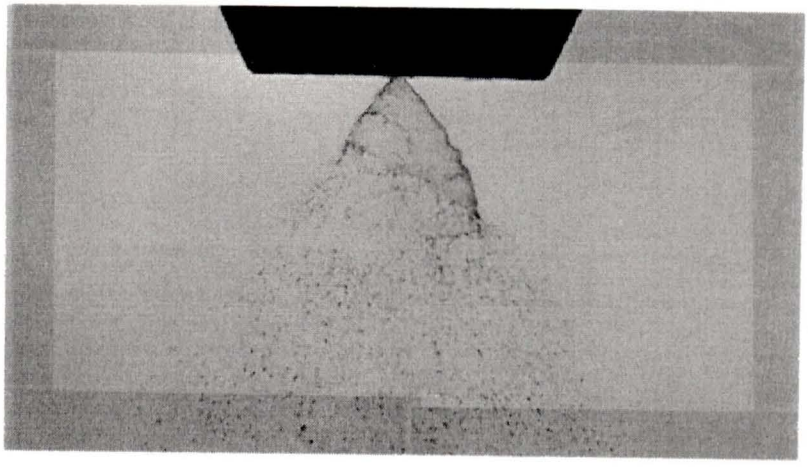

Figure 4.4: Photograph of the spray produced by the baseline pressure-swirl nozzle without acoustic excitations. $p = 0.4$ MPa (60 psi).

processes appear random and stochastic (at least at the measurement location some distance downstream of the breakup region), the time-of-arrival data analysis from the PDPA measurement may not be able to resolve the droplet clustering due to the instability of the liquid sheet.

With the presence of the external disturbances, the liquid sheet disintegration processes are modified as shown in Figure 4.5~4.9. At the frequency of 0.5 kHz, Figure 4.5 shows that both the conical liquid sheet and surface waves become more conspicuous, symmetrical and regular, and the sheet breakup along the circumferential direction occurs almost at the same distance from the atomizer exit. As a result, liquid sheet atomization and droplet formation occur in a more symmetrical, regular and controlled manner. As the frequency of the external excitations is increased (Figures 4.6~4.9), more visible wave structures appear on the liquid sheet with larger wave amplitudes before its disruption into droplets. It must be mentioned that because the liquid sheet breaks up at approximately one half wavelength interval, any measurement of the breakup length will be at most accurate up to plus/minus one half wavelength. It should also be pointed out that the frequencies of the external excitations used are orders of magnitude larger than that of the droplet clustering in

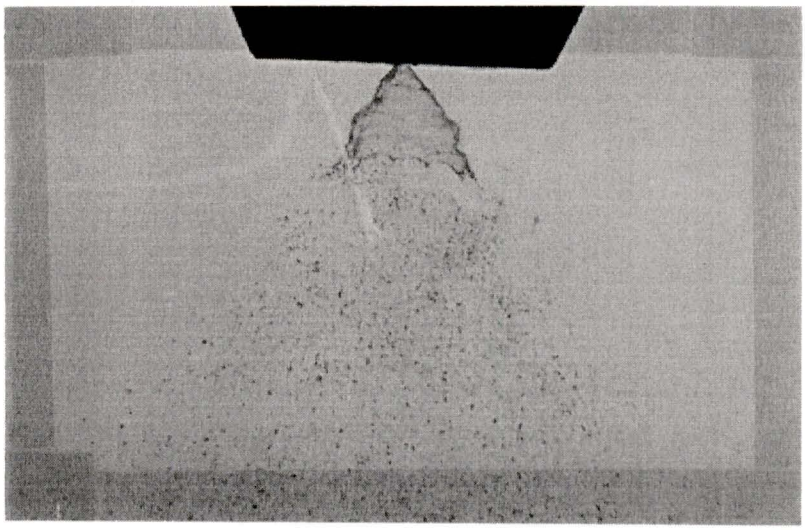

Figure 4.5: Photograph of the spray produced by the baseline pressure-swirl nozzle with acoustic excitations. $p = 0.4$ MPa (60 psi), $f_a = 0.5$ kHz, and power level 3.

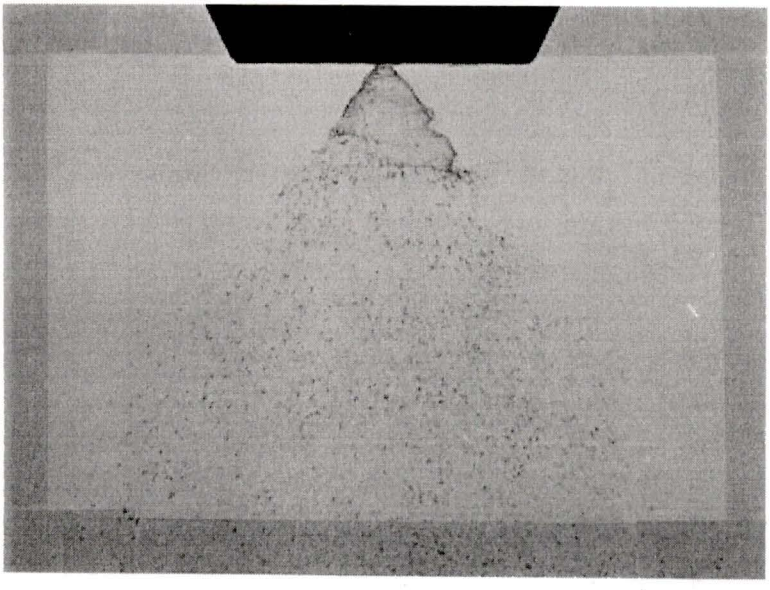

Figure 4.6: Photograph of the spray produced by the baseline pressure-swirl nozzle with acoustic excitations. $p = 0.4$ MPa (60 psi), $f_a = 0.75$ kHz, and power level 3.

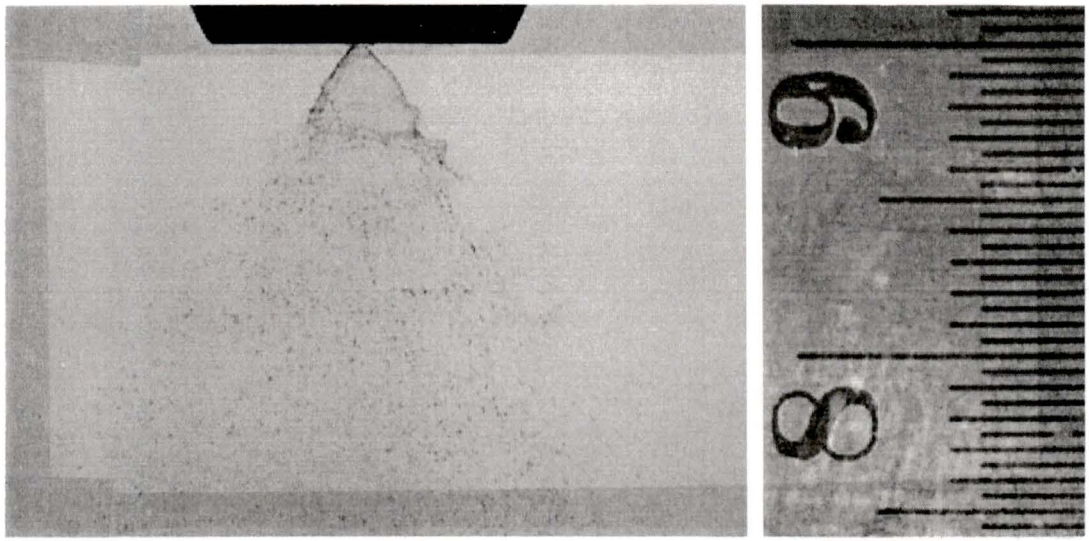

Figure 4.7: Photograph of the spray produced by the baseline pressure-swirl nozzle with acoustic excitations. $p = 0.4$ MPa (60 psi), $f_a = 1.75$ kHz, and power level 3.

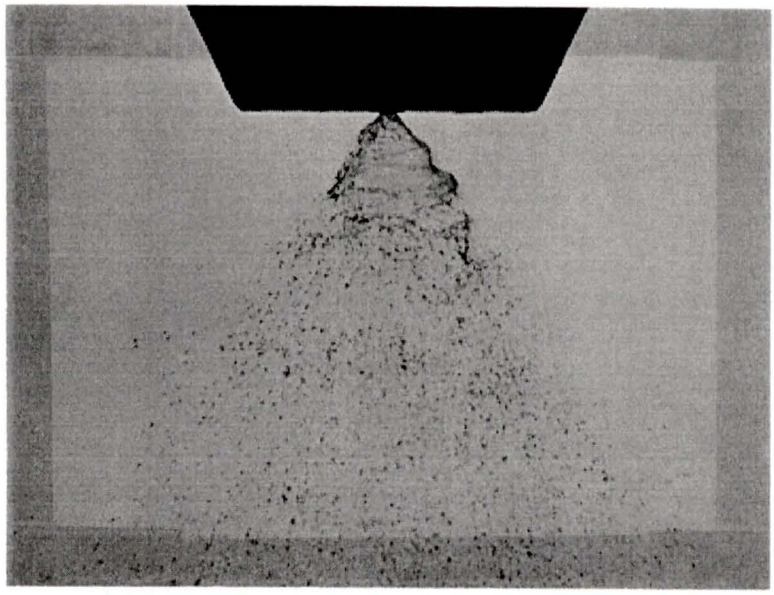

Figure 4.8: Photograph of the spray produced by the baseline pressure-swirl nozzle with acoustic excitations. $p = 0.4$ MPa (60 psi), $f_a = 5.5$ kHz, and power level 3.

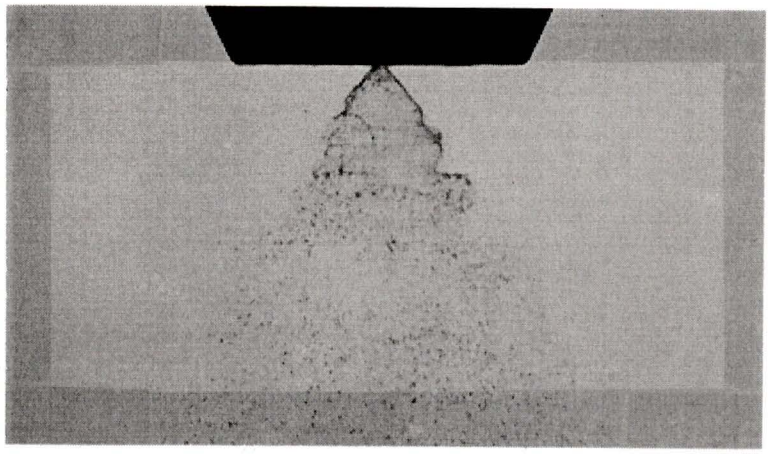

Figure 4.9: Photograph of the spray produced by the baseline pressure-swirl nozzle with acoustic excitations. $p = 0.4$ MPa (60 psi), $f_a = 16.5$ kHz, and power level 3.

the swirling airflow reported by Bachalo, et al. [30]. It might be pointed out that a scale showing one centimeter length is given in Figure 4.7. Clearly, the liquid sheet breakup occurs at a distance of less than 5 mm from the atomizer exit and at the axial location of 10 mm from the nozzle exit, the spray profile is well developed.

Although ambiguities exist in determining the exact locations of the liquid sheet and outer periphery of the spray, quantitative information can be retrieved from the back-lit stroboscopic photographs. Figure 4.10 presents the spray angle as a function of the acoustic disturbance frequency for a fixed disturbance power level. It is seen that the effect of external disturbances on spray angle is minimal, within approximately 10% compared with the case without external disturbances. Similar observations have also been reported by Takahashi, et al. [12] for pressure-swirl atomization, even though their disturbance power levels are much higher.

4.3.2 PDPA Measurement

Figure 4.11 shows the radial distributions of mass mean diameter (D_{30}) and Sauter mean diameter (D_{32}) for the baseline pressure-swirl atomizer at the injection pressure

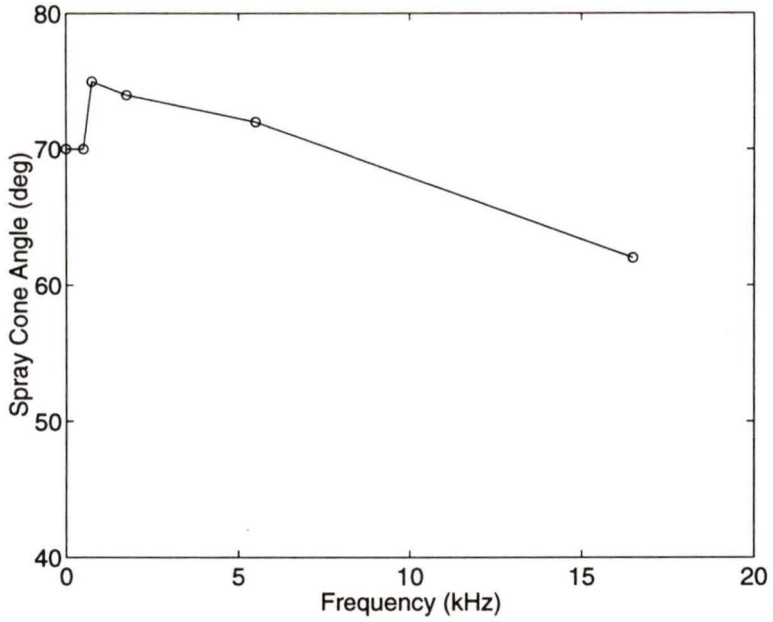

Figure 4.10: Effect of external acoustic excitations on the spray cone angle. $p = 0.4$ MPa, and power level 3.

of 0.4 MPa (60 psi) and at the axial location of $z = 25.4$ mm (1 inch) from the nozzle exit, with acoustic excitations of 7.0 kHz frequency and power level two which is relevant to a sound pressure of about 1.125 Pa (95 dB) at 127 mm (5 inches) distance from the loud speaker. Clearly, the diameter distribution is not symmetric along the radial direction from the centerline. This was observed from the flow field visualization under the stroboscopic backlighting, as discussed in previous section 4.3.1. It is also seen that the droplet diameter decreases gradually towards the spray centerline, thus smaller droplets are present in the spray core region, and larger droplets exist near the spray periphery. This result is consistent with the photographic observations shown earlier. The small droplets quickly lose their momentum, and follow the motion of the ambient air which is entrained by the spray droplet cloud and move towards the spray centerline. Whereas the large droplets with relatively high inertia continue their straight trajectories along their original direction, which is the same as the cone angle

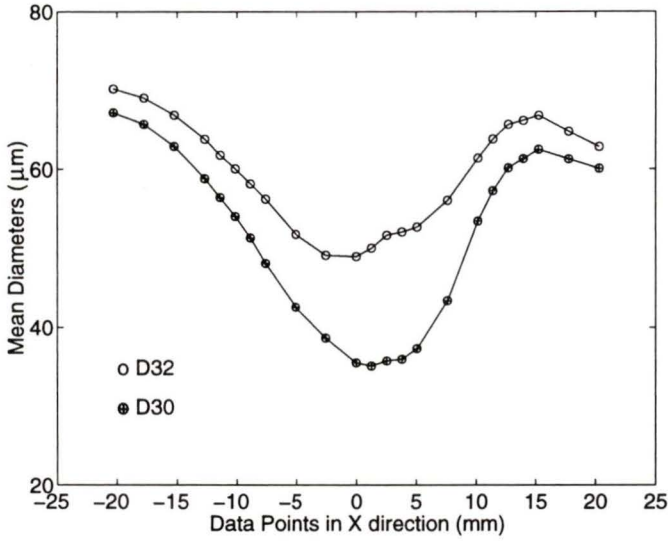

Figure 4.11: Mean diameters of baseline measurement at 25.4 mm (1 inch) of axial location with acoustic excitations. $p = 0.4$ MPa (60 psi), $f_a = 7.0$ kHz, and power level 2 (or 1.125 of sound pressure at 127 mm (5 inches) distance from the loud speaker).

of the liquid sheet. As a result, small droplets accumulate near the spray centerline and large droplets remain in the spray edge region. Nevertheless, further towards the spray edge, the droplet size decreases again because it represents the size of the droplet clouds torn off from the tip of the wavy conical liquid sheet by the air dynamic interaction. These droplet clouds have relatively low velocity mainly due to the air drag effect, and this fact can be seen from Figure 4.12. But one difficulty of the measurement of these satellite droplet clouds is that at the further edge region, the PDPA data rate is quite low because of low droplet concentration. Figures 4.12 and 4.13 show the measured mean velocity and volume flux distributions, respectively, under the same conditions.

Shown in Figure 4.14 are the measured results at a distance of 203.2 mm (8 inches) from the atomizer exit, without acoustic excitations. The two curves represent the two radial profiles of the mass mean diameter along two perpendicular radial

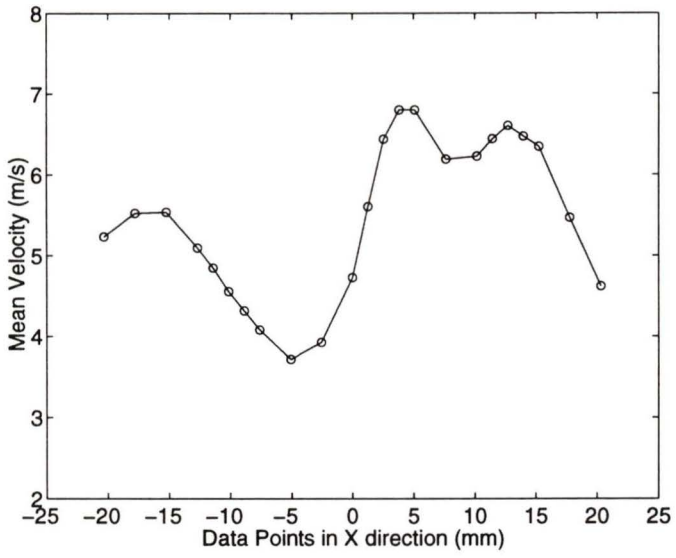

Figure 4.12: Mean velocity of baseline measurement at 25.4 mm (1 inch) of axial location with acoustic excitations. $p = 0.4$ MPa (60 psi), $f_a = 7.0$ kHz, and power level 2 (or 1.125 of sound pressure at 127 mm (5 inches) distance from the loud speaker).

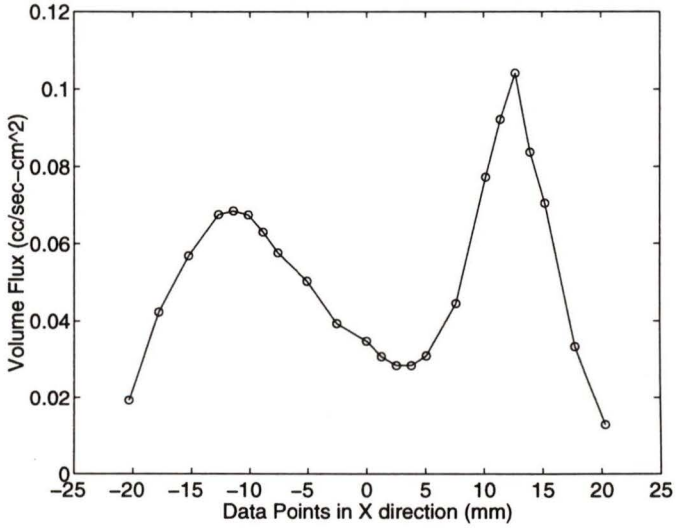

Figure 4.13: Volume flux of baseline measurement at 25.4 mm (1 inch) of axial location with acoustic excitations. $p = 0.4$ MPa (60 psi), $f_a = 7.0$ kHz, and power level 2 (or 1.125 of sound pressure at 127 mm (5 inches) distance from the loud speaker).

directions (x and y). Clearly the droplet size distribution is not symmetric at this location, and the smaller droplets have all accumulated towards the centerline and the larger droplets remain in the edge region. It can be seen that this distribution is totally different from the case at 25.4 mm (1 inch) from the nozzle exit. The profiles show that the diameter is small at the centerline and then gradually increases along the radial direction towards the spray edge region. A comparison between Figure 4.11 and 4.14 reveals that along the axial direction of the spray, the mass mean diameter increases at corresponding radial locations. This result is typical of droplet size distributions for hollow cone sprays produced by pressure-swirl atomizer [1]. It is not because of droplet collisions and resulting coalescence as droplet number concentration is fairly low and spray in the measurement locations may be still be considered dilute. It is also not because of evaporation of small droplets as in the practical combustion chambers where small droplets may evaporate faster than the larger ones under the same high temperature conditions. The droplet evaporation for the present experimental conditions may be regarded negligible due to the low ambient air temperature and high humidity (near saturation). The apparent increase in the mass mean diameter is due to the entrainment effect of droplets and the ambient air. More and larger droplets gradually follow the motion of air towards the inner region of the spray, unless the droplets are large enough so that they will keep quite amount of momentum to follow their original direction. The larger droplets have more dominant influence on the mass mean diameter as shown in Eq. (4.2). The third power over the diameters makes the mass mean diameter very sensitive towards the presence of large droplets (This can be seen from Figures 4.15 and 4.16).

Figures 4.15 and 4.16 show the typical measured diameter distributions at the centerline and the edge of the spray, under the condition of 0.4 MPa (60 psi) injection pressure and at 25.4 mm (1 inch) distance from the atomizer exit, with acoustic

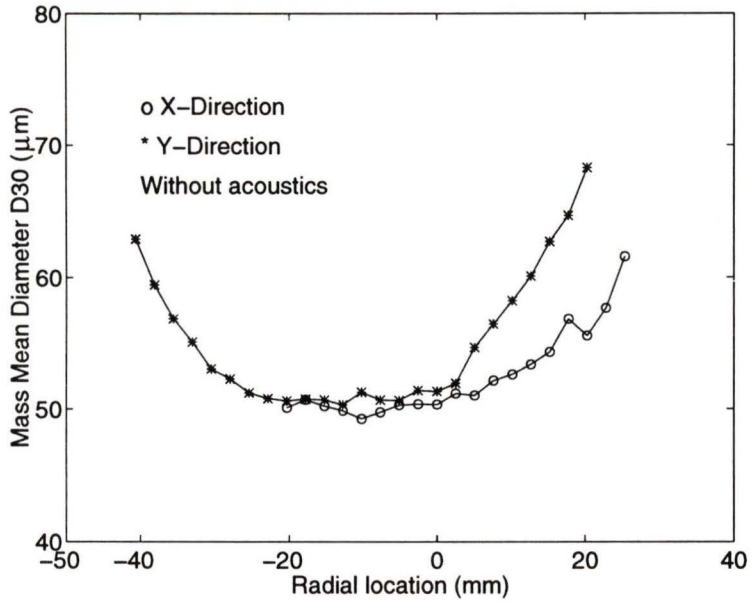

Figure 4.14: Mass mean diameter distribution along radial directions x and y, at axial location of 203.2 mm (8 inches) from the nozzle exit without acoustic excitations. $p = 0.4$ MPa (60 psi).

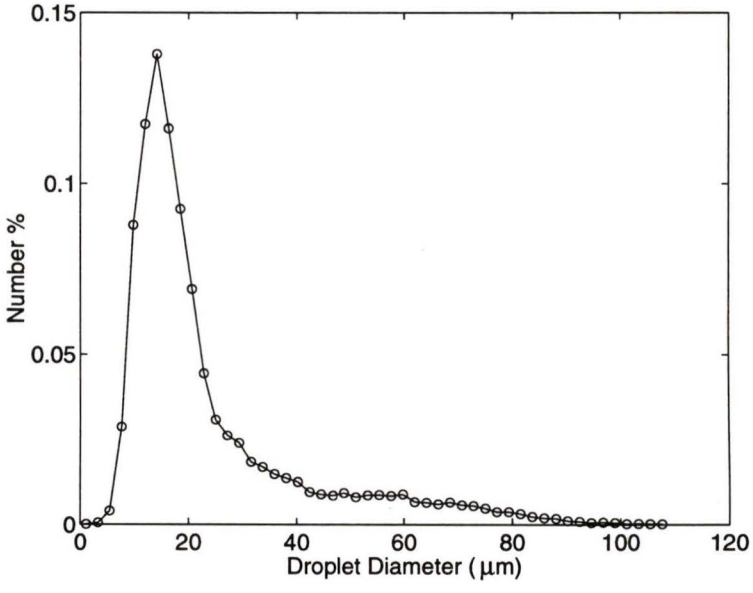

Figure 4.15: Typical diameter distributions of the baseline pressure-swirl nozzle at the centerline with acoustics. $p = 0.4$ MPa (60 psi), $x = 0$, $y = 0$, $z = 25.4$ mm (1 inch), $f_a = 7.0$ kHz, power level 2, $D_{30} = 35.79$ μm.

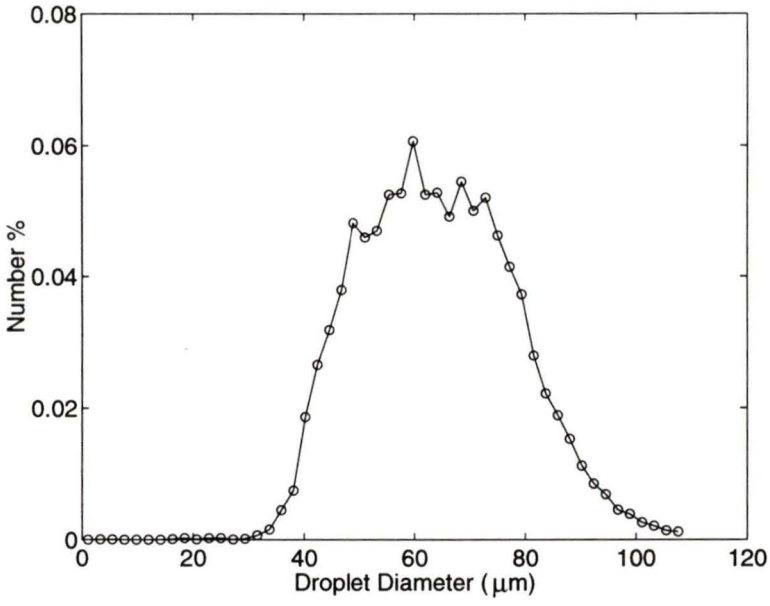

Figure 4.16: Typical diameter distributions of the baseline pressure-swirl nozzle at the edge with acoustics. $p = 0.4$ MPa (60 psi), $x = 22.86$ mm (0.9 inches), $y = 0$, $z = 25.4$ mm (1 inch), $f_a = 7.0$ kHz, power level 2, $D_{30} = 67.092$ μm.

excitations of 7.0 kHz frequency and power level 2. From the figures it can be seen that the distribution of the diameter range is quite wide, which results in the mass mean diameter quite large because the mass mean diameter D_{30} is dominated by the third power over the diameters. In Figure 4.15, even though most of the droplets are about or below 20 μm in diameter, the mass mean diameter is still 35.790 μm. At the spray edge (at radial location of $x = 22.86$ mm), it is even worse that the mass mean diameter is 67 μm, although most droplets appear to be in the right range of the distribution histogram.

After the first few measurements, the baseline pressure-swirl nozzle was disassembled and the symmetric measurement results can now be explained. The slots of the insert for the swirl chamber are totally randomly made (Figure 4.17). That includes the slot angle, width and locations. This is probably because the manufacturer is

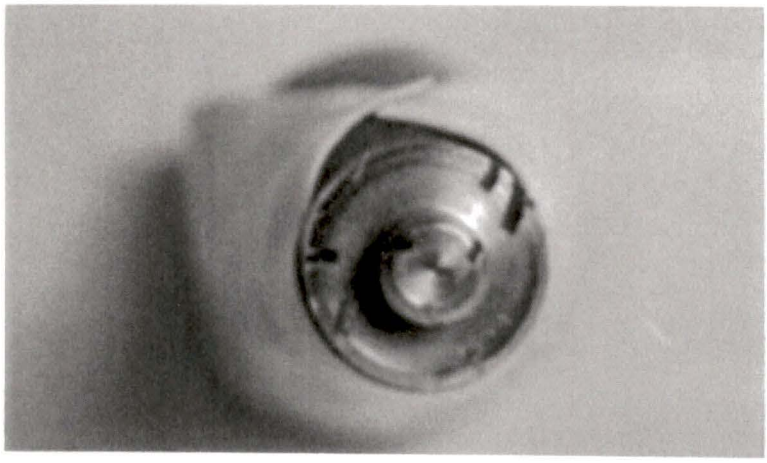

Figure 4.17: Photograph of the insert of the baseline pressure-swirl nozzle.

mostly interested in, besides the droplet size, the total flow rate. Considering the application of this type of atomizer, the injection pressure is usually high, hence the atomization is usually not a problem.

Figure 4.18 shows the variation of the measured mass mean diameter with frequency at power level 3, which is equivalent to a sound pressure of about 47.427 Pa (127.5 dB) at the frequency of 1 kHz. These data are measured at the spray centerline, 25.4 mm (1 inch) from the nozzle exit. It is clearly seen that there is one frequency (about 1.25 kHz) at which the diameter decreases by about 3 μm. This frequency is different from the results of Takahashi and Schmoll [12] who used a piezoelectric driver to enhance the liquid atomization of a pressure-swirl nozzle. Their results show a frequency of about 19 kHz at which the droplet size is clearly decreased. However, their results also show that at some locations the droplet size is decreased while at some other locations the droplet size is actually increased. Hence the net effect on the droplet diameter (such as line-averaged mean diameter) may not be decreased significantly.

Figures 4.19~4.22 present the variations of the line-averaged diameter (D_{30} & D_{32}) with the acoustic frequency at different power levels and different axial locations from

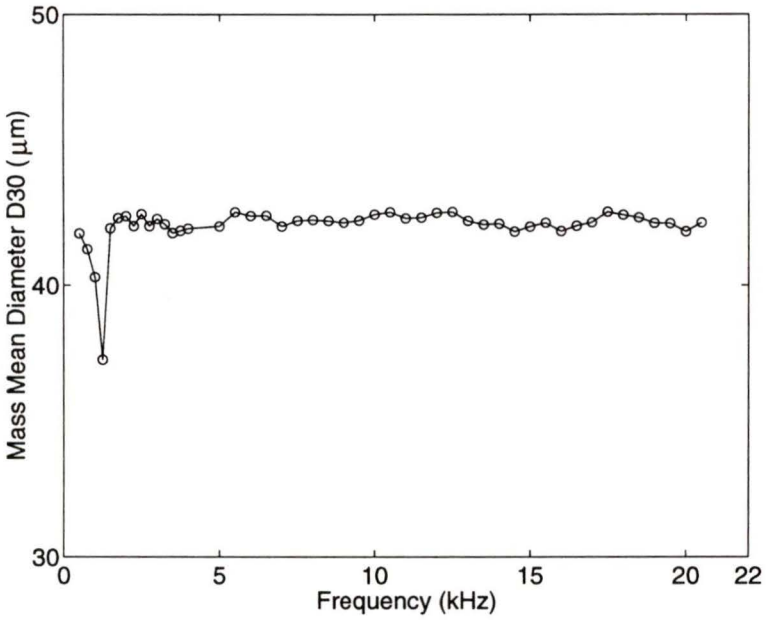

Figure 4.18: Mass mean diameter variation with frequency at power level 3. $p = 0.4$ MPa (60 psi), $x = 0$, $y = 0$, $z = 25.4$ mm (1 inch).

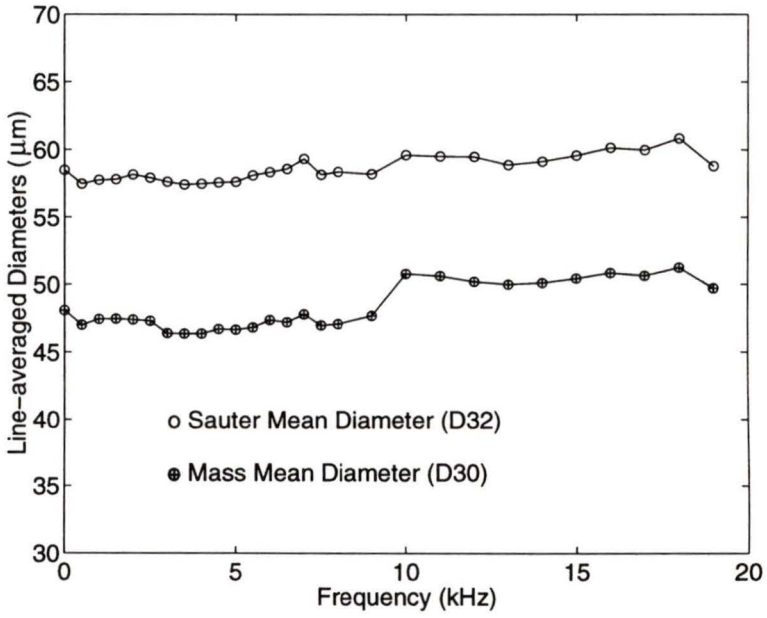

Figure 4.19: Line-averaged diameters with frequency at power level 2. $p = 0.4$ MPa (60 psi), $x = 0$, $y = 0$, $z = 25.4$ mm (1 inch).

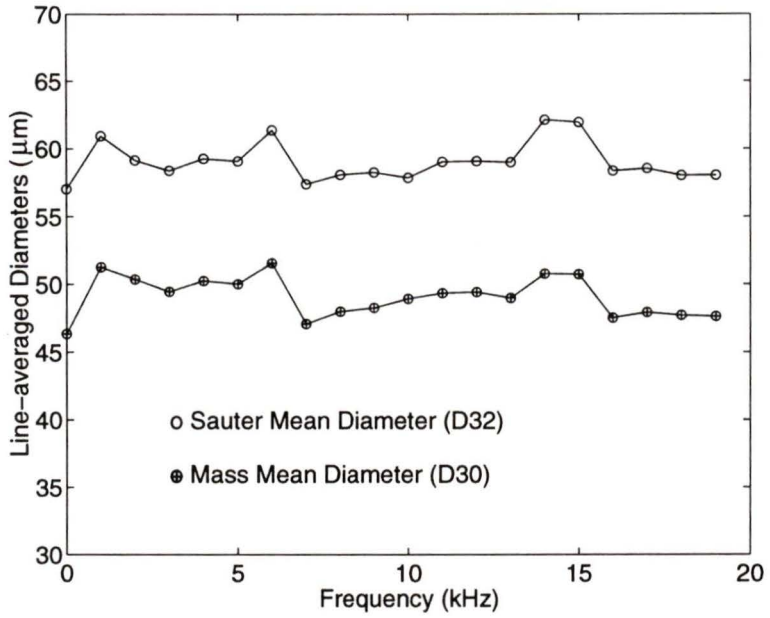

Figure 4.20: Line-averaged diameters with frequency at power level 5. $p = 0.4$ MPa (60 psi), $x = 0$, $y = 0$, $z = 25.4$ mm (1 inch).

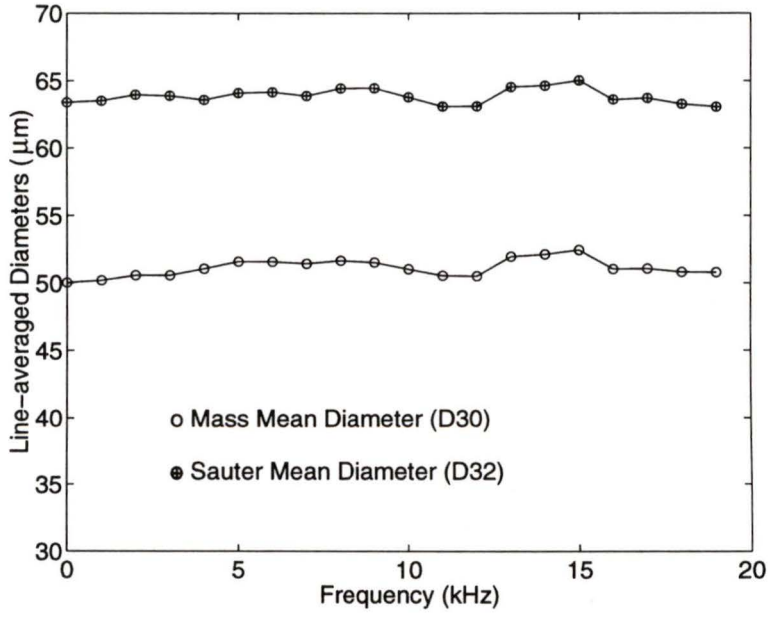

Figure 4.21: Line-averaged diameters with frequency at power level 1.5. $p = 0.4$ MPa (60 psi), $x = 0$, $y = 0$, $z = 203.2$ mm (8 inches).

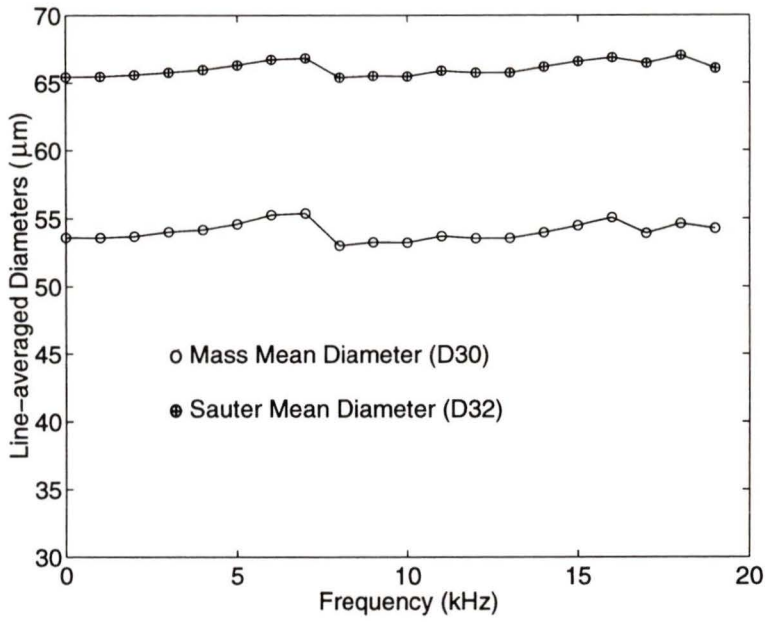

Figure 4.22: Line-averaged diameters with frequency at power level 3. $p = 0.4$ MPa (60 psi), $x = 0$, $y = 0$, $z = 203.2$ mm (8 inches).

the nozzle exit. These figures show similar results and the droplet size does not seem to change much with the frequency. But the diameter does decrease with power output levels (also see Figures 4.23 and 4.24) except the results at 203.2 mm (8 inches) from the nozzle exit. This is probably caused by the fact that the spray is not symmetric, hence the measurement location is not the same as at 25.4 mm (1 inch) from the nozzle exit. On the other hand, the spray itself is unsteady all the time and the power output levels chosen are very close for this case. As shown in Figures 4.19 through 4.22, the power level has more effect on the spray closer to the nozzle exit than that further downstream. That confirms that the degree of external perturbation on the conical liquid sheet surface is not only controlled by the frequency, but also controlled by the power level. Once the conical liquid sheet breaks up into small droplets, the external disturbances no longer have much effect on the droplet size. That means the effect of external disturbances on the liquid breakup region is

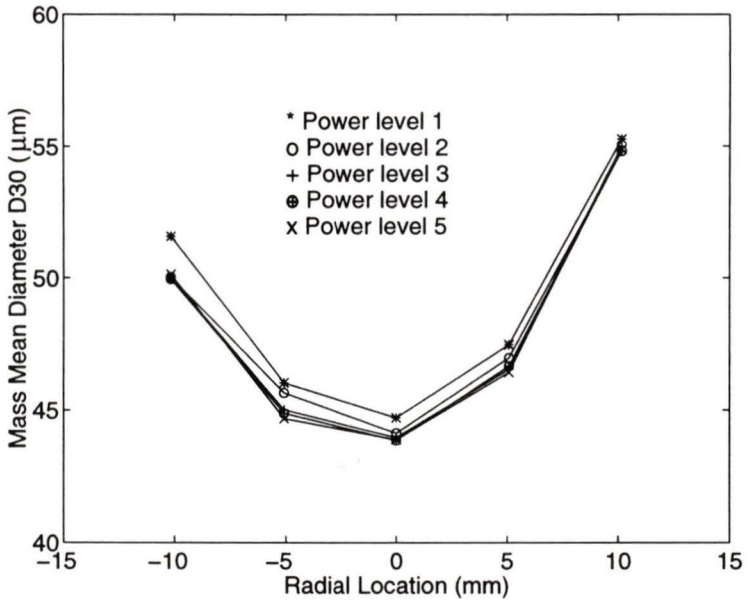

Figure 4.23: Radial distributions of the mass mean diameter for the baseline pressure-swirl nozzle measurement with acoustic excitations. $p = 0.4$ MPa (60 psi), $f_a = 19$ kHz, $x = 0$, $y = 0$, $z = 25.4$ mm (1 inch), power level as shown.

most important and significant.

Figure 4.23 shows an indication of the effect of the acoustic power output levels on the radial distributions of mass mean diameter (D_{30}) for the baseline pressure-swirl atomizer at injection pressure of 0.4 MPa (60 psi) and axial location of 25.4 mm (1 inch) from the atomizer exit. The acoustic frequency is fixed at 19 kHz. Shown in Figure 4.24 is the trend of mass mean diameter variation with acoustic power output for the baseline pressure-swirl nozzle under the same test conditions. The acoustic frequency is fixed at 10 kHz. It is seen that different acoustic power levels do have some effect on the mass mean diameter in both figures, but the amount of change seems to be relatively small. This result is similar to those reported by Takahashi, et al. [12]. The more powerful the excitations, the smaller the droplets are so formed (Figures 4.23 and 4.24), even though the reduction of mass mean diameter is not

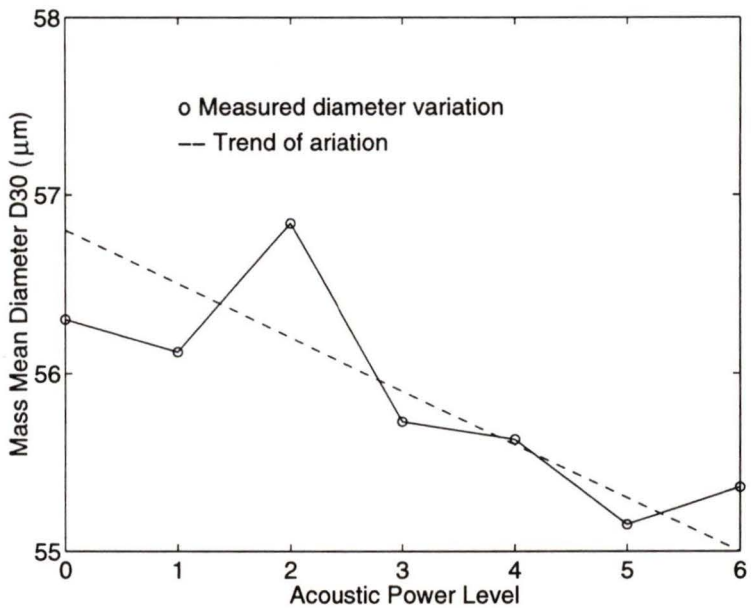

Figure 4.24: Variation of the mass mean diameter for the baseline pressure-swirl nozzle measurement with acoustic excitations. $p = 0.4$ MPa (60 psi), $f_a = 10$ kHz, $x = 0$, $y = 0$, $z = 25.4$ mm (1 inch).

significant. This can be explained by the instability analysis in Appendix B.

4.4 Summary

Both flow visualization and PDPA measurement reveal that external acoustic excitations do have effect, though quite small, on the breakup process of the conical liquid sheet and the resulting droplet sizes of the sprays produced by the baseline pressure-swirl atomizer. This reinforces the discussion in the introduction section that it is NOT sufficient to achieve the desired droplet size reduction by either the pressure-swirl atomization or external excitation alone. A proper combination of the atomizer structure design (that is, atomization process organization) and external excitation (frequency and amplitude) may potentially achieve the goal of desired droplet sizes,

even though it may be difficult (Appendix B). That is, the present atomizer plus external excitation is not enough. As a result, new atomizers with appropriate geometrical configuration have been designed, and the resulting spray characteristics have been investigated. The details will be described in the next chapter.

Chapter 5

MODIFIED PRESSURE-SWIRL ATOMIZERS

As discussed earlier, pressure-swirl atomization is a complex process in which the atomizer structure, turbulence, cavitation, as well as boundary layer development all have their influence as the seeds of initial disturbances before the liquid is discharged from the nozzle orifice. Once the liquid is discharged from the atomizer, the subsequent development of disintegration process is mainly influenced by its initial velocity and the physical properties of the liquid and the ambient gas. The liquid velocity or momentum is affected by aerodynamic interactions at the interface of the liquid and the gas phases. To improve the spray formation process it is necessary to have better atomizer structure design and aerodynamic interactions by inducing external disturbances to promote the excitational development of unstable waves on the liquid sheet surface.

In Chapter 4 it is shown that the baseline pressure-swirl nozzle with external acoustic excitations is not sufficient to achieve the desired reduction of droplet sizes. It is hoped that proper atomizer structure design plus external excitations may po-

tentially reduce the droplet sizes and improve the characteristics of the spray. In this chapter, new geometrical designs of the inserts based on the baseline pressure-swirl nozzle will be given and the results by visualization techniques and PDPA measurements will be presented.

5.1 Nozzle Design

As discussed earlier (section 4.1), the formation of the conical liquid sheet begins inside the swirling chamber where the pressurized liquid obtains axial and tangential velocities. The balance of momentum in the axial and radial directions eventually determines the spray angle. The process of pressure-swirl atomization is very complex but the controlling mechanism may be described as following: i) Inside the swirling chamber, the fluid motion is controlled by a combination of the liquid parameters, such as liquid pressure and liquid properties, and the chamber geometry which may cause turbulence and cavitation. Turbulence has the potential to cascade the kinetic energy into smaller scales which lead to preparation of the liquid breaking up into smaller droplets. The cavitation effect basically enhances the irregularity of the fluid motion therefore it may also has the potential to improve the resulting liquid atomization. To enhance the degree of turbulent motion, a convex tip with specific shape can be made on top of the insert, in addition to proper slot angle and geometrical considerations. This convex can cause liquid separation and recirculation. But this may have another effect which reduces the spray angle because the kinetic energy loss results in loss of liquid velocity, especially the tangential velocity, of the fluid motion. ii) Once the liquid is discharged outside of the atomizer orifice, the breakup mechanism is mainly controlled by aerodynamic interactions between the liquid and the ambient air. This is based on the condition of high velocity, and low viscosity, or high Weber number

Table 5.1: Parameters of different insert designs used in this experiment

	Slot #	Slot Angle (deg)	Slot Width (mm)	Slot Depth (mm)
Insert # 1	4	30	0.254 (0.01")	0.3
Insert # 2	6	45	0.152 (0.006")	0.3
Insert # 3[1]	4	60	0.254 (0.01")	0.3

and Reynolds number. External excitations can enhance the disturbances on the liquid sheet such that they intensify the aerodynamic interactions.

For practical applications, it is even more complex because there exists other factors which may have significant influence on the breakup mechanism. In this chapter, a combination of the original nozzle outer housing with different insert designs was developed to investigate the nozzle geometric effect on the final liquid atomization. Figure 5.1 demonstrates one of the insert designs in which the following four parameters - slot number, slot angle, slot width and depth - are emphasized. In this experiment, three different inserts were used, and the parameters of these designs are listed in Table 5.1.

5.2 Test Conditions and Procedures

The test conditions are the same as those in Chapter 4 for the baseline pressure-swirl nozzle so that the results may be comparable. Since the nozzle geometric design is different, the liquid flow rate and overall flow characteristics may differ as well.

Measurements for the modified pressure-swirl atomizers are conducted following the procedures for the baseline pressure-swirl atomizer. First the spray characteristics are investigated by both flow visualization and PDPA measurement without

[1] A small tip is made on top of it.

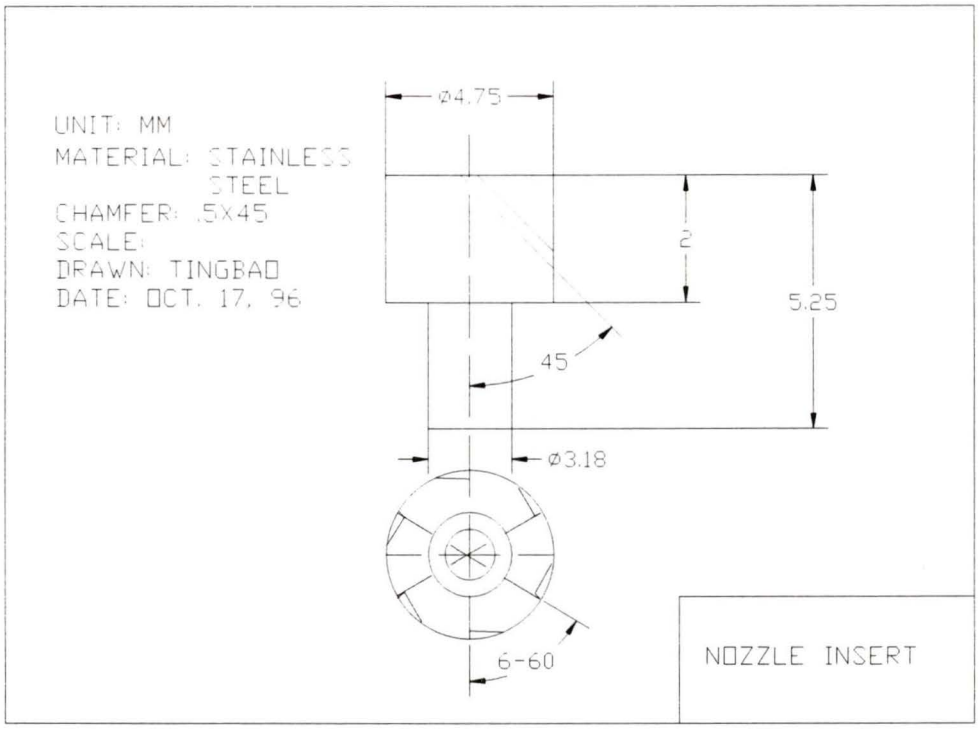

Figure 5.1: Geometric structure of one of the inserts of the modified pressure-swirl atomizer.

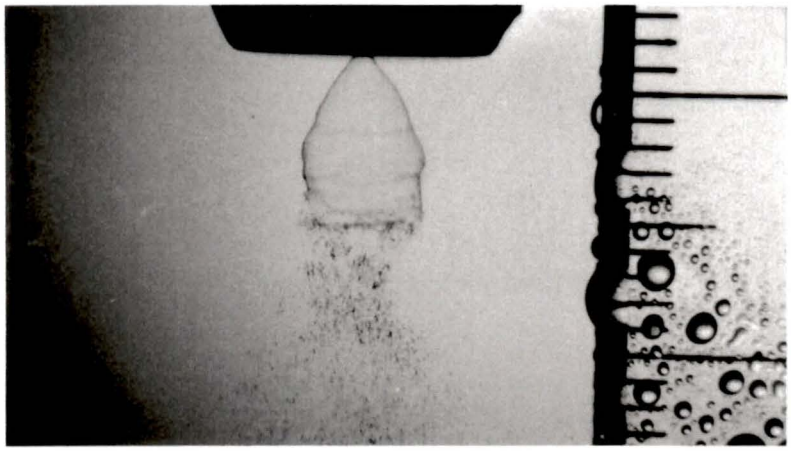

Figure 5.2: Photograph of the spray produced by the modified pressure-swirl atomizer with Insert # 3 without acoustic excitations. $p = 0.4$ MPa (60 psi).

any acoustic excitations. The results are then compared with the baseline measurements presented in the previous chapter. Finally, the effect of acoustic excitations is investigated by changing the acoustic frequency while keeping the power level and measurement location fixed.

5.3 Results and Discussion

5.3.1 Photographic Observations

Stroboscopic back-lit visualization as well as photographs reveal that the spray produced by the modified pressure-swirl atomizers is very symmetric. Exciting motion (regular and successive contraction and expansion) of the conical liquid sheet is observed right at the nozzle exit. This contraction or expansion makes the waves on the conical liquid sheet surface conspicuous with large amplitudes. This seemingly periodic and symmetric wave motion may be caused by the symmetric distribution of the insert slots in the modified pressure-swirl atomizers.

Shown in Figures 5.2 through 5.5 are photographs of the modified pressure-swirl

Figure 5.3: Photograph of the spray produced by the modified pressure-swirl atomizer with Insert # 3 without acoustic excitations. $p = 0.4$ MPa (60 psi).

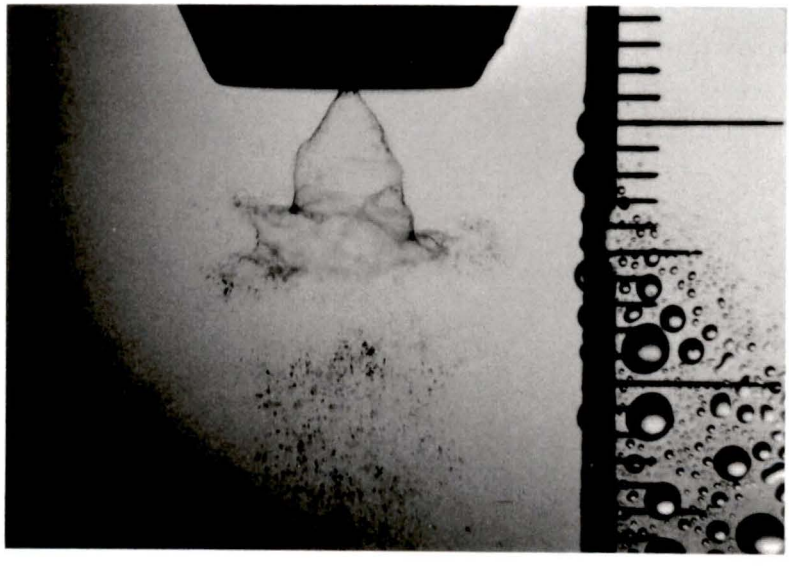

Figure 5.4: Photograph of the spray produced by the modified pressure-swirl atomizer with Insert # 3 without acoustic excitations. $p = 0.4$ MPa (60 psi).

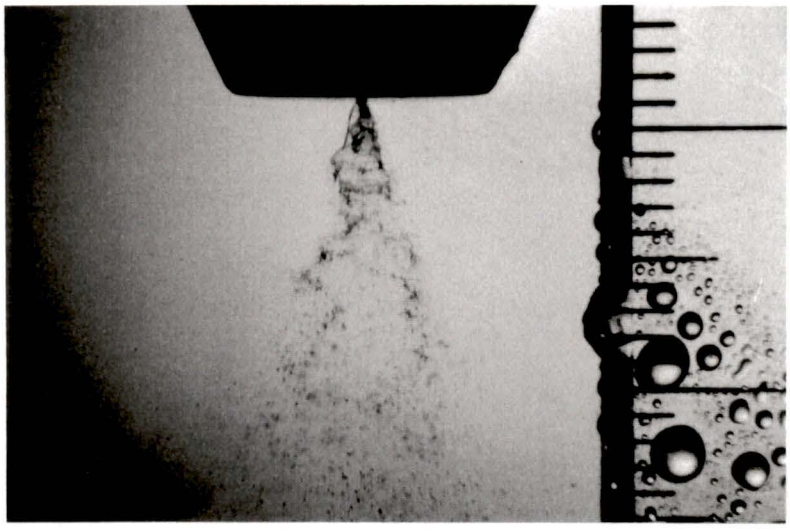

Figure 5.5: Photograph of the spray produced by the modified pressure-swirl atomizer with Insert # 3 without acoustic excitations. $p = 0.4$ MPa (60 psi).

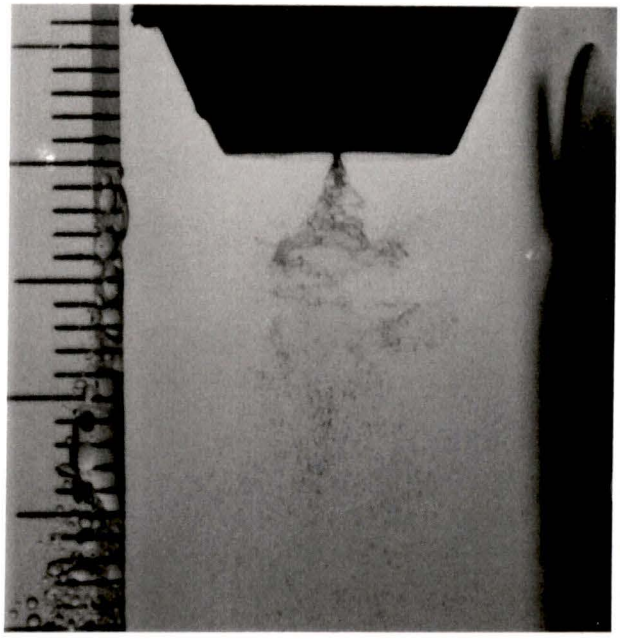

Figure 5.6: Photograph of the spray produced by the modified pressure-swirl atomizer with Insert # 3 with acoustic excitations. $p = 0.4$ MPa (60 psi), $f_a = 60$ Hz, power level 3.

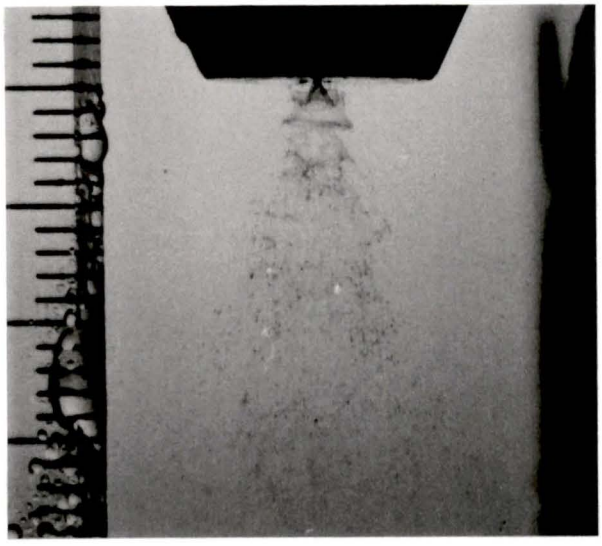

Figure 5.7: Photograph of the spray produced by the modified pressure-swirl atomizer with Insert # 3 with acoustic excitations. $p = 0.4$ MPa (60 psi), $f_a = 240$ Hz, power level 4.

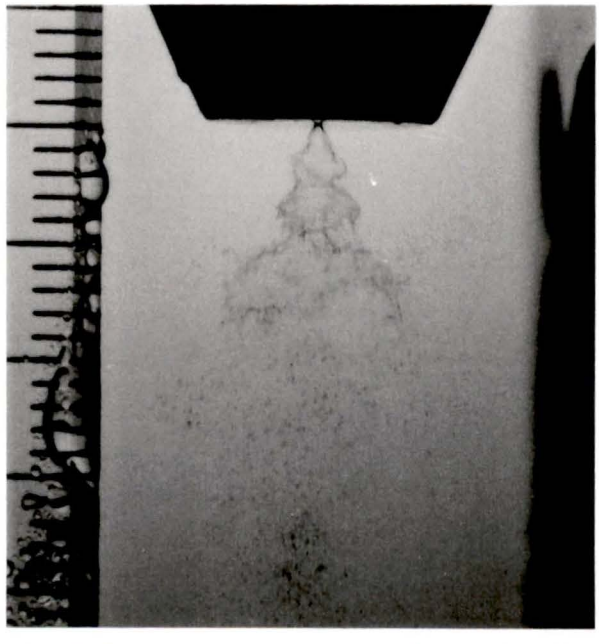

Figure 5.8: Photograph of the spray produced by the modified pressure-swirl atomizer with Insert # 3 with acoustic excitations. $p = 0.4$ MPa (60 psi), $f_a = 240$ Hz, power level 4.

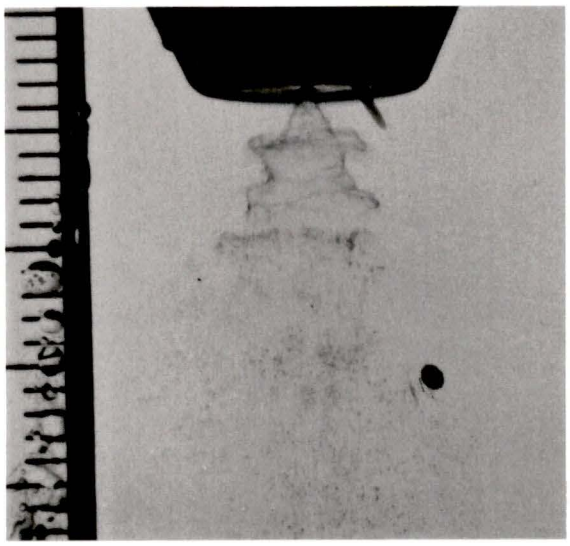

Figure 5.9: Photograph of the spray produced by the modified pressure-swirl atomizer with Insert # 3 with acoustic excitations. $p = 0.4$ MPa (60 psi), $f_a = 600$ Hz, power level 4.

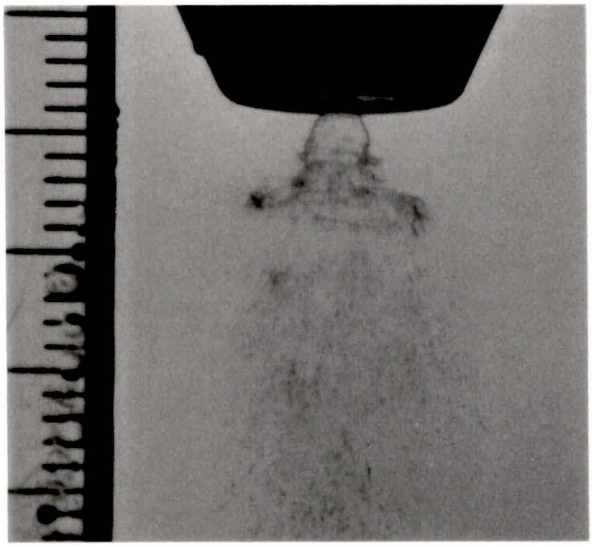

Figure 5.10: Photograph of the spray produced by the modified pressure-swirl atomizer with Insert # 3 with acoustic excitations. $p = 0.4$ MPa (60 psi), $f_a = 1$ kHz, power level 5.

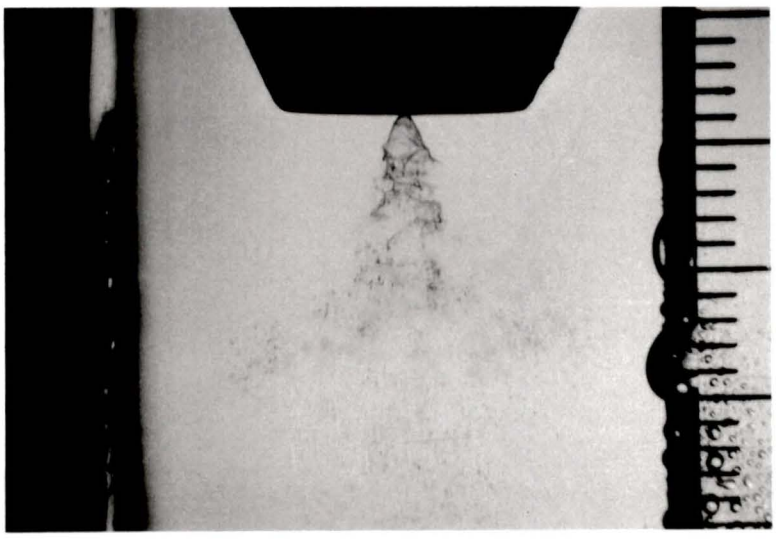

Figure 5.11: Photograph of the spray produced by the modified pressure-swirl atomizer with acoustic excitations. $p = 0.4$ MPa (60 psi), $f_a = 1$ kHz, power level 3.

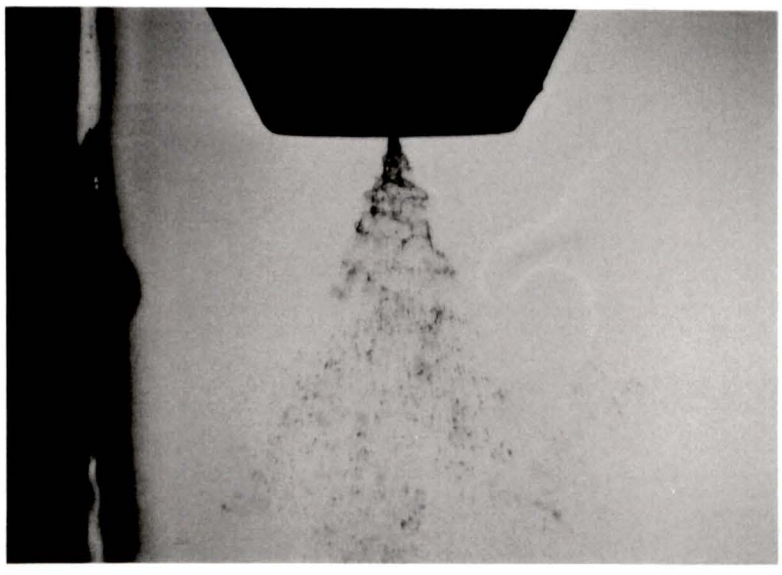

Figure 5.12: Photograph of the spray produced by the modified pressure-swirl atomizer with acoustic excitations. $p = 0.4$ MPa (60 psi), $f_a = 1$ kHz, power level 3.

Figure 5.13: Photograph of the spray produced by the modified pressure-swirl atomizer with acoustic excitations. $p = 0.4$ MPa (60 psi), $f_a = 1$ kHz, power level 3.

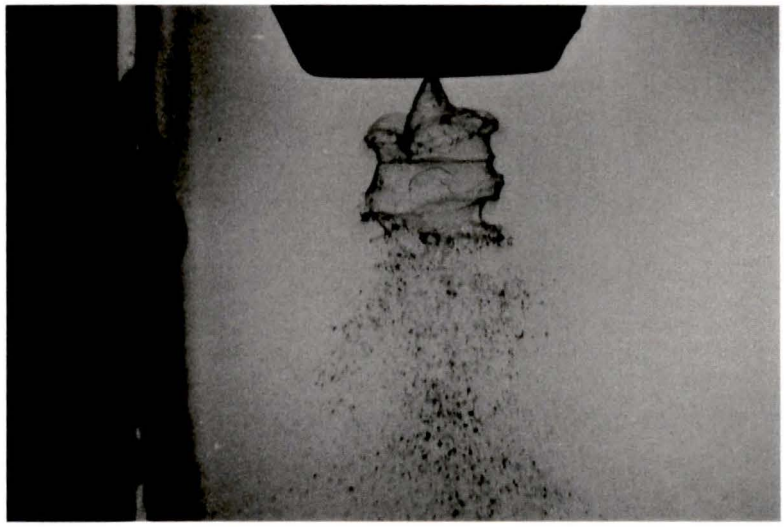

Figure 5.14: Photograph of the spray produced by the modified pressure-swirl atomizer with acoustic excitations. $p = 0.4$ MPa (60 psi), $f_a = 5$ kHz, power level 3.

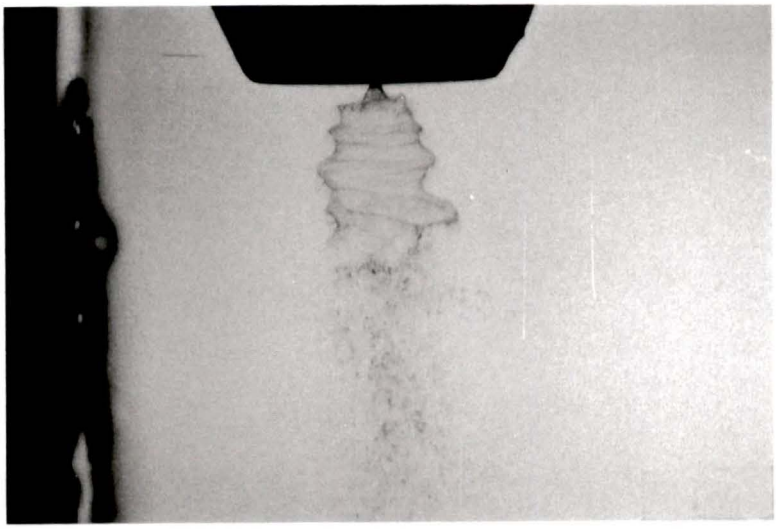

Figure 5.15: Photograph of the spray produced by the modified pressure-swirl atomizer with acoustic excitations. $p = 0.4$ MPa (60 psi), $f_a = 5$ kHz, power level 3.

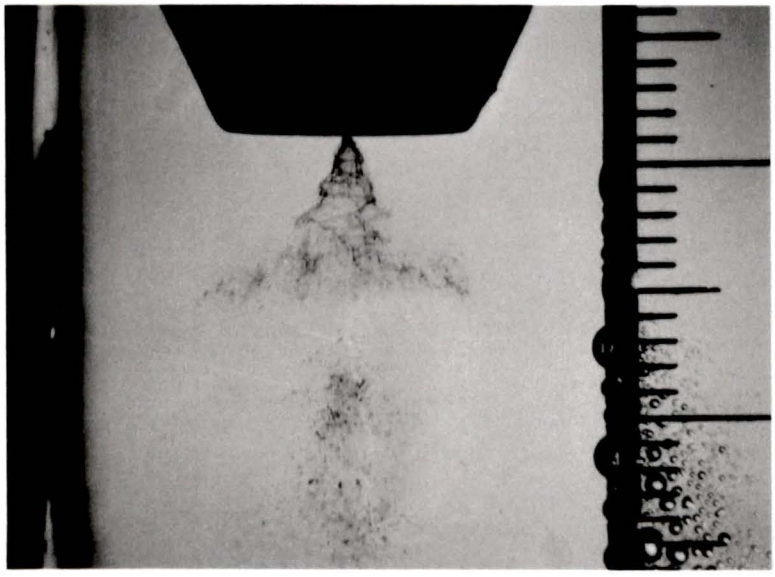

Figure 5.16: Photograph of the spray produced by the modified pressure-swirl atomizer with acoustic excitations. $p = 0.4$ MPa (60 psi), $f_a = 5$ kHz, power level 5.

atomizer without acoustic excitations, with injection pressure of 0.4 MPa (60 psi). The atomizer uses an insert of 6 slots with 45° slot angle. Very symmetric liquid sheet surfaces can be seen from these pictures and the breakup occurs almost at the same distance on both sides of the picture from the atomizer exit. On the liquid sheet surface, Kelvin-Helmholtz waves develop in a more regular manner than the baseline pressure-swirl atomizer. Figure 5.4 shows a pattern of combination of the so-called perforated-sheet and wavy-sheet disintegration [1]. Figure 5.5 catches the instant of contraction of the conical liquid sheet and irregular wave shape can also be seen. Figure 5.6 shows the case of the same atomizer with acoustic excitations applied. The frequency of the acoustic signal was 60 Hz and the power output was set to level 3. It is the instant at which the liquid sheet contraction occurs. It is clearly seen that the strong swirling motion twists the conical liquid sheet into a bell type of shape. In Figures 5.7 and 5.8, acoustic excitations of 240 Hz frequency and level 4 power output were applied and large wave amplitude can be seen. Comparable wave length of about 2 mm can also be observed from these pictures, even though the spray angle seems different. In Figure 5.9, the frequency of acoustic disturbances was 600 Hz and the speaker power output was set to level 4. Large wave amplitude can be observed and the wave length is comparable with those in Figures 5.7 and 5.8. Figure 5.10 reveals a sudden expansion of the liquid sheet as acoustic perturbation of 1 kHz frequency and level 5 power output was exerted. This explosion-like-occurrence may be caused by large centrifugal forces created by the swirling motion. Figures 5.11 through 5.16 give the situations of the spray produced by the same atomizer under the same flow conditions, with acoustic excitations of different frequencies and different power levels. Similar spray pattern (or wave forms) can be seen from these pictures. This strongly suggests the existence of the acoustic effect on the development of aerodynamic instabilities on the liquid sheet surface which dominate the breakup process.

5.3.2 PDPA Measurements

Prior to conducting experiment with acoustic excitations, measurements were made to obtain basic information of the modified pressure-swirl atomizers, such as spray symmetry, diameter distributions, velocity distributions, and so on.

Figure 5.17 presents the distributions of mass mean diameter along the radial locations of the sprays produced by the modified pressure-swirl atomizers with three different inserts without acoustic excitations. The flow conditions are the same as those for the baseline pressure-swirl nozzle. The injection pressure is 0.4 MPa (60 psi) and the measured axial locations are at 25.4 mm (1 inch) and 203.2 mm (8 inches) from the atomizer exit, respectively. Completely different distributions can be seen from this figure for the mass mean diameter at 25.4 mm (1 inch) from the nozzle exit, compared with the results of the baseline pressure-swirl nozzle. For these modified pressure-swirl atomizers, the mass mean diameter distributions at 25.4 mm (1 inch) from the nozzle exit have only one peak which fall at the centerline, while the diameter distributions at the same axial location for the baseline pressure-swirl nozzle have two peaks which fall at the periphery of the conical liquid sheet and smaller droplets fall at the centerline. This explains the visual observations that there exists a moment at which the liquid sheet contracts to the centerline, as seen in Figures 5.5, 5.6, 5.11 and 5.12. In Figure 5.18, the corresponding velocity distributions are presented. It is consistent that large droplets at the centerline have high velocity. Video visualization also shows that strong entrainment occurs in the spray motion which brings the droplets towards the centerline. The overall pattern of the modified pressure-swirl atomizers can be drawn from Figures 5.17 and 5.18 that the higher the droplet velocity, the larger the droplet diameter.

Figure 5.19 shows the histogram of diameter distributions for modified pressure-swirl atomizer with insert # 1 at the edge of the spray ($x = -11.43$ mm (-0.45 inches)

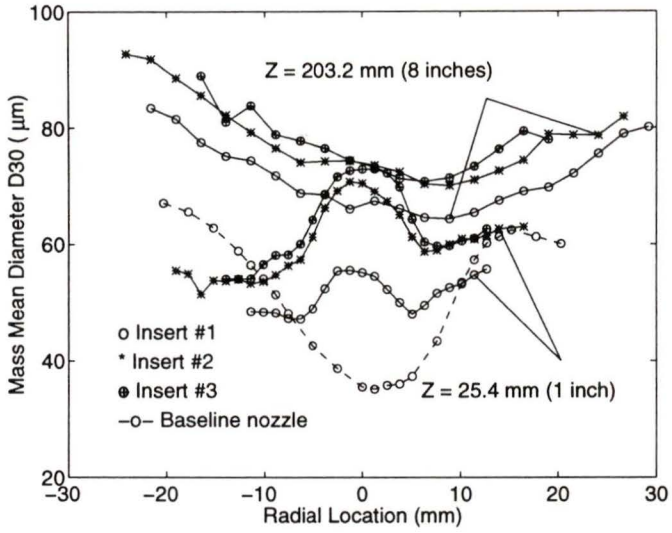

Figure 5.17: Mass mean diameter distributions for the modified pressure-swirl atomizer with insert # 1, # 2 and # 3 without acoustic excitations. The dashed curve represents the mass mean diameter distribution for the baseline pressure-swirl nozzle with acoustic excitations: $f_a = 7.0$ kHz, power level 2.

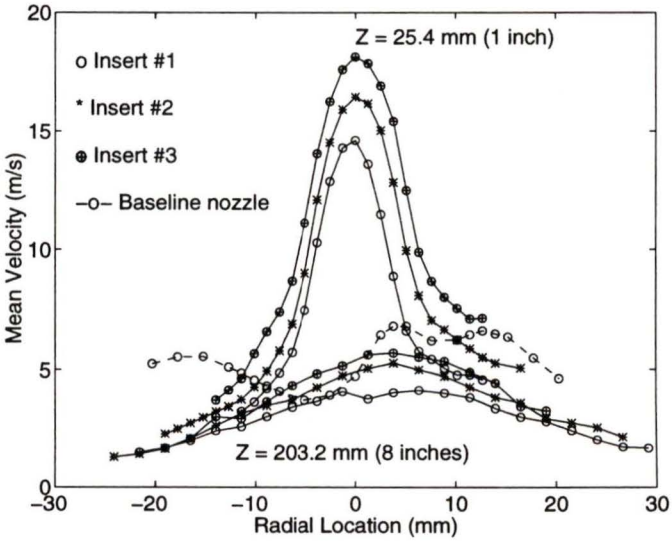

Figure 5.18: Velocity distributions for the modified pressure-swirl atomizer with insert # 1, # 2 and # 3 without acoustic excitations. The dashed curve represents the velocity distribution for the baseline pressure-swirl nozzle with acoustic excitations: $f_a = 7.0$ kHz, power level 2. $z = 25.4$ mm (1 inch).

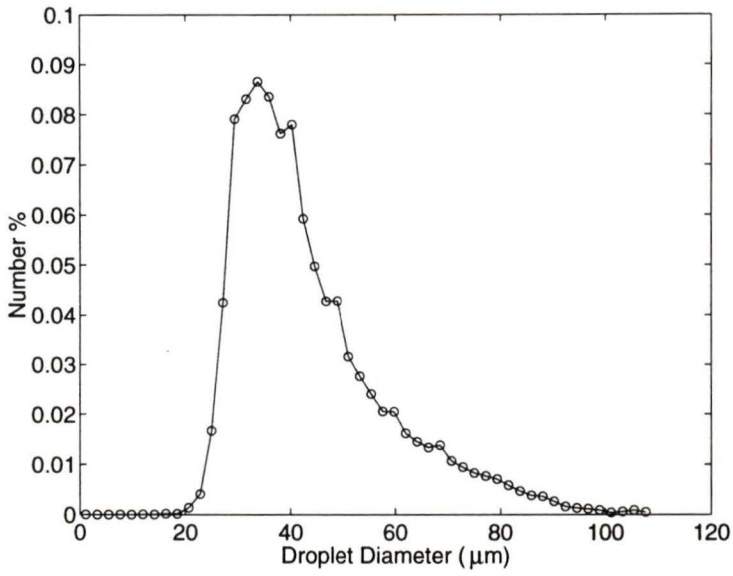

Figure 5.19: Diameter histogram of the modified pressure-swirl atomizer with Insert # 1 at the edge of the spray without acoustic excitations. $x = -11.43$ mm (0.45 inches), $y = 0$, $z = 25.4$ mm (1 inch).

at the axial location of $z = 25.4$ mm (1 inch)). Figure 5.20 gives the corresponding diameter histogram at the centerline ($x = 0$). Clearly, the histogram of diameter distribution for the modified atomizer at the centerline looks like that of the baseline nozzle at the edge locations (refer Figure 4.16), while the histogram of the modified atomizer at the edge of the spray seems similar to that of the baseline nozzle at the centerline (Figure 4.15). From these two figures it is evident that even though the peak droplet number is located at small droplets, whether measured at the centerline or at the edge, the mean diameter is still very large due to the large droplet weighting effect.

Figures 5.21 through 5.23 give the variations of mass mean diameter with the acoustic frequency for three different inserts. Each curve represents the mass mean diameter at the same axial location ($z = 203.2$ mm (8 inches)) but different radial locations. The injection pressure is 0.4 MPa (60 psi). The power output of the

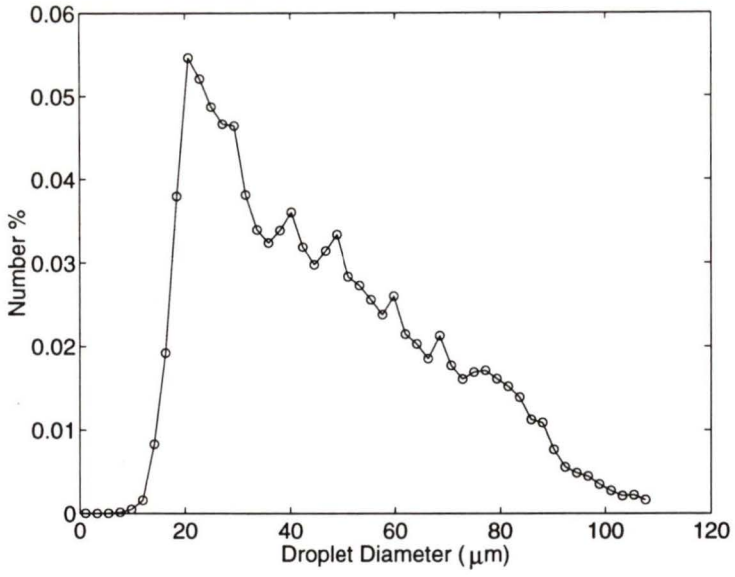

Figure 5.20: Diameter histogram of the modified pressure-swirl atomizer with Insert # 1 at the centerline of the spray without acoustic excitations. $x = 0$, $y = 0$, $z = 25.4$ mm (1 inch).

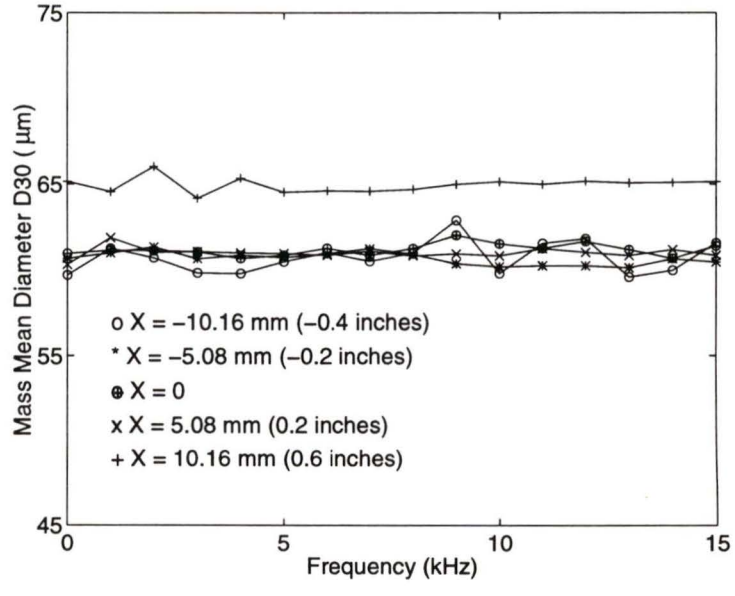

Figure 5.21: Mass mean diameter for the modified pressure-swirl atomizer of insert # 1 with acoustic excitations applied. $p = 0.4$ MPa (60 psi), power level 3, $z = 203.2$ mm (8 inches), $y = 0$, x as shown.

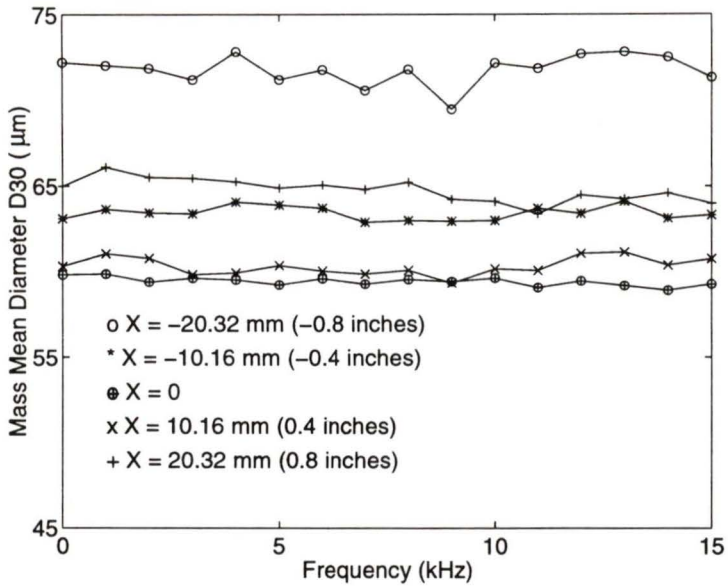

Figure 5.22: Mass mean diameter for the modified pressure-swirl atomizer of insert # 2 with acoustic excitations applied. $p = 0.4$ MPa (60 psi), power level 3, $z = 203.2$ mm (8 inches), $y = 0$, x as shown.

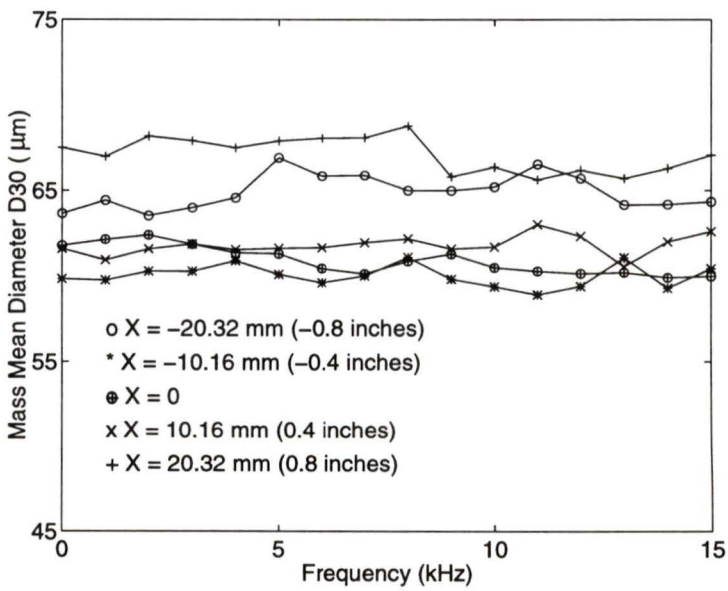

Figure 5.23: Mass mean diameter for the modified pressure-swirl atomizer of insert # 3 with acoustic excitations applied. $p = 0.4$ MPa (60 psi), power level 3, $z = 203.2$ mm (8 inches), $y = 0$, x as shown.

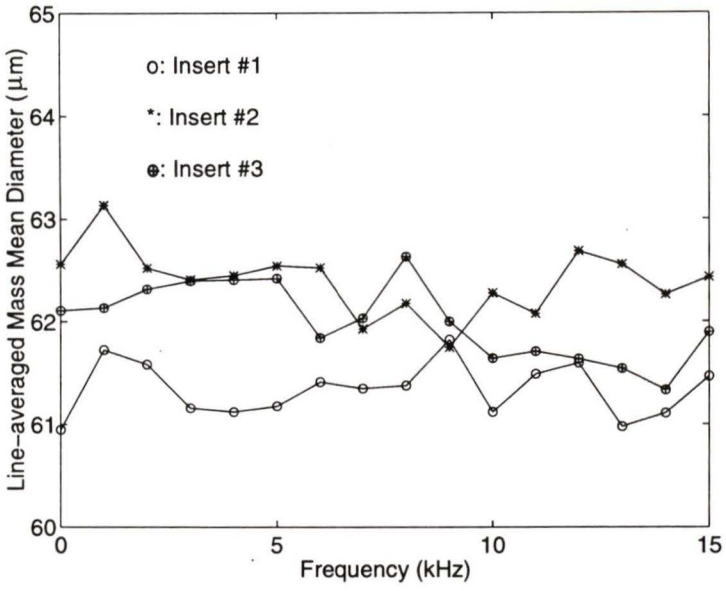

Figure 5.24: Line-averaged mass mean diameter for the modified pressure-swirl atomizer of three different inserts with acoustic excitations applied. $p = 0.4$ MPa (60 psi), power level 3, $x = 0$, $y = 0$, $z = 203.2$ mm (8 inches).

acoustic disturbances is set to level 3. It is seen that there is not significant change in diameter with and without acoustic excitations, as noted for the baseline pressure-swirl nozzle. Similar variations can be seen from Figure 5.24 for the line-averaged mass mean diameters of the three different atomizer assemblies.

5.4 Summary

Similar to the baseline pressure-swirl nozzle, the modified pressure-swirl atomizers with three different inserts do not give significant reduction of droplet sizes as expected. But as discussed above, the symmetry of the spray is achieved by the modified pressure-swirl atomizers and new spray pattern is observed. Exciting oscillation of the conical liquid sheet could be helpful for improving the atomization process. Strong swirling motion can enlarge the spray angle and strong entrainment is ob-

served which can increase the spray penetration. Visualization reveals that the whole spray pattern of the modified pressure-swirl atomizers is more symmetric and regular.

Photographic techniques confirm the external excitation effect on the aerodynamic instability development on the liquid sheet surface, similar to the baseline pressure-swirl nozzle. Unfortunately, both pressure-swirl atomizers cannot reduce the line-averaged mass mean diameter dramatically at low injection pressures. For Johnson's aerosol products, pressure-swirl atomizer may not be the satisfactory solution for the droplet diameter reduction and the spray performance improvement without chemical additives. To relieve the environmental pollution problem due to the use of chemical propellants in the aerosol products, new atomization technique may have to be explored, because of the poor atomization of pressure-swirl atomizer at low injection pressures. That is how the new-concept atomizer comes in. This new-concept impaction atomizer can reduce the droplet diameter dramatically and the spatial uniformity of the spray is achieved far better than that of the spray produced by the pressure-swirl atomizer. This is confirmed by PDPA measurement as well as by Johnson's Malvern measurement. The new-concept impaction atomization technique could be a good solution for Johnson's aerosol applications, to be detailed in the next chapter.

Chapter 6

NEW-CONCEPT IMPACTION ATOMIZER

For most industrial applications, such as combustion sprays in furnaces, pressure-swirl atomization is a well developed and mature technology which gives satisfactory characteristics of the spray such as droplet diameter and diameter distribution. For the aerosol applications, safety considerations limit the injection pressure which results in difficulties in obtaining fine and uniform sprays by pressure-swirl atomization. Even though theoretically it is possible to reduce the droplet diameters by exerting external disturbances, such as external acoustic excitations, and photographic evidence confirms this possibility, practical difficulties exist in finding the proper combination of frequency and amplitude of the disturbances, since the condition causing resonance or collapse of the liquid sheet produced by pressure-swirl atomizer is extremely dependent on the testing conditions and the specific experimental system. Any attempt is difficult because the resonance range of frequency is narrow and the procedure is extremely tedious, time consuming and expensive.

A liquid jet or drop impacting on a solid object will lead to collapse of the jet

or drop. This common phenomenon can be observed almost everywhere in daily life, for example, rain falling on a roof creates splash with smaller droplets bouncing out in different directions, depending on the roof shape and the impaction angle. This leads to the present attempt at investigating this impaction phenomenon for potential application in the aerosol atomization.

6.1 Introduction

In 1960, Sir Geoffrey Taylor showed that when two equal cylindrical liquid jets collide they form an expanding liquid sheet in elliptical or round shape depending on the colliding angle [31]. This study gives a detailed theoretical analysis of the phenomena of impingement of two liquid jets. Earlier studies of impingement of two liquid sheets was conducted back to 1890 by Mitchell [32]. But Taylor only studied the development of the formed sheet without consideration of breakup or atomization further down stream following the liquid sheet. This implies that the liquid jet velocities are not very high and the liquid viscosity may have to be high. Thinking about that case with high jet velocity and low liquid viscosity, the impingement will form smaller liquid sheet and collapse or atomization will occur quickly due to the impaction and sudden exchange of momentum.

In this chapter, investigation is made in a course of attempt to study the case of a liquid jet stream, produced by a small round hole, impacting on a solid flat surface. For aerosol applications, the liquid jet stream is directed to the solid surface at a certain angle so that most of the resulting smaller droplets will bounce out in the same direction. The experiment is focused on the effect of the impaction length (from the injection nozzle exit to the impaction point on the plate) and the incident angle on the resulting spray characteristics. Visualization techniques were used and

PDPA measurements were conducted.

6.2 Theoretical Analysis

The impaction concept atomizer is based on the idea that collision between two objects will change their kinematic and dynamic properties. If two solid objects which are not deformable collide in an axis, their momentum will be conserved before and after the collision, which is given by

$$m_1\mathbf{u}_1 + m_2\mathbf{u}_2 + m_1\mathbf{u}_1' + m_2\mathbf{u}_2' = 0 \tag{6.1}$$

where m_1, m_2 are the masses of the two objects, respectively, $\mathbf{u}_1$, $\mathbf{u}_2$ are their velocity vectors before the collision, and $\mathbf{u}_1'$, $\mathbf{u}_2'$ are their velocity vectors after the collision.

Assume that $m_2 >> m_1$ and $\mathbf{u}_2 = 0$, $\mathbf{u}_2' = 0$ (here the second object with mass m_2 could be corresponding to the impaction plate which is fixed at certain location from the injection nozzle), then the momentum change of the first, smaller object can be determined by

$$m_1\mathbf{u}_1 + m_1\mathbf{u}_1' = 0 \tag{6.2}$$

or

$$\mathbf{u}_1 = -\mathbf{u}_1' \tag{6.3}$$

It means that the amplitude of the velocity does not change after the collision, but its direction changes 180^o. This is based on the assumption that the two objects have no deformation when they collide elastically.

Consider one of the individual droplets produced by the injection nozzle, the conservation of momentum can be expressed as

$$m_0\mathbf{u} = \sum_{i=1}^{M} m_i\mathbf{u_i} + m_s\mathbf{u_s} \tag{6.4}$$

where m_0 represents the mass of one of the individual droplets before impaction and $\mathbf{u}$ its velocity, m_i the ith droplet after the impaction and $\mathbf{u_i}$ its velocity; M the total number of droplets after the impaction; m_s the mass of the amount of water stick on the plate and $\mathbf{u_s}$ its velocity.

For this case, individual almost spherical liquid droplets continuously collide with the impaction plate. Because the liquid droplets are completely deformable (the impaction plate can be considered nondeformable for this case), most of the liquid mass stick on the plate surface and form a thin liquid sheet (A special type of Taylor's impingement [31]) with a wave type of motion propagating from the impinging point. These ripples can be clearly seen from the photographs and the shapes of the ripples change from round circles to ellipsoids when the impaction angle changing from the right angle to less than 90 degrees. The smaller the impaction angle, the longer the major axis of the ellipsoids. The impaction angle is defined by the liquid droplet stream and the impaction plate from the incident direction (Figure 6.4). After a certain distance in the radial direction from the impinging point, the liquid loses its momentum (velocity) due to viscous friction and forms a thick rim at the edge of the ripples under surface tension forces.

Besides the liquid sheet formed on the impaction plate, a portion of the liquid mass is bounced back in certain direction in the form of fine droplet cloud. This portion of liquid breaks up into very uniform fine droplets when the larger, individual droplets collide with the impaction plate. After the impingement, the individual droplets collapse into smaller ones and some of them lose their velocity due to collision direction as well as their location after the collision. Others gain high enough velocity so that they overcome the surface tension forces and fly out in different directions from the impaction point. Observation shows that these droplets are very small and the spray so formed are very uniform (as confirmed by PDPA measurement later). This

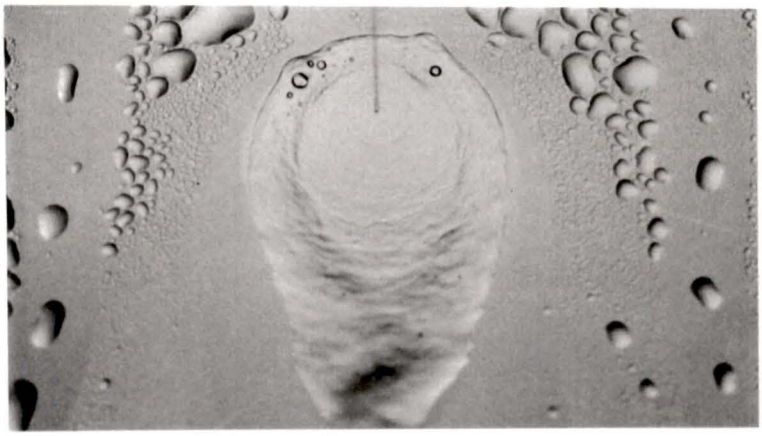

Figure 6.1: Photograph of the ripples created by the new-concept impaction atomizer

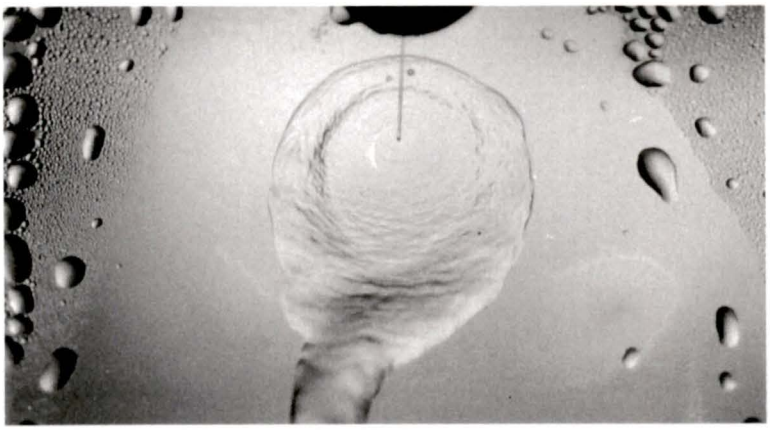

Figure 6.2: Photograph of the ripples created by the new-concept impaction atomizer

phenomenon of perfectly uniform sprays obtained from the impingement is beyond the detailed theoretical and mathematical description at present.

6.3 Experimental Apparatus

The devices used in this new-concept impaction atomization are designed in two different sketches as shown in Figures 6.3 and 6.4. Both two devices give similar atomization characteristics - the spray is very fine and uniform. The tube-type device

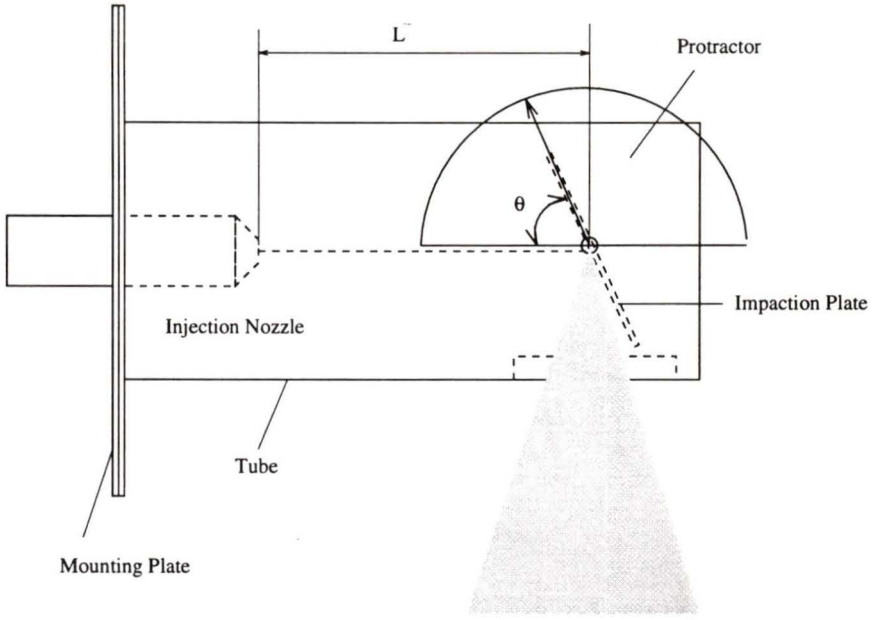

Figure 6.3: Tube-type device of the new-concept impaction atomizer

is used to study the effect of impaction angle by adjusting the plate angle (θ). The impaction angle is then read from the protractor fastened on the plate. The plate-type device is used to investigate the impaction length effect on the resulting atomization. Both results will be presented in the results and discussion section (6.4). The effect of the injection nozzle will also be discussed analytically.

The injection pressure of 0.4 MPa (60 psi) is used and the whole experiment is carried out under room temperature such that consistency is assured and uncertainty caused by test conditions is negligible.

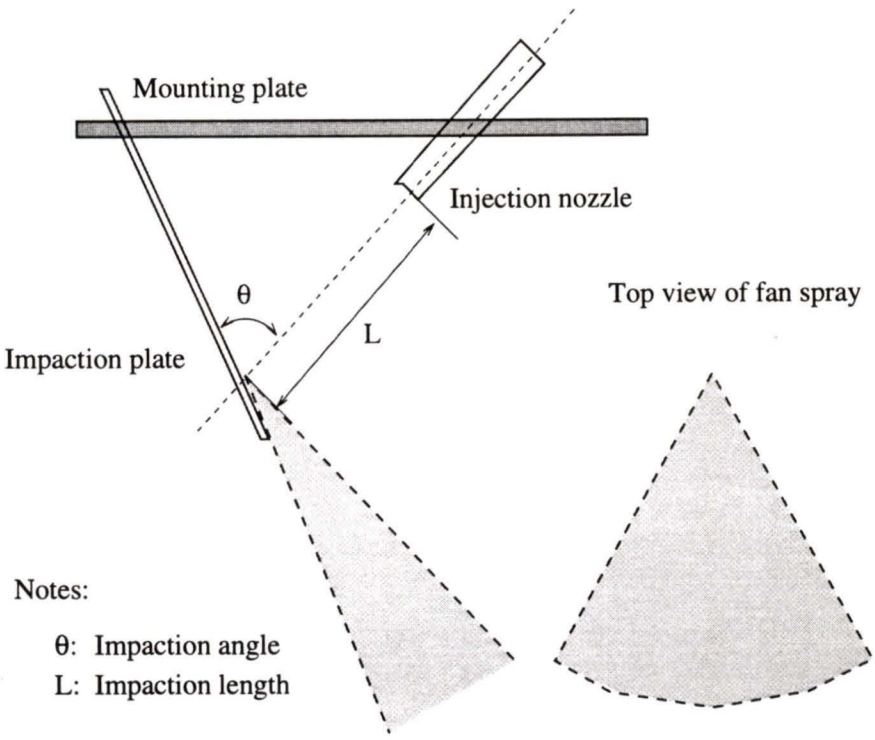

Figure 6.4: Plate-type device of the new-concept impaction atomizer

6.4 Results and Discussion

6.4.1 Effect of Impaction Angle on Atomization

Figure 6.5 gives the mean diameter distributions along the radial locations for the impaction angle of 65° at the impaction length of 50.8 mm (2 inches). It is clearly seen that the mass mean diameter distribution is very uniform in the whole spray, showing a spray characteristics totally different from those of the pressure-swirl atomizer. The maximum variation of the mass mean diameters is about 5% for this case.

Figure 6.6 shows the effect of impaction angle on the droplet mean diameters in the resulting sprays. The injection pressure is 0.4 MPa (60 psi) and the injection nozzle is the outer housing of the baseline pressure-swirl nozzle (60°B 0.5) - that is, a circular orifice with a diameter of 0.2 mm. The measurement location is 203.2 mm (8 inches) downstream of the impaction point. The curves represent the variations of line-averaged mean diameters with the impaction angle. It is seen that an impaction angle of 65° gives the smallest line-averaged mean droplet diameters. Larger or smaller than this angle, the line-averaged mean diameters increase.

6.4.2 Effect of Impaction Length on Atomization

The influence of the impaction length on the spray produced by the new-concept impaction atomizer is mainly reflected by the momentum (velocity) of the individual droplets before impaction. The liquid jet discharged by a single round hole disintegrates into individual droplets at certain distance downstream. As is common knowledge, the impaction effect is not as strong for a continuous liquid column as for discontinuous individual droplet impaction. Therefore, if the impaction length is so short that the liquid jet does not break up into individual droplets before the

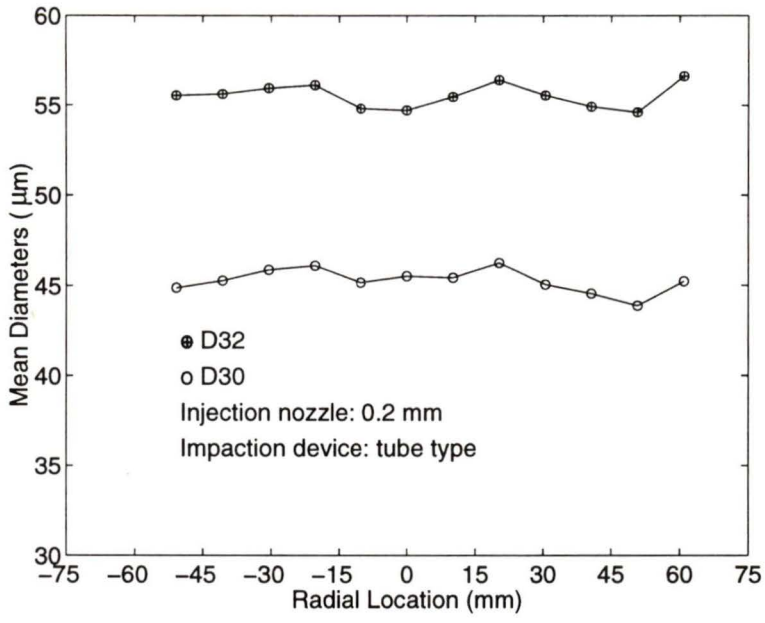

Figure 6.5: Mass mean diameter distributions along the radial locations of the spray created by the new-concept impaction atomizer. Injection pressure: 0.4 MPa (60 psi); impaction angle: 65°; impaction length: 50.8 mm (2 inches); measurement location: 203.2 mm (8 inches) from the impaction point.

impaction no spray may be produced. Once individual small droplets are formed and they impact on the flat plate, the shorter the impaction length, the finer the spray would be. This is because with shorter impaction length, the individual droplets have larger momentum. With an increase in the impaction length, the individual droplets will lose their momentum due to air drag effect. In Figure 6.7, the mean diameter distributions along the radial locations of the spray are presented. Similar diameter variations can be seen as in Figure 6.5. Figure 6.8 shows the variations of the line-averaged mean diameters with the impaction length. Clearly, by decreasing the impaction length, the line-averaged mean diameters are also decreased. This experiment shows that the shortest impaction length can reach 50.8 mm (2 inches). Less than this length, poor or even no spray is observed.

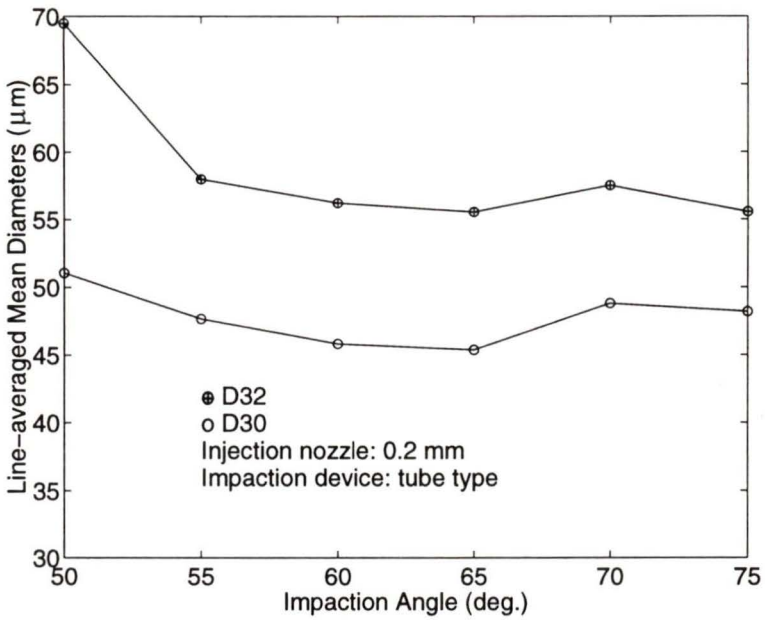

Figure 6.6: Line-averaged mean diameters as a function of the impaction angle for the new-concept impaction atomizer. Injection pressure: 0.4 MPa (60 psi); impaction length: 50.8 mm (2 inches); measurement location: 203.2 mm (8 inches).

6.4.3 Effect of Injection Nozzle Diameter on Atomization

The effect of the injection nozzle is that the smaller the pre-created individual droplets, the finer the final spray. With smaller pre-created individual droplets, the limited impaction length can also be reduced. But the drawback is that the penetration of the final spray is shorter, which is unexpected. With larger orifice of the injection nozzle, longer penetration distance of the final spray can be achieved but the droplet diameter will be larger. Therefore, for Johnson's aerosol applications, a proper choice of the injection nozzle opening can be determined by achieving fine, uniform spray and obtaining certain spray penetration.

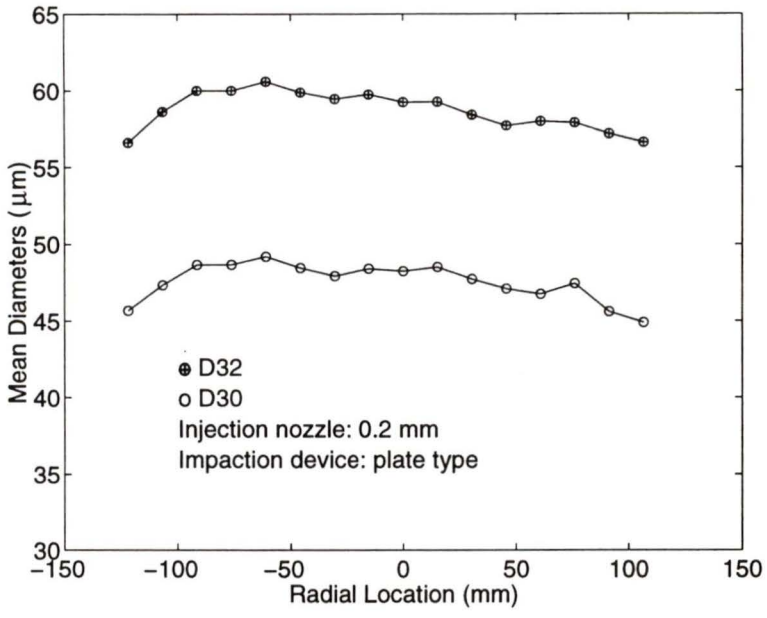

Figure 6.7: Mass mean diameter distributions along the radial locations of the spray created by the new-concept impaction atomizer. Injection pressure: 0.4 MPa (60 psi); impaction angle: 60°; impaction length: 50.8 mm (2 inches).

6.5 Problem of Impaction Atomization

The shortcoming of the new-concept impaction atomizer is that only about 30% of the discharged liquid is atomized into fine spray. The rest will accumulate by coalescence with the impaction plate. Attempt to recirculate or re-utilize the rest of the un-atomized liquid has been made and the mathematical calculations show that it is possible to recirculate the rest of the un-atomized liquid by the Venturi effect. Detailed calculations can be found in Appendix A. The recirculation of the dripping liquid by Venturi tube needs experimental verifications.

Another potential solution to the dripping problem may be the hand-pump pressurization system, which is easy to design and manufacture for aerosol products. It also needs experimental verifications.

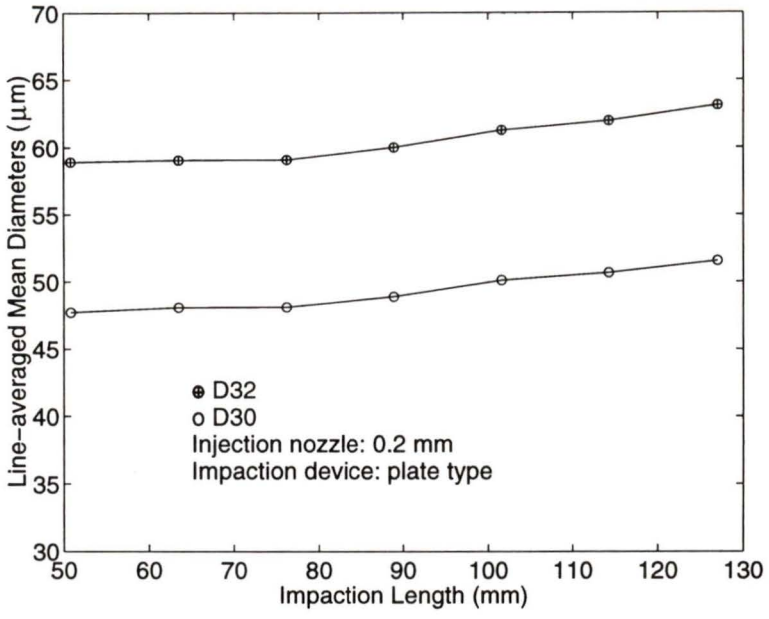

Figure 6.8: Line-averaged mass mean diameter distributions with impaction length for the new-concept impaction atomizer. Injection pressure: 0.4 MPa (60 psi); impaction angle: 60°; impaction length as shown.

6.6 Prototype Design

A prototype of the new-concept impaction atomization device has been designed and made in house (Figure 6.9). Two different injection nozzle designs have been demonstrated. This design is only intended to show the possibility of fitting the atomization device into Johnson's present products. The Venturi effect has not yet been tested due to difficulty in manufacturing with the available facilities in house. For actual volume production, the device can be made smaller and more handy with nicer appearance using plastic injection molding techniques.

Figure 6.9: Photograph of the prototype design of the new-concept impaction atomizer.

6.7 Summary

The new-concept impaction atomizer creates very fine and uniform spray such that it can be a good substitute for the atomization system of Johnson's aerosol products. The dripping problem can be potentially solved by applying Venturi tube to completely recirculate the dripping liquid. Theoretical analysis and mathematical calculations have been carried out to confirm the possibility of design based on Johnson's present product structure using the Venturi tube design (Appendix A). Another potential solution to the dripping problem could be the hand-pump pressurization system design to recirculate the dripping fluid easily. The new-concept impaction atomizer with either Venturi tube design or hand-pump pressurization system may have promising marketing value for Johnson's new aerosol products with quality spray performance without concerns for environmental impact.

Chapter 7

CONCLUSIONS AND RECOMMENDATIONS

7.1 Conclusions

7.1.1 Baseline Pressure-swirl Nozzle

Spray formation from the baseline pressure-swirl nozzle exhibits a random-like, irregular and un-symmetric characteristics with Kelvin-Helmholtz instability dominating the wave development on the conical liquid sheet surface. The irregularity is mainly caused by the randomly-made slots on the nozzle insert.

External acoustic excitations show effect on the instability development observed by back-lit visualization technique. These excitations modulate the wave motion on the liquid sheet surface and enlarges the wave amplitude. The PDPA measurements reveal that the reduction of droplet sizes under the effect of external acoustic excitations seems not significant.

7.1.2 Modified Pressure-swirl Atomizers

The modified pressure-swirl atomizers use three different insert designs in order to investigate the effect of different atomizer structure on the resulting spray characteristics. It is shown that the symmetrically oriented insert slots create symmetric spray pattern and enhances the swirling motion of the liquid inside the swirling chamber. This increases the droplet velocity thus the spray penetration as well. Due to the strong swirling motion, successive contraction and expansion of the liquid sheet is observed such that a solid-cone-like spray pattern is formed by the modified pressure-swirl atomizer. This is shown by both the flow visualization techniques and PDPA measurements.

As discussed for the baseline pressure-swirl nozzle, external acoustic excitations do have effect on the liquid breakup process, but significant reduction of the droplet diameter has not yet been verified by PDPA measurement. At certain frequencies, the droplet diameter is decreased; while at others it is increased, an observation similar to the results available in literature. The modified pressure-swirl atomizers achieve an overall spray pattern with more symmetric and regular spray characteristics but larger droplets were observed.

7.1.3 New-concept Impaction Atomizer

Based on the momentum exchange theory by collision between two objects, a new-concept impaction atomizer is developed. The droplet diameter and uniformity of the spray produced by the new-concept impaction atomizer is investigated and two main parameters influencing the spray are examined. It is shown that smaller droplets are produced by shorter impaction length. But there exists a limit below which poor or even no spray is created. The impaction angle has an optimized value of 65° at which

smallest droplets can be produced. This angle has to be less than 90° such that all the droplets formed can move in a certain direction, for the aerosol applications.

With the new-concept impaction atomizer, a dramatic reduction of about 20 μm in droplet diameter is achieved and the variation of droplet diameter in the whole spray is less than 5 μm. The dripping liquid created by the new-concept impaction atomizer can be completely recirculated or re-utilized by either the Venturi tube design (see Appendix A) or simply the hand-pump pressurization system for aerosol applications. This new-concept impaction atomizer could be a very good atomization system for aerosol applications with quality spray performances having no negative environmental impact. It has potential reduction of production costs and promising marketing value.

7.2 Recommendations

Based on the observations and conclusions drawn in the previous section, there are several avenues that should be investigated to further understand the influence of external excitations on the liquid spray produced by pressure-swirl atomizers.

The high velocity of the wave motion and the short length of the liquid sheet bring with difficulties in observing the instability development of the disturbances by visualization techniques. Therefore, high speed visualization techniques are highly recommended in order to study the mechanism of the liquid breakup processes.

The new-concept impaction atomizer produces very fine and uniform spray. It is very promising for aerosol applications. The dripping fluid can be recirculated or re-utilized completely by Venturi effect, but further experimental verifications are still needed. The hand-pump pressurization system is also recommended to be tested

for recirculation or re-utilization of the dripping fluid created by the new-concept impaction atomizer.

References

[1] A. H. Lefebvre. *Atomization and Sprays.* Hemisphere, New York, 1989.

[2] H. B. Squire. Investigation of the instability of a moving liquid film. *British Journal of Applied Phisics*, 4:167–169, 1953.

[3] X. Li and R. S. Tankin. On the temporal instability of a two-dimensional viscous liquid sheet. *Journal of Fluid Mechanics*, 226:425–443, 1991.

[4] S. A. Jazayeri and X. Li. Nonlinear breakup of liquid sheets. *ILASS -AMERICAS 96, 9th Annual Conference on Liquid Atomization Systems*, pages 114–119, May 1996.

[5] Xianguo Li. Spatial instability of plane liquid sheets. *Chemical Engineering Sciences*, 48:2973–2981, 1993.

[6] N. Dombrowski and W. R. Johns. The aerodynamic instability and disintegration of viscous liquid sheets. *Chemical Engineering Sciences*, 18:203–214, 1963.

[7] L. Rayleigh. On the instability of jets. *Proceedings of London Mathematical Society*, 10:4–13, 1878.

[8] R. N. Berglund and B. Y. H. Liu. Generation of monodisperse aerosol standards. *Environmental Sciences and Technology*, 7(2):147–153, 1973.

[9] W. D. Warnica, M. Van Reenen, M. Renksizbulut and A. B. Strong. Charge synchronization for a piezoelectric drolet generator. *Review of Scientific Instruments*, 64(8):1–6, 1993.

[10] J. C. O'C. Young and R. J. Lang. An ultrasonic oil burner. *2nd American Petroleum Institute Research Conference onDistillate Fuel Combustion, API Publication1701, Paper CP62-7*, 1962.

[11] D. W. Locklin. *recent research and development in residential oil burners. Combustion Technology: Some Modern developments.* Academic, New York, Chap. 15, 1974.

[12] F. Takahashi, W. J. Schmoll and J. L. Dressler. Characteristics of a velocity-modulated pressure-swirl atomizing spray. *Journal of Propulsion and Power*, 11(5):955–963, 1995.

[13] J. L. Dressler and W. Anderson. Control of impinging jet atomization by velocity-modulation. *ILASS - AMERICAS 96, 9th Annual Conference on Liquid Atomization and Spray Systems*, pages 12–16, May 1996.

[14] D. F. Rutland and G. J. Jameson. A non-linear effect in the capillary instability of liquid jets. *Journal of Fluid Mechanics*, 46(2):267–271, 1971.

[15] S. J. Leib and M. E. Goldstein. The generation of capillary instabilities on a liquid jet. *Journal of Fluid Mechanics*, 168:479–500, 1986.

[16] S. J. Leib and M. E. Goldstein. Convective and absolute instability of a viscous liquid jet. *Physics of Fluids*, 29:952–954, 1986.

[17] J. B. Keller and S. I. Rubinow. Spatial instability of a jet. *Physics of Fluids*, 16:2052–2055, 1972.

[18] David Anthony Billenness. The design of a flow channel with an investigation of laminar flow over a square rib. Master's thesis, University of Victoria, 1995.

[19] J. G. Berbee. Aspect ratio and reynolds number effects on the flow behind a rearward-facing step. Master's thesis, University of Wisconsin, Madison, 1987.

[20] F. Duest and J. H. Whitelaw. *Principles and Practice of Laser-Doppler Anrmetry.* Academic Press, London, 1976.

[21] Dantec Elektronik. *User's manual, Particle Dynamic Analyzer*, 1.

[22] W. D. Bachalo and M. J. Houser. Phase/doppler spray analyzer for simultaneous measurements of drop size and velocity distributions. *Optical Engineering*, 23(5):583–590, September/October 1984.

[23] Chien-Pei Mao. Measurements of sprays using phase doppler instruments: A study to establish formal operating procedures. *ILASS-AMERICAS 96-Proceedings of 9th Annual Conference on Liquid Atomization and Spray System*, pages 22–26, 1996.

[24] S. V. Sankar and W. D. Bachalo. Improving phase doppler measurement accuracy using signal amplitude as a validation criterion. *ILASS-AMERICAS 96-Proceedings of 9th Annual Conference on Liquid Atomization and Spray Systems*, pages 27–32, 1996.

[25] S. A. Jazayeri. *Nonlinear Analysis of Liquid Sheet Disintegration.* PhD thesis, University of Victoria, 1997.

[26] M. J. McCarthy and N. A. Molloy. Review of stability of liquid jets and the influence of nozzle design. *Chem. Eng. J.*, 7:1–20, 1974.

[27] Xianguo Li. Mechanism of atomization of a liquid jet. *Atomization and Sprays*, 5(1):89–105, Jan.-Feb. 1995.

[28] Lee G. Dodge and Deborah J. Rhodes. Comparison of drop-size measurement techniques in fuel sprays: Malvern laser-diffraction and aerometrics phase/doppler. *Propared for the Spring, 1986 Meeting of the Central States Section/The Combustion Institute, NASA Lewis Research Center*, May 1986.

[29] Jacob Friedman. The interaction of an annular air jet with a non-evaporating liquid spray. Master's thesis, University of Waterloo, 1994.

[30] W. D. Bachalo and S. V. Sanker. Time-resolved measurements of spray drop size and velocity. liquid particle size measurement techniques. volume 2, pages 209–224. American Society for Testingand Materials, STP 1083, 1990.

[31] Sir Geoffrey Taylor. Formation of thin flat sheets of water. *Proceedings of Royal Society of London*, 259(A):1–17, 1960.

[32] J. H. Mitchell. *Phil. Trans. A.*, pages 181–389, 1890.

Appendix A

Venturi Calculations

A.1 Introduction

This calculation is intended to confirm the possibility of solving the problem of the dripping water for the new-concept impaction atomizer by using the Venturi effect. The geometric design is shown in Figure A.1. The calculation is carried out based on the Bernoulli equation between points C and D; conservation of mass between points B and C; finally, applying viscous pipe flow between points A and C to solve the amount of liquid which can possibly be recirculated by Venturi effect.

A.2 Calculations

According to Bernoulli equation, between C and D, we have

$$\frac{p_D}{\rho} + \frac{1}{2}u_D^2 = \frac{p_C}{\rho} + \frac{1}{2}u_C^2 + gH_v \tag{A.1}$$

where u_D the velocity at point D and it can be considered zero at this point; p_C and P_D are the pressures at point C and D respectively; ρ the liquid density; g the

gravitational acceleration and H_v the height between points C and D. Thus

$$p_C = p_D - \left(\frac{1}{2}\rho u_C^2 + \rho g H_v\right) \tag{A.2}$$

Apply conservation of mass to points B and C, we have

$$\frac{\pi}{4} d_f^2 u_B = \frac{\pi}{4} d_C^2 u_C \tag{A.3}$$

or

$$u_C = \left(\frac{d_f}{d_C}\right)^2 u_B \tag{A.4}$$

Substitute Eq. A.4 into Eq. A.2, we have

$$p_C = p_D - \left[\frac{1}{2}\rho \left(\frac{d_f}{d_C}\right)^4 u_B^2 + \rho g H_v\right] \tag{A.5}$$

But $p_a - p_C \geq 0$, where p_a is the atmospheric pressure at point A. Hence

$$d_C \leq \frac{u_B^{1/2}}{\left(\frac{2(p_D - p_a)}{\rho} - 2gH_v\right)^{1/4}} d_f \tag{A.6}$$

From the PDPA measurement, $u_B \approx 30$ m/s, $p_D - p_a$ is the gauge pressure at point D (which is 60 psi in this experiment), assume $H_v = 5$ mm, then we can calculate the maximum diameter at point C which can cause Venturi effect.

$$d_C \leq \frac{30^{1/2}}{\left(\frac{2\times 60\times 6894.8}{10^3} - 2 \times 10 \times 0.005\right)^{1/4}} d_f = 1.02 d_f \tag{A.7}$$

From the calculation here, the gravitational effect can be neglected.

Now let's assume $d_C = d_f = 0.25$ mm, apply the Hagen-Poiseuille equation (viscous flow in ducts) neglecting the gravitational effect,

$$Q_r = \frac{\pi d_a^4}{64\mu}\left(\frac{p_a - p_C}{d_o - d_C}\right) \approx 1782692 \times \frac{d_a^4}{d_o} \tag{A.8}$$

where d_o is the outer diameter of the injector ($d_o = 6.5$ mm); Q_r the flow rate of the recirculation and d_a the diameter of the side hole.

Now suppose that the amount of dripping fluid can be totally recirculated, that is, $Q_r \approx 0.7Q = 0.7 \times \frac{\pi}{4} d_f^2 u_B$, thus the diameter of the side hole can be calculated from

$$1782692 \times \frac{d_a^4}{d_o} \approx 0.7 \times \frac{\pi}{4} d_f^2 u_B \tag{A.9}$$

or

$$d_a^4 = \frac{0.7\pi d_o d_f^2 u_B}{4 \times 1782692} = \frac{0.7\pi \times 6.5 \times 10^{-3} \times (0.25 \times 10^{-3})^2 \times 30}{4 \times 1782692} \tag{A.10}$$

or

$$d_a = 2.48 \times 10^{-4} \tag{A.11}$$

That means a side hole of 0.248 mm in diameter can be used to recirculate the dripping liquid completely.

A.3 Summary

From the calculations above, it is possible to recirculate the dripping liquid completely by the Venturi effect, theoretically. But further practical verifications are needed.

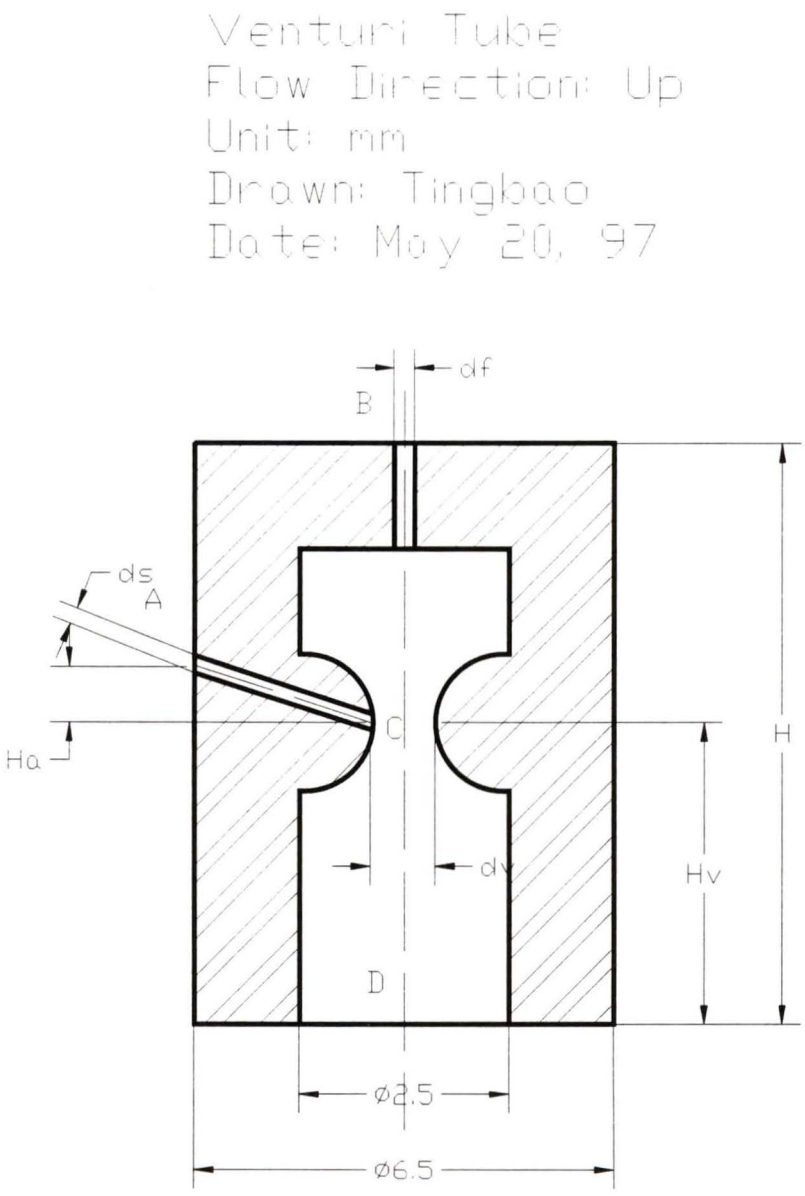

Figure A.1: Schematic of the Venturi pipe

Appendix B

Instability Analysis

Linear analysis shows that the growing amplitude of the disturbances is a function of the initial amplitude and the wave growth rate. For specific flow conditions, for example, the Weber number (W_e) and the Reynolds number (R_e) (or Ohnesorge number Z) given, the wave growth rate can be represented by the curves shown in Figures B.1$\sim$B.3. The disturbance amplitude corresponding to the dominant wavenumber can be expressed as

$$A_1 = \eta_1 \exp(\beta \Omega t) \tag{B.1}$$

While the disturbance amplitude at larger wavenumber (or smaller wave length corresponding to smaller droplets) can be expressed as

$$A_2 = \eta_2 \exp(\beta \omega t) \tag{B.2}$$

where A represents the amplitude of the disturbances, η the initial amplitude, ω the dimensionless wave growth rate, κ the dimensionless wave number, and t is time. The

dimensional factor is defined as

$$\beta = \left(\frac{\rho_\ell r^3}{\sigma}\right)^{1/2} \tag{B.3}$$

Hence, the ratio of Eqs. (B.2) and (B.1) is given below:

$$\frac{A_2}{A_1} = \frac{\eta_2}{\eta_1} \frac{1}{\exp[\beta(\Omega - \omega)t]} \tag{B.4}$$

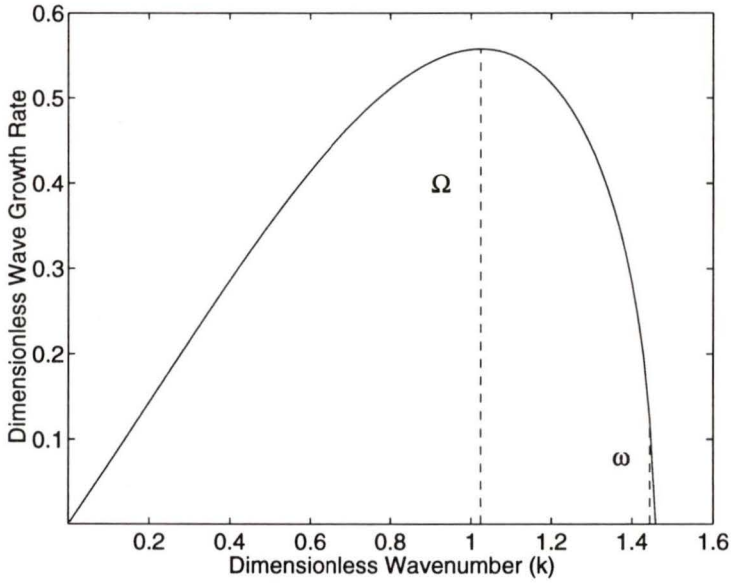

Figure B.1: Temporal wave growth rate as a function of wavenumber for varicose mode. $n = 0$, $W_e = 1000$, $Z = 0.001$, $\rho_g/\rho_\ell = 0.001$, $u_g/u_\ell = 0$.

It is clearly seen from Eq. (B.4), in order to make the amplitude of the exerted external acoustic disturbances larger than that of the disturbances corresponding to the dominant wave growth rate, the initial amplitude of the exerted disturbances must be very large ($\eta_2 \geq \eta_1 \exp[\beta(\Omega - \omega)t]$), because it is proportional to the exponential of a large value $(\Omega - \omega)$.

Assume $r = 0.1$ mm, $u_\ell = 30$ m/s, then for water and air, $\beta = 1.3755$. For the case shown in Figure B.1, $\Omega = 0.5578$, $\omega = 0.1229$. Thus,

$$\eta_2 \geq \eta_1 \exp[\beta(\Omega - \omega)t] > 1.82\eta_1 \tag{B.5}$$

In Figure B.2, $\Omega = 3.5077$, $\omega = 0.8712$, then

$$\eta_2 \geq \eta_1 \exp[\beta(\Omega - \omega)t] > 37.58\eta_1 \tag{B.6}$$

In Figure B.3, $\Omega = 10.6343$, $\omega = 2.2435$, then

$$\eta_2 \geq \eta_1 \exp[\beta(\Omega - \omega)t] > 10^5\eta_1 \tag{B.7}$$

Clearly, it is experimentally difficult to produce such large initial amplitude of disturbances using normal loud speakers (The loud speaker is easily burnt out), as observed in the experiment. With large Weber numbers, which is the common case in laboratory, it is almost impossible to carry it out. Therefore, it is difficult to achieve a significant reduction of the droplet sizes by exerted acoustic excitations, as shown in the PDPA measurements, because the formation process of the droplets is mainly controlled by the disturbances with the dominant wave growth rate.

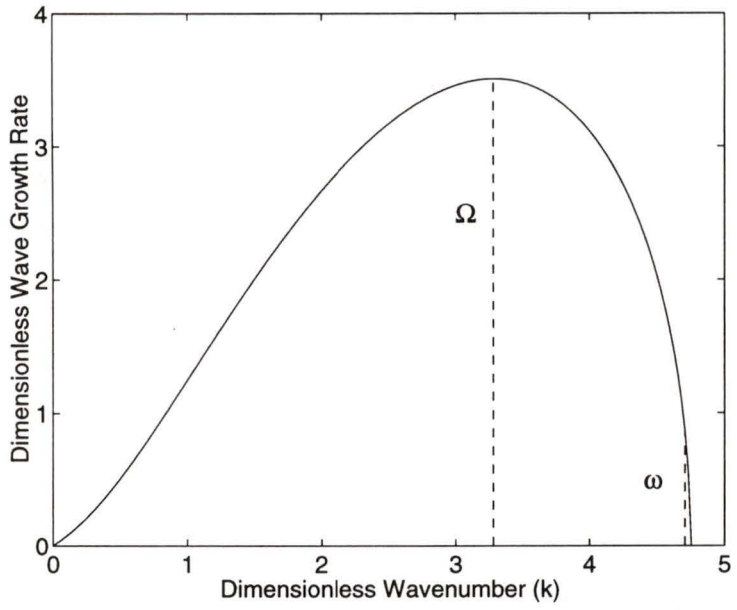

Figure B.2: Temporal wave growth rate as a function of wavenumber for varicose mode. $n = 0$, $W_e = 5000$, $Z = 0.001$, $\rho_g/\rho_\ell = 0.001$, $u_g/u_\ell = 0$.

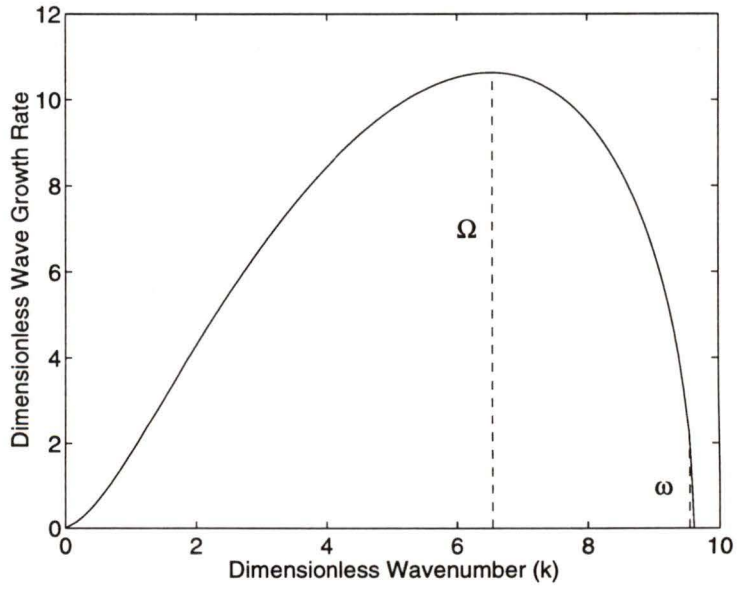

Figure B.3: Temporal wave growth rate as a function of wavenumber for varicose mode. $n = 0$, $W_e = 10^4$, $Z = 0.001$, $\rho_g/\rho_\ell = 0.001$, $u_g/u_\ell = 0$.

Appendix C

Measured Data for Chapter 3

Test Nozzle: Modified Pressure-swirl Atomizer with Insert #3					
Sample Size	Run 1	Run 2	Run 3	Run 4	Run 5
1000	51.18	47.93	48.35	47.86	49.45
2000	48.48	48.52	49.30	49.44	49.47
4000	48.65	48.97	48.27	47.68	49.25
6000	49.64	49.16	49.30	49.77	48.59
8000	49.95	49.49	49.27	48.44	48.89
10000	48.94	49.40	48.92	48.16	48.01
14000	47.95	48.91	48.76	48.78	48.28
18000	48.93	48.16	48.81	48.37	48.66
22000	48.63	48.90	49.18	48.65	49.04
26000	48.47	48.76	49.17	48.90	49.47
30000	48.68	48.86	48.55	48.78	48.73
35000	48.77	48.98	49.13	49.22	48.88
40000	48.93	49.21	48.62	49.20	48.99
45000	49.06	49.00	48.91	48.81	48.88
50000	48.99	48.67	49.00	48.77	48.79

Table C.1: Measured data for sample size validation (Figure 3.3).

Class	Size Range (μm)	Counts	Concentration (counts/cc)	Flux (cc/s/cm^2)	Uvel (m/s)
0	0.00 - 1.73	53	7.57e-001	1.86e-009	9.160
1	1.73 - 3.45	73	9.72e-001	1.97e-008	9.429
2	3.45 - 5.18	73	9.23e-001	6.23e-008	9.290
3	5.18 - 6.90	89	1.19e+000	1.89e-007	9.199
4	6.90 - 8.63	105	1.33e+000	4.09e-007	9.121
5	8.63 - 10.35	125	1.66e+000	8.80e-007	9.140
6	10.35 - 12.08	126	1.77e+000	1.49e-006	9.137
7	12.08 - 13.80	130	1.73e+000	2.15e-006	9.036
8	13.80 - 15.53	100	1.38e+000	2.43e-006	9.022
9	15.53 - 17.25	80	1.08e+000	2.64e-006	9.129
10	17.25 - 18.98	75	1.01e+000	3.21e-006	8.895
11	18.98 - 20.70	56	7.76e-001	3.30e-006	9.164
12	20.70 - 22.43	60	9.55e-001	5.07e-006	8.993
13	22.43 - 24.15	44	6.66e-001	4.45e-006	9.057
14	24.15 - 25.88	39	5.26e-001	4.43e-006	9.292
15	25.88 - 27.60	27	3.33e-001	3.35e-006	9.146
16	27.60 - 29.33	23	5.05e-001	5.90e-006	8.841
17	29.33 - 31.05	19	3.54e-001	5.07e-006	9.139
18	31.05 - 32.78	23	4.64e-001	7.65e-006	8.940
19	32.78 - 34.50	11	2.67e-001	5.36e-006	9.334
20	34.50 - 36.23	8	1.54e-001	3.45e-006	9.019
21	36.23 - 37.95	16	4.64e-001	1.19e-005	8.987
22	37.95 - 39.68	10	1.67e-001	5.09e-006	9.326
23	39.68 - 41.41	6	1.24e-001	4.33e-006	9.378
24	41.41 - 43.13	14	3.98e-001	1.51e-005	9.028
25	43.13 - 44.86	10	3.93e-001	1.73e-005	9.293
26	44.86 - 46.58	10	2.70e-001	1.32e-005	9.255
27	46.58 - 48.31	16	3.70e-001	1.94e-005	8.889
28	48.31 - 50.03	21	6.83e-001	4.04e-005	9.024
29	50.03 - 51.76	19	4.38e-001	2.95e-005	9.280
30	51.76 - 53.48	25	7.71e-001	5.74e-005	9.297
31	53.48 - 55.21	28	9.15e-001	7.35e-005	9.115
32	55.21 - 56.93	27	8.91e-001	7.08e-005	8.230
33	56.93 - 58.66	32	9.66e-001	9.35e-005	9.162

Table C.2: Measured data for the diameter distributions of the SDG (Figure 3.10).

...continued from the previous table

Class	Size Range	Counts	Concentration	Flux	Uvel
	(μm)		(counts/cc)	(cc/s/cm^2)	(m/s)
34	58.66 - 60.38	37	1.08e+000	1.12e-004	8.959
35	60.38 - 62.11	52	1.56e+000	1.77e-004	9.044
36	62.11 - 63.83	46	1.36e+000	1.67e-004	9.014
37	63.83 - 65.56	46	1.36e+000	1.85e-004	9.231
38	65.56 - 67.28	65	1.85e+000	2.68e-004	9.108
39	67.28 - 69.01	77	2.09e+000	3.25e-004	9.042
40	69.01 - 70.73	84	2.50e+000	4.27e-004	9.228
41	70.73 - 72.46	90	2.62e+000	4.75e-004	9.101
42	72.46 - 74.18	164	4.67e+000	9.04e-004	9.052
43	74.18 - 75.91	119	3.46e+000	7.25e-004	9.140
44	75.91 - 77.63	134	4.01e+000	9.00e-004	9.158
45	77.63 - 79.36	148	4.12e+000	9.85e-004	9.129
46	79.36 - 81.09	169	5.25e+000	1.34e-003	9.125
47	81.09 - 82.81	194	5.61e+000	1.53e-003	9.158
48	82.81 - 84.54	214	6.30e+000	1.82e-003	9.153
49	84.54 - 86.26	292	8.60e+000	2.64e-003	9.146
50	86.26 - 87.99	299	8.67e+000	2.84e-003	9.167
51	87.99 - 89.71	309	8.69e+000	3.03e-003	9.208
52	89.71 - 91.44	374	1.10e+001	4.03e-003	9.133
53	91.44 - 93.16	403	1.16e+001	4.50e-003	9.178
54	93.16 - 94.89	432	1.21e+001	4.97e-003	9.157
55	94.89 - 96.61	439	1.25e+001	5.40e-003	9.169
56	96.61 - 98.34	478	1.47e+001	6.72e-003	9.149
57	98.34 - 100.06	624	1.85e+001	8.92e-003	9.168
58	100.06 - 101.79	364	1.07e+001	5.41e-003	9.157
59	101.79 - 103.51	301	8.71e+000	4.65e-003	9.188
60	103.51 - 105.24	237	6.73e+000	3.77e-003	9.181
61	105.24 - 106.96	228	6.52e+000	3.82e-003	9.133
62	106.96 - 108.69	193	5.34e+000	3.28e-003	9.141
63	108.69 - 110.41	138	3.74e+000	2.42e-003	9.180
64	110.41 - 112.14	181	4.80e+000	3.25e-003	9.176
65	112.14 - 113.86	129	3.48e+000	2.47e-003	9.206
66	113.86 - 115.59	132	3.45e+000	2.56e-003	9.168

Table C.3: Measured data for the diameter distributions of the SDG (Figure 3.10).

...continued from the previous table

Class	Size Range (μm)	Counts	Concentration (counts/cc)	Flux (cc/s/cm^2)	Uvel (m/s)
67	115.59 - 117.31	136	3.32e+000	2.57e-003	9.163
68	117.31 - 119.04	137	3.64e+000	2.95e-003	9.167
69	119.04 - 120.77	158	4.17e+000	3.53e-003	9.162
70	120.77 - 122.49	190	4.76e+000	4.20e-003	9.183
71	122.49 - 124.22	260	6.51e+000	6.01e-003	9.197
72	124.22 - 125.94	129	2.89e+000	2.79e-003	9.227
73	125.94 - 127.67	102	2.67e+000	2.66e-003	9.164
74	127.67 - 129.39	76	1.79e+000	1.86e-003	9.177
75	129.39 - 131.12	51	1.18e+000	1.28e-003	9.230
76	131.12 - 132.84	60	1.36e+000	1.56e-003	9.323
77	132.84 - 134.57	50	1.02e+000	1.21e-003	9.238
78	134.57 - 136.29	55	1.27e+000	1.55e-003	9.172
79	136.29 - 138.02	49	1.18e+000	1.49e-003	9.216
80	138.02 - 139.74	50	1.04e+000	1.38e-003	9.227
81	139.74 - 141.47	45	1.08e+000	1.48e-003	9.278
82	141.47 - 143.19	119	3.01e+000	4.19e-003	9.059
83	143.19 - 144.92	656	1.85e+001	2.66e-002	9.033
84	144.92 - 146.64	2260	6.07e+001	9.03e-002	9.011
85	146.64 - 148.37	6555	1.70e+002	2.62e-001	8.996
86	148.37 - 150.09	5124	1.31e+002	2.08e-001	8.980
87	150.09 - 151.82	2940	7.40e+001	1.22e-001	8.974
88	151.82 - 153.54	1249	3.06e+001	5.20e-002	8.980
89	153.54 - 155.27	401	9.86e+000	1.73e-002	8.977
90	155.27 - 157.00	165	4.16e+000	7.55e-003	8.963
91	157.00 - 158.72	64	1.46e+000	2.77e-003	9.082
92	158.72 - 160.45	43	1.07e+000	2.15e-003	9.244
93	160.45 - 162.17	15	3.82e-001	7.87e-004	9.227
94	162.17 - 163.90	18	5.17e-001	1.10e-003	9.194
95	163.90 - 165.62	21	5.33e-001	1.16e-003	9.181
96	165.62 - 167.35	11	4.77e-001	1.07e-003	9.186
97	167.35 - 169.07	12	2.64e-001	6.19e-004	9.252
98	169.07 - 170.80	16	4.43e-001	1.06e-003	9.214
99	170.80 - 172.52	10	2.84e-001	7.07e-004	9.268

Table C.4: Measured data for the diameter distributions of the SDG (Figure 3.10).

Class	Size Range	Counts	Concentration	Flux	Uvel
	(μm)		(counts/cc)	(cc/s/cm^2)	(m/s)
0	0 - 1.73	1	3.22E+01	6.08E+10	7.017
1	1.73 - 3.45	0	0.00E+00	0.00E+00	0
2	3.45 - 5.18	0	0.00E+00	0.00E+00	0
3	5.18 - 6.9	2	6.11E+01	6.98E+08	6.642
4	6.9 - 8.63	2	3.64E+01	8.32E+08	6.798
5	8.63 - 10.35	1	3.46E+01	1.67E+07	8.299
6	10.35 - 12.08	5	2.05E+00	1.22E+06	6.439
7	12.08 - 13.8	6	1.83E+00	1.79E+06	7.121
8	13.8 - 15.53	0	0.00E+00	0.00E+00	0
9	15.53 - 17.25	4	1.35E+00	2.45E+06	6.734
10	17.25 - 18.98	0	0.00E+00	0.00E+00	0
11	18.98 - 20.7	0	0.00E+00	0.00E+00	0
12	20.7 - 22.43	1	3.53E+01	1.40E+06	6.706
13	22.43 - 24.15	0	0.00E+00	0.00E+00	0
14	24.15 - 25.88	1	2.90E+01	1.95E+06	7.392
15	25.88 - 27.6	1	4.13E+01	2.82E+06	6.203
16	27.6 - 29.33	1	1.40E+00	1.08E+05	5.828
17	29.33 - 31.05	0	0.00E+00	0.00E+00	0
18	31.05 - 32.78	0	0.00E+00	0.00E+00	0
19	32.78 - 34.5	1	2.47E+01	4.26E+06	8.015
20	34.5 - 36.23	0	0.00E+00	0.00E+00	0
21	36.23 - 37.95	0	0.00E+00	0.00E+00	0
22	37.95 - 39.68	0	0.00E+00	0.00E+00	0
23	39.68 - 41.41	0	0.00E+00	0.00E+00	0
24	41.41 - 43.13	0	0.00E+00	0.00E+00	0
25	43.13 - 44.86	0	0.00E+00	0.00E+00	0
26	44.86 - 46.58	0	0.00E+00	0.00E+00	0
27	46.58 - 48.31	0	0.00E+00	0.00E+00	0
28	48.31 - 50.03	0	0.00E+00	0.00E+00	0
29	50.03 - 51.76	0	0.00E+00	0.00E+00	0
30	51.76 - 53.48	0	0.00E+00	0.00E+00	0
31	53.48 - 55.21	0	0.00E+00	0.00E+00	0
32	55.21 - 56.93	1	1.67E+01	1.03E+05	6.386
33	56.93 - 58.66	0	0.00E+00	0.00E+00	0

Table C.5: Measured data for the diameter distributions of the SDG (Figure 3.11).

...continued from the previous table

Class	Size Range (μm)	Counts	Concentration (counts/cc)	Flux (cc/s/cm^2)	Uvel (m/s)
34	58.66 - 60.38	0	0.00E+00	0.00E+00	0
35	60.38 - 62.11	0	0.00E+00	0.00E+00	0
36	62.11 - 63.83	1	1.52E+01	1.22E+05	5.892
37	63.83 - 65.56	0	0.00E+00	0.00E+00	0
38	65.56 - 67.28	3	4.60E+01	4.67E+05	6.367
39	67.28 - 69.01	1	1.47E+01	1.44E+05	5.699
40	69.01 - 70.73	0	0.00E+00	0.00E+00	0
41	70.73 - 72.46	0	0.00E+00	0.00E+00	0
42	72.46 - 74.18	2	2.43E+01	3.25E+05	6.267
43	74.18 - 75.91	0	0.00E+00	0.00E+00	0
44	75.91 - 77.63	0	0.00E+00	0.00E+00	0
45	77.63 - 79.36	1	1.68E+01	2.62E+05	5.946
46	79.36 - 81.09	2	3.42E+01	5.68E+05	5.951
47	81.09 - 82.81	1	1.38E+01	2.54E+05	6.203
48	82.81 - 84.54	0	0.00E+00	0.00E+00	0
49	84.54 - 86.26	0	0.00E+00	0.00E+00	0
50	86.26 - 87.99	0	0.00E+00	0.00E+00	0
51	87.99 - 89.71	0	0.00E+00	0.00E+00	0
52	89.71 - 91.44	0	0.00E+00	0.00E+00	0
53	91.44 - 93.16	0	0.00E+00	0.00E+00	0
54	93.16 - 94.89	0	0.00E+00	0.00E+00	0
55	94.89 - 96.61	0	0.00E+00	0.00E+00	0
56	96.61 - 98.34	1	2.65E+01	8.84E+05	6.706
57	98.34 - 100.06	0	0.00E+00	0.00E+00	0
58	100.06 - 101.79	1	2.60E+01	9.71E+05	6.77
59	101.79 - 103.51	0	0.00E+00	0.00E+00	0
60	103.51 - 105.24	0	0.00E+00	0.00E+00	0
61	105.24 - 106.96	0	0.00E+00	0.00E+00	0
62	106.96 - 108.69	0	0.00E+00	0.00E+00	0
63	108.69 - 110.41	1	5.20E+01	2.48E+04	6.77
64	110.41 - 112.14	2	1.36E+00	6.68E+04	6.674
65	112.14 - 113.86	2	9.27E+01	4.89E+04	6.83
66	113.86 - 115.59	2	1.32E+00	7.18E+04	6.734

Table C.6: Measured data for the diameter distributions of the SDG (Figure 3.11).

...continued from the previous table

Class	Size Range	Counts	Concentration	Flux	Uvel
	(μm)		(counts/cc)	(cc/s/cm^2)	(m/s)
67	115.59 - 117.31	0	0.00E+00	0.00E+00	0
68	117.31 - 119.04	1	5.02E+01	3.05E+04	6.889
69	119.04 - 120.77	1	5.50E+01	3.34E+04	6.578
70	120.77 - 122.49	0	0.00E+00	0.00E+00	0
71	122.49 - 124.22	1	4.75E+01	3.37E+04	7.081
72	124.22 - 125.94	0	0.00E+00	0.00E+00	0
73	125.94 - 127.67	2	8.20E+01	6.01E+04	6.734
74	127.67 - 129.39	0	0.00E+00	0.00E+00	0
75	129.39 - 131.12	1	5.40E+01	4.23E+04	6.642
76	131.12 - 132.84	0	0.00E+00	0.00E+00	0
77	132.84 - 134.57	2	2.44E+01	2.11E+04	6.77
78	134.57 - 136.29	20	2.32E+00	2.06E+03	6.71
79	136.29 - 138.02	74	8.95E+00	8.28E+03	6.717
80	138.02 - 139.74	204	2.40E+01	2.29E+02	6.684
81	139.74 - 141.47	515	6.32E+01	6.25E+02	6.674
82	141.47 - 143.19	1032	1.27E+02	1.30E+01	6.668
83	143.19 - 144.92	1433	1.77E+02	1.88E+01	6.653
84	144.92 - 146.64	1160	1.42E+02	1.55E+01	6.633
85	146.64 - 148.37	855	1.04E+02	1.18E+01	6.638
86	148.37 - 150.09	305	3.65E+01	4.29E+02	6.631
87	150.09 - 151.82	125	1.46E+01	1.77E+02	6.642
88	151.82 - 153.54	45	5.27E+00	6.64E+03	6.65
89	153.54 - 155.27	25	2.72E+00	3.54E+03	6.634
90	155.27 - 157	11	1.23E+00	1.65E+03	6.648
91	157 - 158.72	2	1.73E+01	2.36E+04	6.546
92	158.72 - 160.45	2	2.81E+01	3.95E+04	6.514
93	160.45 - 162.17	4	4.94E+01	7.32E+04	6.64
94	162.17 - 163.9	1	1.10E+01	1.67E+04	6.578
95	163.9 - 165.62	1	1.25E+01	1.93E+04	6.514
96	165.62 - 167.35	1	1.19E+01	2.20E+04	7.576
97	167.35 - 169.07	1	1.10E+01	1.83E+04	6.578
98	169.07 - 170.8	4	5.25E+01	8.92E+04	6.516
99	170.8 - 172.52	2	2.58E+01	4.72E+04	6.798

Table C.7: Measured data for the diameter distributions of the SDG (Figure 3.11).

Appendix D

Measured Data for Chapter 4

Cone angle (deg.)	70	70	75	74	72	62
Frequency (kHz)	0	0.5	0.75	1.75	5.5	16.5

Table D.1: Measured data for the acoustic effect on the spray angle (Figure 4.10).

x mm (inch)	u m/s	Flux cc/s/cm^2	D_{32} μm	D_{30} μm
-20.32 (-0.8)	5.236	0.0192722	70.12	67.09
-17.78 (-0.7)	5.525	0.0423411	68.98	65.63
-15.24 (-0.6)	5.54	0.0568767	66.79	62.85
-12.7 (-0.5)	5.096	0.0676237	63.76	58.83
-11.43 (-0.45)	4.849	0.0685345	61.77	56.43
-10.16 (-0.4)	4.556	0.0675141	60.04	54.0
7 -8.89 (-0.35)	4.317	0.063034	58.18	51.34
-7.62 (-0.3)	4.082	0.0576096	56.25	48.13
-5.08 (-0.2)	3.715	0.0502276	51.81	42.59
-2.54 (-0.1)	3.926	0.0393264	49.14	38.66
0 (0)	4.729	0.0347536	48.98	35.52
1.27 (0.05)	5.608	0.0308138	50.05	35.14
2.54 (0.1)	6.438	0.0285497	51.69	35.79
3.81 (0.15)	6.802	0.0285501	52.08	35.99
5.08 (0.2)	6.802	0.0310219	52.7	37.31
7.62 (0.3)	6.191	0.0445186	56.07	43.4
10.16 (0.4)	6.227	0.0773263	61.34	53.45
11.43 (0.45)	6.441	0.0922336	63.76	57.27
12.7 (0.5)	6.607	0.104153	65.59	60.14
13.97 (0.55)	6.475	0.083738	66.09	61.26
15.24 (0.6)	6.347	0.0705201	66.75	62.43
17.78 (0.7)	5.471	0.03332	64.69	61.25
20.32 (0.8)	4.621	0.0128837	62.78	60.03

Table D.2: Measured data for the baseline pressure-swirl nozzle (Figures 4.11 $\sim$ 4.13).

x mm (inch)	D_{30} μm	y mm (inch)	D_{30} μm
-20.32 (-0.8)	50.087	-40.64 (-1.6)	62.91
-17.78 (-0.7)	50.694	-38.1 (-1.5)	59.43
-15.24 (-0.6)	50.217	-35.56 (-1.4)	56.85
-12.7 (-0.5)	49.86	-33.02 (-1.3)	55.08
-10.16 (-0.4)	49.265	-30.48 (-1.2)	53.02
-7.62 (-0.3)	49.749	-27.94 (-1.1)	52.27
-5.08 (-0.2)	50.283	-25.4 (-1.0)	51.22
-2.54 (-0.1)	50.364	-22.86 (-0.9)	50.78
0 (0)	50.329	-20.32 (-0.8)	50.61
2.54 (0.1)	51.161	-17.78 (-0.7)	50.742
5.08 (0.2)	51.017	-15.24 (-0.6)	50.673
7.62 (0.3)	52.124	-12.7 (-0.5)	50.297
10.16 (0.4)	52.602	-10.16 (-0.4)	51.268
12.7 (0.5)	53.364	-7.62 (-0.3)	50.678
15.24 (0.6)	54.307	-5.08 (-0.2)	50.63
17.78 (0.7)	56.83	-2.54 (-0.1)	51.382
20.32 (0.8)	55.538	0 (0)	51.322
22.86 (0.9)	57.667	2.54 (0.1)	51.923
25.4 (1.0)	61.6	5.08 (0.2)	54.653
		7.62 (0.3)	56.441
		10.16 (0.4)	58.224
		12.7 (0.5)	60.107
		15.24 (0.6)	62.727
		17.78 (0.7)	64.704
		20.32 (0.8)	68.293

Table D.3: Measured data for the baseline pressure-swirl nozzle at 203.2 mm (8 inches) of axial location (Figure 4.14).

Class	Size Range	Counts	Concentration	Flux	Uvel
	(μm)		(counts/cc)	(cc/s/cm^2)	(m/s)
0	0 - 2.17	5	2.09E+00	4.91E-09	4.356
1	2.17 - 4.35	27	5.47E+00	1.29E-07	5.475
2	4.35 - 6.52	204	2.76E+01	2.34E-06	5.844
3	6.52 - 8.7	1444	1.78E+02	3.46E-05	5.641
4	8.7 - 10.87	4394	4.97E+02	1.86E-04	5.574
5	10.87 - 13.04	5865	6.35E+02	4.01E-04	5.435
6	13.04 - 15.22	6894	6.73E+02	6.66E-04	5.36
7	15.22 - 17.39	5801	5.29E+02	7.64E-04	5.24
8	17.39 - 19.57	4628	3.74E+02	7.66E-04	5.23
9	19.57 - 21.74	3458	2.40E+02	6.78E-04	5.253
10	21.74 - 23.92	2227	1.31E+02	5.06E-04	5.388
11	23.92 - 26.09	1552	7.93E+01	4.12E-04	5.578
12	26.09 - 28.26	1315	6.02E+01	4.10E-04	5.766
13	28.26 - 30.44	1201	4.90E+01	4.46E-04	6.167
14	30.44 - 32.61	923	3.55E+01	4.17E-04	6.467
15	32.61 - 34.79	849	2.83E+01	4.40E-04	7.053
16	34.79 - 36.96	742	2.32E+01	4.52E-04	7.387
17	36.96 - 39.13	685	1.95E+01	4.79E-04	7.818
18	39.13 - 41.31	628	1.70E+01	5.13E-04	8.199
19	41.31 - 43.48	480	1.26E+01	4.69E-04	8.614
20	43.48 - 45.66	445	1.07E+01	4.86E-04	9.095
21	45.66 - 47.83	430	1.01E+01	5.45E-04	9.409
22	47.83 - 50.01	467	1.02E+01	6.50E-04	9.729
23	50.01 - 52.18	406	8.49E+00	6.27E-04	9.922
24	52.18 - 54.35	434	9.04E+00	7.88E-04	10.372
25	54.35 - 56.53	439	8.68E+00	8.76E-04	10.673

Table D.4: Measured data for the diameter distributions of the baseline pressure-swirl nozzle at the centerline with acoustics. z = 25.4 mm (1 inch).

...continued from the previous table

Class	Size Range	Counts	Concentration	Flux	Uvel
	(μm)		(counts/cc)	(cc/s/cm^2)	(m/s)
26	56.53 - 58.7	422	8.58E+00	9.72E-04	10.689
27	58.7 - 60.88	448	8.99E+00	1.18E-03	11.066
28	60.88 - 63.05	336	6.45E+00	9.40E-04	11.106
29	63.05 - 65.22	325	5.95E+00	9.91E-04	11.457
30	65.22 - 67.4	300	5.56E+00	1.03E-03	11.523
31	67.4 - 69.57	330	6.07E+00	1.24E-03	11.566
32	69.57 - 71.75	289	5.23E+00	1.20E-03	11.874
33	71.75 - 73.92	278	5.00E+00	1.24E-03	11.707
34	73.92 - 76.09	239	4.13E+00	1.15E-03	12.09
35	76.09 - 78.27	188	3.16E+00	9.60E-04	12.117
36	78.27 - 80.44	188	3.45E+00	1.14E-03	12.141
37	80.44 - 82.62	160	2.74E+00	1.01E-03	12.51
38	82.62 - 84.79	118	1.98E+00	8.09E-04	12.778
39	84.79 - 86.97	98	1.75E+00	7.57E-04	12.542
40	86.97 - 89.14	90	1.55E+00	7.09E-04	12.374
41	89.14 - 91.31	56	9.41E-01	4.83E-04	12.874
42	91.31 - 93.49	47	7.75E-01	4.42E-04	13.326
43	93.49 - 95.66	29	4.73E-01	2.86E-04	13.21
44	95.66 - 97.84	36	6.26E-01	3.91E-04	12.744
45	97.84 - 100.01	26	4.65E-01	3.23E-04	13.252
46	100.01 - 102.18	13	2.70E-01	1.82E-04	12.096
47	102.18 - 104.36	15	2.99E-01	2.11E-04	11.85
48	104.36 - 106.53	12	2.26E-01	1.84E-04	12.84
49	106.53 - 108.71	10	2.01E-01	1.81E-04	13.405

Table D.5: Measured data for the diameter distributions of the baseline pressure-swirl nozzle at the centerline with acoustics. z = 25.4 mm (1 inch). Figure 4.15.

Class	Size Range	Counts	Concentration	Flux	Uvel
	(μm)		(counts/cc)	(cc/s/cm^2)	(m/s)
0	0 - 2.17	0	0.00E+00	0.00E+00	0
1	2.17 - 4.35	1	4.49E-02	1.63E-09	8.467
2	4.35 - 6.52	1	2.53E-02	2.93E-09	7.964
3	6.52 - 8.7	0	0.00E+00	0.00E+00	0
4	8.7 - 10.87	0	0.00E+00	0.00E+00	0
5	10.87 - 13.04	0	0.00E+00	0.00E+00	0
6	13.04 - 15.22	0	0.00E+00	0.00E+00	0
7	15.22 - 17.39	3	9.18E-02	3.78E-08	1.494
8	17.39 - 19.57	7	2.15E-01	1.50E-07	1.779
9	19.57 - 21.74	2	3.48E-02	1.43E-07	7.65
10	21.74 - 23.92	8	1.28E-01	2.36E-07	2.565
11	23.92 - 26.09	7	3.58E-01	7.56E-07	2.271
12	26.09 - 28.26	1	7.63E-01	6.97E-07	0.773
13	28.26 - 30.44	5	4.12E-02	2.91E-07	4.791
14	30.44 - 32.61	21	1.48E+00	3.25E-06	1.208
15	32.61 - 34.79	49	3.80E+00	8.42E-06	1.005
16	34.79 - 36.96	142	1.33E+01	2.91E-05	0.827
17	36.96 - 39.13	237	3.80E+01	9.09E-05	0.762
18	39.13 - 41.31	589	4.74E+01	1.56E-04	0.89
19	41.31 - 43.48	840	5.58E+01	2.56E-04	1.063
20	43.48 - 45.66	1009	5.95E+01	3.52E-04	1.186
21	45.66 - 47.83	1200	4.64E+01	3.91E-04	1.472
22	47.83 - 50.01	1522	5.05E+01	5.47E-04	1.656
23	50.01 - 52.18	1453	3.40E+01	5.22E-04	2.068
24	52.18 - 54.35	1485	2.64E+01	5.68E-04	2.556
25	54.35 - 56.53	1660	2.32E+01	6.59E-04	3.01

Table D.6: Measured data for the diameter distributions of the baseline pressure-swirl nozzle at the edge with acoustics. $z = 25.4$ mm (1 inch). Figure 4.16.

...continued from the previous table

Class	Size Range	Counts	Concentration	Flux	Uvel
	(μm)		(counts/cc)	(cc/s/cm^2)	(m/s)
26	56.53 - 58.7	1666	1.79E+01	6.94E-04	3.661
27	58.7 - 60.88	1918	1.71E+01	8.74E-04	4.32
28	60.88 - 63.05	1659	1.31E+01	8.24E-04	4.786
29	63.05 - 65.22	1668	1.19E+01	9.13E-04	5.295
30	65.22 - 67.4	1552	9.59E+00	9.03E-04	5.871
31	67.4 - 69.57	1721	9.46E+00	1.07E-03	6.426
32	69.57 - 71.75	1580	8.09E+00	1.05E-03	6.695
33	71.75 - 73.92	1645	7.82E+00	1.20E-03	7.271
34	73.92 - 76.09	1462	6.68E+00	1.17E-03	7.601
35	76.09 - 78.27	1310	5.66E+00	1.14E-03	8.012
36	78.27 - 80.44	1178	4.89E+00	1.12E-03	8.398
37	80.44 - 82.62	883	3.62E+00	9.40E-04	8.79
38	82.62 - 84.79	701	2.78E+00	8.07E-04	9.11
39	84.79 - 86.97	597	2.37E+00	7.56E-04	9.259
40	86.97 - 89.14	484	1.91E+00	6.73E-04	9.489
41	89.14 - 91.31	355	1.32E+00	5.07E-04	9.669
42	91.31 - 93.49	269	1.07E+00	4.43E-04	9.683
43	93.49 - 95.66	218	8.34E-01	3.76E-04	9.841
44	95.66 - 97.84	143	5.60E-01	2.66E-04	9.686
45	97.84 - 100.01	123	4.53E-01	2.39E-04	10.088
46	100.01 - 102.18	84	3.11E-01	1.70E-04	9.756
47	102.18 - 104.36	67	2.16E-01	1.32E-04	10.247
48	104.36 - 106.53	45	1.49E-01	9.65E-05	10.224
49	106.53 - 108.71	38	1.16E-01	8.47E-05	10.839

Table D.7: Measured data for the diameter distributions of the baseline pressure-swirl nozzle at the edge with acoustics. $z = 25.4$ mm (1 inch). Figure 4.16.

frequency	D_{30}	Frequency	D_{30}	Frequency	D_{30}	Frequency	D_{30}
0.5	41.92	3.5	41.94	9.5	42.4	15.5	42.3
0.75	41.34	3.75	42.02	10	42.62	16	42
1	40.3	4	42.1	10.5	42.71	16.5	42.2
1.25	37.26	5	42.18	11	42.48	17	42.331
1.5	42.11	5.5	42.71	11.5	42.52	17.5	42.72
1.75	42.49	6	42.57	12	42.69	18	42.61
2	42.56	6.5	42.58	12.5	42.72	18.5	42.51
2.25	42.19	7	42.18	13	42.38	19	42.3
2.5	42.64	7.5	42.39	13.5	42.25	19.5	42.29
2.75	42.19	8	42.42	14	42.28	20	41.99
3	42.46	8.5	42.38	14.5	41.99	20.5	42.31
3.25	42.26	9	42.32	15	42.17		

Table D.8: Measured data for the diameter variations of the baseline pressure-swirl nozzle with acoustic frequency at power level 3. $z = 25.4$ mm (1 inch). Figure 4.18.

Frequency	D_{32}	D_{30}	Frequency	D_{32}	D_{30}
0	58.49231	48.09238	7	59.33076	47.79977
0.5	57.4718	47.00659	7.5	58.16279	46.99389
1	57.74376	47.44315	8	58.36877	47.08751
1.5	57.79666	47.46157	9	58.19768	47.69105
2	58.15444	47.40384	10	59.61329	50.78891
2.5	57.91815	47.30898	11	59.52522	50.62827
3	57.62096	46.40026	12	59.48699	50.19426
3.5	57.40863	46.36713	13	58.87516	49.99394
4	57.47755	46.37151	14	59.13196	50.10171
4.5	57.56834	46.71513	15	59.57648	50.4334
5	57.61968	46.66959	16	60.14706	50.85026
5.5	58.10884	46.83519	17	59.98677	50.6408
6	58.3383	47.3749	18	60.8503	51.2527
6.5	58.58137	47.21957	19	58.79315	49.71711

Table D.9: Line-averaged data for the mean diameters of the baseline pressure-swirl nozzle with acoustic frequency at power level 2. $z = 25.4$ mm (1 inch). Figure 4.19.

Frequency	D_{32}	D_{30}	Frequency	D_{32}	D_{30}
0	57.00565	46.34253	10	57.86539	48.93328
1	60.94204	51.24683	11	59.03898	49.34743
2	59.15488	50.34624	12	59.09007	49.42293
3	58.38261	49.44894	13	59.00359	48.97918
4	59.27872	50.26046	14	62.11337	50.76374
5	59.08325	50.02149	15	61.94416	50.72702
6	61.37461	51.55978	16	58.35368	47.53133
7	57.40492	47.08202	17	58.52831	47.92635
8	58.09045	48.00365	18	58.03086	47.72052
9	58.26217	48.26421	19	58.03151	47.63366

Table D.10: Line-averaged data for the mean diameters of the baseline pressure-swirl nozzle with acoustic frequency at power level 5. $z = 25.4$ mm (1 inch). Figure 4.20.

Frequency	D_{32}	D_{30}	Frequency	D_{32}	D_{30}
0	50.03421	63.39462	10	51.03554	63.77972
1	50.19568	63.51819	11	50.55896	63.08937
2	50.5907	63.96112	12	50.52374	63.11203
3	50.58556	63.88662	13	51.96557	64.54025
4	51.07109	63.58695	14	52.12859	64.63546
5	51.5977	64.09826	15	52.44971	65.01756
6	51.59253	64.15962	16	51.04264	63.60541
7	51.4447	63.87737	17	51.07197	63.71324
8	51.66698	64.4366	18	50.82364	63.2655
9	51.53699	64.45081	19	50.79859	63.05838

Table D.11: Line-averaged data for the mean diameters of the baseline pressure-swirl nozzle with acoustic frequency at power level 1.5. $z = 203.2$ mm (8 inches). Figure 4.21.

Frequency	D_{32}	D_{30}	Frequency	D_{32}	D_{30}
0	53.60987	65.44065	10	53.25498	65.48573
1	53.59999	65.47914	11	53.72527	65.90123
2	53.69658	65.59855	12	53.57146	65.7639
3	54.03322	65.79253	13	53.57567	65.76242
4	54.19636	65.97324	14	53.98541	66.18497
5	54.61245	66.31773	15	54.48353	66.58059
6	55.27149	66.7222	16	55.07406	66.86465
7	55.39713	66.8289	17	53.93216	66.44743
8	53.02754	65.40496	18	54.63457	67.02536
9	53.288	65.52811	19	54.28282	66.06759

Table D.12: Line-averaged data for the mean diameters of the baseline pressure-swirl nozzle with acoustic frequency at power level 3. z = 203.2 mm (8 inches). Figure 4.22.

x	Power 1	Power 2	Power 3	Power 4	Power 5
-10.16	51.59	50.03	50.01	49.96	50.14
-5.08	46.03	45.65	45.01	44.88	44.68
0	44.71	44.13	43.97	43.86	43.89
5.08	47.47	46.97	46.54	46.66	46.42
10.16	55.27	54.82	55.00	54.82	54.89

Table D.13: Measured data for the mass mean diameter of the baseline pressure-swirl nozzle as a function of acoustic power level. z = 25.4 mm (1 inch), f_a = 19 kHz. Figure 4.23.

Power level	0	1	2	3	4	5	6
D_{30}	56.30	56.12	56.84	55.73	55.63	55.15	55.36

Table D.14: Measured data for the mass mean diameter of the baseline pressure-swirl nozzle as a function of acoustic power level. z = 25.4 mm (1 inch), f_a = 10 kHz. Figure 4.24.

Appendix E

Measured Data for Chapter 5

Velocity (m/s)	$D_{30}(\mu m)$	Flux	x (mm)
3.247	48.46	0.12252	-11.43
3.634	48.37	0.122936	-10.16
4.201	48.23	0.118428	-8.89
4.857	47.29	0.101823	-7.62
5.712	47.19	0.0989561	-6.35
7.461	48.92	0.103125	-5.08
10.29	52.37	0.107952	-3.81
12.86	55.40	0.110354	-2.54
14.29	55.54	0.101841	-1.27
14.60	55.16	0.0997203	0
13.6	54.51	0.106448	1.27
11.47	52.24	0.0999606	2.54
8.885	49.98	0.089538	3.81
6.596	47.99	0.0795235	5.08
5.751	49.49	0.0787809	6.35
5.417	51.57	0.0859538	7.62
5.044	52.55	0.097919	8.89
4.766	53.19	0.0792777	10.16
4.781	54.71	0.0648671	11.43
4.564	55.68	0.0480177	12.7

Table E.1: Measured data for the mass mean diameter distributions of the modified pressure-swirl atomizer (Insert # 1) without acoustics. $z = 25.4$ mm (1 inch). Figures 5.17 and 5.18.

Velocity (m/s)	$D_{30}(\mu m)$	x (mm)	Velocity (m/s)	D_{30} (μm)	x (mm)
2.286	55.5	-19.05	15.91	70.75	-1.27
2.509	54.94	-17.78	16.43	70.50	0
2.761	51.44	-16.51	16.16	69.10	1.27
3.004	53.77	-15.24	15.02	67.41	2.54
3.242	53.63	-13.97	12.82	65.09	3.81
3.454	53.99	-12.7	9.964	61.27	5.08
3.749	53.24	-11.43	8.078	58.71	6.35
4.265	53.60	-10.16	7.042	58.93	7.62
4.930	54.73	-8.89	6.655	59.97	8.89
5.774	56.33	-7.62	6.232	60.93	10.16
6.894	57.33	-6.35	5.859	60.87	11.43
9.018	61.26	-5.08	5.494	61.5	12.7
12.09	66.30	-3.81	5.23	62.64	13.97
14.51	69.20	-2.54	5.045	62.96	16.51

Table E.2: Measured data for the mass mean diameter distributions of the modified pressure-swirl atomizer (Insert # 2) without acoustics. $z = 25.4$ mm (1 inch). Figures 5.17 and 5.18.

Velocity (m/s)	$D_{30}(\mu m)$	x (mm)	Velocity (m/s)	D_{30} (μm)	x (mm)
3.722	54.03	-13.97	18.13	72.92	0
4.141	54.03	-12.7	17.85	72.94	1.27
4.634	54.09	-11.43	16.91	72.24	2.54
5.662	56.54	-10.16	15.41	69.84	3.81
6.578	58.08	-8.89	12.49	64.30	5.08
7.398	58.19	-7.62	9.889	60.39	6.35
8.691	60.03	-6.35	8.671	59.67	7.62
11.11	64.21	-5.08	8.006	59.74	8.89
14.04	68.64	-3.81	7.549	60.55	10.16
16.24	71.63	-2.54	7.106	61.00	11.43
17.60	72.64	-1.27	7.133	62.62	12.7

Table E.3: Measured data for the mass mean diameter distributions of the modified pressure-swirl atomizer (Insert # 3) without acoustics. $z = 25.4$ mm (1 inch). Figures 5.17 and 5.18.

Velocity (m/s)	$D_{30}(\mu m)$	x (mm)	Velocity (m/s)	D_{30} (μm)	x (mm)
1.479	83.44	-21.59	4.127	64.58	6.35
1.659	81.54	-19.05	4.003	64.37	8.89
1.978	77.52	-16.51	3.815	65.45	11.43
2.422	75.16	-13.97	3.366	67.53	13.97
2.603	74.36	-11.43	3.009	69.11	16.51
3.034	71.81	-8.89	2.811	69.77	19.05
3.432	68.78	-6.35	2.424	72.14	21.59
3.664	68.53	-3.81	2.026	75.55	24.13
4.079	66.08	-1.27	1.705	78.94	26.67
3.768	67.45	1.27	1.659	80.11	29.21
4.033	66.16	3.81			

Table E.4: Measured data for the mass mean diameter distributions of the modified pressure-swirl atomizer (Insert # 1) without acoustics. z = 203.2 mm (8 inches). Figures 5.17 and 5.18.

Velocity (m/s)	$D_{30}(\mu m)$	x (mm)	Velocity (m/s)	D_{30} (μm)	x (mm)
1.288	92.74	-24.13	5.263	72.43	3.81
1.412	91.83	-21.59	4.979	70.38	6.35
1.636	88.58	-19.05	4.713	70.10	8.89
2.083	85.62	-16.51	4.259	71.06	11.43
2.645	82.23	-13.97	3.820	72.61	13.97
3.169	79.26	-11.43	3.585	74.42	16.51
3.491	76.53	-8.89	2.946	78.88	19.05
3.723	74.08	-6.35	2.758	78.73	21.59
4.249	74.26	-3.81	2.556	78.67	24.13
4.740	74.35	-1.27	2.147	81.91	26.67
5.039	73.59	1.27			

Table E.5: Measured data for the mass mean diameter distributions of the modified pressure-swirl atomizer (Insert # 2) without acoustics. z = 203.2 mm (8 inches). Figures 5.17 and 5.18.

Velocity (m/s)	$D_{30}(\mu m)$	x (mm)	Velocity (m/s)	D_{30} (μm)	x (mm)
2.092	88.96	-16.51	5.690	71.28	3.81
3.029	81.02	-13.97	5.502	70.80	6.35
2.948	83.82	-11.43	5.327	71.42	8.89
3.648	78.83	-8.89	4.880	73.37	11.43
4.336	77.78	-6.35	4.430	76.32	13.97
4.824	76.48	-3.81	3.447	79.42	16.51
5.149	74.41	-1.27	3.266	77.97	19.05
5.608	73.30	1.27			

Table E.6: Measured data for the mass mean diameter distributions of the modified pressure-swirl atomizer (Insert # 3) without acoustics. z = 203.2 mm (8 inches). Figures 5.17 and 5.18.

Class	Size Range	Counts	Concentration	Flux	Uvel
	(μm)		(counts/cc)	(cc/s/cm^2)	(m/s)
0	0 - 2.17	1	1.63E-01	9.50E-10	10.855
1	2.17 - 4.35	0	0.00E+00	0.00E+00	0
2	4.35 - 6.52	0	0.00E+00	0.00E+00	0
3	6.52 - 8.7	1	2.30E-01	1.02E-07	12.909
4	8.7 - 10.87	0	0.00E+00	0.00E+00	0
5	10.87 - 13.04	2	1.44E-01	2.56E-07	15.239
6	13.04 - 15.22	1	2.95E+01	1.81E-06	0.332
7	15.22 - 17.39	6	2.22E+00	2.56E-06	4.182
8	17.39 - 19.57	5	4.75E+01	1.24E-05	0.663
9	19.57 - 21.74	41	4.72E+01	3.57E-05	1.407
10	21.74 - 23.92	123	3.25E+02	2.12E-04	0.91
11	23.92 - 26.09	501	1.71E+03	1.25E-03	0.787
12	26.09 - 28.26	1275	4.36E+03	3.77E-03	0.733
13	28.26 - 30.44	2374	5.73E+03	7.11E-03	0.841
14	30.44 - 32.61	2493	4.12E+03	7.26E-03	0.971
15	32.61 - 34.79	2598	3.39E+03	8.16E-03	1.093
16	34.79 - 36.96	2507	2.20E+03	7.73E-03	1.327
17	36.96 - 39.13	2286	1.67E+03	7.68E-03	1.465
18	39.13 - 41.31	2341	1.27E+03	8.42E-03	1.801
19	41.31 - 43.48	1779	6.92E+02	6.52E-03	2.186
20	43.48 - 45.66	1493	3.92E+02	5.46E-03	2.798
21	45.66 - 47.83	1283	2.33E+02	4.74E-03	3.542
22	47.83 - 50.01	1285	2.07E+02	5.12E-03	3.78
23	50.01 - 52.18	948	1.12E+02	3.91E-03	4.683
24	52.18 - 54.35	830	8.24E+01	3.73E-03	5.376
25	54.35 - 56.53	722	6.23E+01	3.53E-03	5.989

Table E.7: Measured data for the diameter distributions of the modified pressure-swirl atomizers (insert #1) at the edge of radial locations. x = -11.43 mm (-0.45 inches), z = 25.4 mm (1 inch). Figure 5.19.

...continued from the previous table

Class	Size Range	Counts	Concentration	Flux	Uvel
	(μm)		(counts/cc)	(cc/s/cm^2)	(m/s)
26	56.53 - 58.7	617	4.37E+01	3.09E-03	6.679
27	58.7 - 60.88	615	4.08E+01	3.34E-03	6.928
28	60.88 - 63.05	487	2.84E+01	2.92E-03	7.836
29	63.05 - 65.22	435	2.29E+01	2.72E-03	8.194
30	65.22 - 67.4	400	2.14E+01	2.82E-03	8.218
31	67.4 - 69.57	414	2.07E+01	3.27E-03	8.96
32	69.57 - 71.75	320	1.51E+01	2.71E-03	9.26
33	71.75 - 73.92	283	1.20E+01	2.46E-03	9.698
34	73.92 - 76.1	249	1.06E+01	2.41E-03	9.897
35	76.1 - 78.27	231	9.82E+00	2.44E-03	9.91
36	78.27 - 80.44	212	8.39E+00	2.35E-03	10.273
37	80.44 - 82.62	175	7.00E+00	2.19E-03	10.576
38	82.62 - 84.79	141	5.41E+00	1.89E-03	10.932
39	84.79 - 86.97	114	4.20E+00	1.64E-03	11.326
40	86.97 - 89.14	109	4.44E+00	1.79E-03	10.853
41	89.14 - 91.31	79	3.03E+00	1.32E-03	10.904
42	91.31 - 93.49	48	1.71E+00	8.09E-04	11.047
43	93.49 - 95.66	40	1.50E+00	7.67E-04	11.18
44	95.66 - 97.84	34	1.32E+00	7.61E-04	11.755
45	97.84 - 100.01	27	1.09E+00	6.39E-04	11.241
46	100.01 - 102.19	12	4.25E-01	2.96E-04	12.475
47	102.19 - 104.36	18	8.44E-01	6.05E-04	12.044
48	104.36 - 106.53	27	1.09E+00	7.60E-04	11.06
49	106.53 - 108.71	15	5.74E-01	4.52E-04	11.7

Table E.8: Measured data for the diameter distributions of the modofied pressure-swirl atomizers (insert #1) at the edge of radial locations. x = -11.43 mm (-0.45 inches), z = 25.4 mm (1 inch). Figure 5.19.

Class	Size Range	Counts	Concentration	Flux	Uvel
	(μm)		(counts/cc)	(cc/s/cm^2)	(m/s)
0	0 - 2.17	1	3.60E-02	2.74E-10	14.137
1	2.17 - 4.35	0	0.00E+00	0.00E+00	0
2	4.35 - 6.52	1	1.75E-01	3.65E-08	14.312
3	6.52 - 8.7	4	3.82E-01	1.92E-07	14.619
4	8.7 - 10.87	15	1.49E+00	1.36E-06	13.532
5	10.87 - 13.04	48	4.58E+00	6.10E-06	11.463
6	13.04 - 15.22	249	2.37E+01	4.88E-05	11.169
7	15.22 - 17.39	576	4.43E+01	1.34E-04	10.976
8	17.39 - 19.57	1139	7.19E+01	3.18E-04	11.282
9	19.57 - 21.74	1638	8.71E+01	5.39E-04	11.5
10	21.74 - 23.92	1562	7.00E+01	5.97E-04	11.902
11	23.92 - 26.09	1461	5.86E+01	6.67E-04	12.235
12	26.09 - 28.26	1398	4.93E+01	7.35E-04	12.625
13	28.26 - 30.44	1392	4.47E+01	8.61E-04	13.04
14	30.44 - 32.61	1144	3.34E+01	8.25E-04	13.594
15	32.61 - 34.79	1019	2.81E+01	8.54E-04	13.803
16	34.79 - 36.96	972	2.64E+01	9.86E-04	14.104
17	36.96 - 39.13	1017	2.61E+01	1.18E-03	14.395
18	39.13 - 41.31	1082	2.78E+01	1.49E-03	14.473
19	41.31 - 43.48	957	2.38E+01	1.50E-03	14.667
20	43.48 - 45.66	893	2.13E+01	1.59E-03	14.949
21	45.66 - 47.83	943	2.21E+01	1.90E-03	14.998
22	47.83 - 50.01	1002	2.29E+01	2.29E-03	15.258
23	50.01 - 52.18	851	1.94E+01	2.23E-03	15.488
24	52.18 - 54.35	819	1.85E+01	2.40E-03	15.434
25	54.35 - 56.53	767	1.68E+01	2.52E-03	15.829

Table E.9: Measured data for the diameter distributions of the modified pressure-swirl atomizers (insert # 1) at the centerline. $x = 0$, $z = 25.4$ mm (1 inch). Figure 5.20.

...continued from the previous table

Class	Size Range	Counts	Concentration	Flux	Uvel
	(μm)		(counts/cc)	(cc/s/cm^2)	(m/s)
26	56.53 - 58.7	714	1.57E+01	2.62E-03	15.825
27	58.7 - 60.88	780	1.66E+01	3.17E-03	16.23
28	60.88 - 63.05	644	1.38E+01	2.90E-03	16
29	63.05 - 65.22	609	1.33E+01	3.18E-03	16.408
30	65.22 - 67.4	555	1.19E+01	3.12E-03	16.324
31	67.4 - 69.57	638	1.39E+01	4.07E-03	16.565
32	69.57 - 71.75	531	1.14E+01	3.67E-03	16.716
33	71.75 - 73.92	482	1.05E+01	3.67E-03	16.447
34	73.92 - 76.09	507	1.10E+01	4.24E-03	16.718
35	76.09 - 78.27	513	1.13E+01	4.71E-03	16.55
36	78.27 - 80.44	483	1.07E+01	4.97E-03	16.999
37	80.44 - 82.62	456	1.03E+01	5.19E-03	17.143
38	82.62 - 84.79	417	9.04E+00	4.90E-03	16.981
39	84.79 - 86.97	337	7.05E+00	4.14E-03	17.082
40	86.97 - 89.14	326	7.51E+00	4.75E-03	17.057
41	89.14 - 91.31	230	5.33E+00	3.65E-03	17.175
42	91.31 - 93.49	167	3.75E+00	2.70E-03	16.792
43	93.49 - 95.66	146	3.54E+00	2.75E-03	16.938
44	95.66 - 97.84	134	3.48E+00	2.89E-03	16.908
45	97.84 - 100.01	105	2.56E+00	2.33E-03	17.381
46	100.01 - 102.18	82	1.93E+00	1.82E-03	16.919
47	102.18 - 104.36	64	1.56E+00	1.60E-03	17.32
48	104.36 - 106.53	67	1.87E+00	2.00E-03	16.867
49	106.53 - 108.71	49	1.21E+00	1.38E-03	17.012

Table E.10: Measured data for the diameter distributions of the modified pressure-swirl atomizers (insert # 1) at the centerline. $x = 0$, $z = 25.4$ mm (1 inch). Figure 5.20.

Frequency kHz	$x = -10.16$ mm	$x = -5.08$ mm	$x = 0$ mm	$x = 5.08$ mm	$x = 10.16$ mm
0	59.68	60.66	60.94	60.29	65.15
1	61.24	60.97	61.13	61.86	64.55
2	60.69	61.32	61.11	61.01	66.03
3	59.81	60.64	61.04	61.05	64.16
4	59.77	60.84	60.65	60.98	65.33
5	60.46	60.71	60.84	60.94	64.52
6	61.00	60.93	61.25	60.84	64.61
7	60.49	61.23	60.83	61.08	64.58
8	60.98	60.90	61.24	60.81	64.69
9	62.88	60.34	62.01	60.92	64.98
10	59.77	60.16	61.51	60.81	65.13
11	61.53	60.22	61.24	61.23	64.98
12	61.81	60.22	61.65	61.01	65.16
13	59.57	60.11	61.17	60.82	65.07
14	59.96	60.63	60.65	61.17	65.10
15	61.56	60.44	61.39	60.83	65.14

Table E.11: Measured data of the mass mean diameter for the modified pressure-swirl atomizer (insert # 1) at different radial locations with acoustics (power level 3). $z =$ 203.2 mm (8 inches). Figure 5.21.

Frequency kHz	$x = -10.16$ mm	$x = -5.08$ mm	$x = 0$ mm	$x = 5.08$ mm	$x = 10.16$ mm
0	72.21	63.11	59.84	60.32	64.98
1	72.03	63.64	59.88	61.05	66.09
2	71.87	63.44	59.41	60.79	65.51
3	71.20	63.39	59.64	59.85	65.45
4	72.83	64.07	59.54	59.94	65.26
5	71.20	63.90	59.25	60.37	64.89
6	71.78	63.72	59.62	60.06	65.07
7	70.56	62.91	59.30	59.88	64.81
8	71.80	63.01	59.57	60.10	65.23
9	69.48	62.97	59.43	59.35	64.23
10	72.17	63.01	59.64	60.17	64.10
11	71.86	63.70	59.08	60.08	63.38
12	72.70	63.41	59.47	61.07	64.49
13	72.83	64.11	59.20	61.15	64.24
14	72.52	63.14	58.92	60.38	64.60
15	71.33	63.32	59.28	60.75	63.98

Table E.12: Measured data of the mass mean diameter for the modified pressure-swirl atomizer (insert # 2) at different radial locations with acoustics (power level 3). $z =$ 203.2 mm (8 inches). Figure 5.22.

Frequency kHz	$x = -10.16$ mm	$x = -5.08$ mm	$x = 0$ mm	$x = 5.08$ mm	$x = 10.16$ mm
0	63.64	59.83	61.77	61.58	67.52
1	64.43	59.75	62.12	60.93	66.99
2	63.53	60.28	62.39	61.57	68.19
3	64.00	60.27	61.85	61.86	67.92
4	64.58	60.89	61.35	61.53	67.51
5	66.92	60.09	61.29	61.61	67.91
6	65.85	59.60	60.43	61.65	68.07
7	65.89	60.00	60.12	61.94	68.10
8	65.00	61.08	60.86	62.17	68.79
9	64.99	59.81	61.27	61.57	65.81
10	65.20	59.37	60.48	61.68	66.38
11	66.54	58.89	60.26	63.00	65.62
12	65.71	59.38	60.13	62.31	66.20
13	64.15	61.05	60.19	60.54	65.70
14	64.18	59.28	59.90	61.99	66.30
15	64.34	60.42	59.97	62.59	67.07

Table E.13: Measured data of the mass mean diameter for the modified pressure-swirl atomizer (insert # 3) at different radial locations with acoustics (power level 3). $z =$ 203.2 mm (8 inches). Figure 5.23.

Frequency	Insert # 1	Insert # 2	Insert # 3
0	60.95	62.56	62.11
1	61.72	63.13	62.13
2	61.58	62.52	62.32
3	61.16	62.41	62.40
4	61.12	62.45	62.40
5	61.17	62.54	62.42
6	61.41	62.52	61.84
7	61.35	61.93	62.03
8	61.38	62.17	62.63
9	61.82	61.75	61.99
10	61.12	62.28	61.64
11	61.49	62.07	61.71
12	61.59	62.69	61.63
13	60.98	62.56	61.54
14	61.11	62.26	61.33
15	61.46	62.43	61.90

Table E.14: Line-averaged data of the mass mean diameters for the modified pressure-swirl atomizer (insert # 1, 2, and 3) as a function of the acoustic frequency (power level 3). $z = 203.2$ mm (8 inches). Figure 5.24.

Appendix F

Measured Data for Chapter 6

x (mm)	x (inch)	D_{10} (μm)	D_{20} (μm)	D_{30} (μm)
-50.8	-2	35.26	40.34	44.88
-40.64	-1.6	35.88	40.85	45.28
-30.48	-1.2	36.64	41.53	45.87
-20.32	-0.8	36.91	41.78	46.1
-10.16	-0.4	36.29	41	45.17
0	0	36.96	41.52	45.52
10.16	0.4	36.22	41.11	45.43
20.32	0.8	36.93	41.88	46.25
30.48	1.2	35.55	40.58	45.06
40.64	1.6	35.15	40.12	44.55
50.8	2	34.28	39.32	43.87
60.96	2.4	35.06	40.41	45.22

Table F.1: Mass mean diameter distributions along the radial locations of the spray created by the new-concept impaction atomizer. Impaction angle: 65°; impaction length: 50.8 mm (2 inches); z = 203.2 mm (8 inches). Figure 6.5.

Angle	50	55	60	65	70	75
D_{30}	51.0545	47.6709	45.8156	45.3735	48.8009	48.1919
D_{32}	69.4987	57.9878	56.2294	55.5588	57.5238	55.5588

Table F.2: Line-averaged data for the mean diameter as a function of the impaction angle of the new-concept impaction atomizer. Impaction length: 50.8 mm (2 inches); z = 203.2 mm (8 inches). Figure 6.6.

x (mm)	x (inch)	D_{10} (μm)	D_{20} (μm)	D_{30} (μm)
-121.92	-4.8	35.69	41.03	45.68
-106.68	-4.2	36.92	42.56	47.36
-91.44	-3.6	38.14	43.84	48.68
-76.2	-3	38.14	43.84	48.68
-60.96	-2.4	38.55	44.34	49.21
-45.72	-1.8	37.85	43.6	48.47
-30.48	-1.2	37.25	43.04	47.94
-15.24	-0.6	37.83	43.58	48.42
0	0	37.97	43.55	48.26
15.24	0.6	38.44	43.91	48.53
30.48	1.2	37.72	43.15	47.74
45.72	1.8	37.24	42.56	47.11
60.96	2.4	36.41	41.98	46.76
76.2	3	37.14	42.96	47.46
91.44	3.6	35.12	40.73	45.61
106.68	4.2	34.4	39.98	44.9

Table F.3: Mass mean diameter distributions along the radial locations of the spray created by the new-concept impaction atomizer. Impaction angle: 60°; impaction length: 50.8 mm (2 inches); z = 203.2 mm (8 inches). Figure 6.7.

Impaction length (mm)	50.8	63.5	76.2	88.9	101.6	114.3	127.0
D_{30}	47.7144	48.0878	48.1090	48.8883	50.1022	50.6471	51.5390
D_{32}	58.9105	59.0583	59.0893	60.0072	61.2726	61.9737	63.1082

Table F.4: Line-averaged data for the mean diameter as a function of the impaction length of the new-concept impaction atomizer. Impaction angle: 60°; $z = 203.2$ mm (8 inches). Figure 6.8.

VITA

Surname: Chen — Given Names: Tingbao

Place of Birth: Weifang, Shandong, P. R. China — Date of Birth: February 12, 1962

Educational Institutions Attended:

University of Victoria, Canada	1995 to 1997
Beijing Agricultural Engineering University (BAEU)	1979 to 1983

Degrees Awarded:

B.Eng. (Honours)	BAEU	1983

Honours and Awards:

Scholarship	CAIEP[2]	1994–1995
Fellowship	BAEU	1979–1983

Publications:

1. Tingbao Chen and Xianguo Li, **Liquid Jet Atomization in a Compressible Gas Stream**, submitted to *Transactions of Royal Society of London* for publication.

2. Tingbao Chen and Xianguo Li, **Liquid Jet Atomization in a Compressible Gas Stream**, *Proceedings of ASME - Energy Week*, January 28 - 30, 1997, Houston, Texas, U. S. A., Book V, Vol. VIII, pp. 395 - 399.

3. Tingbao Chen and X. Li, **Gas Compressibility Effect on Three-Dimensional Liquid Jet Instability**, *Proceedings of First Trabzon International Energy and Environments Symposium*, July 29 - 31, 1996, Trabzon, Turkey, Vol. 2, pp. 707 - 714.

[2]Scholarship of US$10,000 sponsored by China Association for International Exchange of Personnel.

PARTIAL COPYRIGHT LICENSE

I hereby grant the right to lend my thesis to users of the University of Victoria Library, and to make single copies only for such users or in response to a request from the Library of any other university, or similar institution, on its behalf or for one of its users. I further agree that permission for extensive copying of this thesis for scholarly purposes may be granted by me or a member of the University designated by me. It is understood that copying or publication of this thesis for financial gain shall not be allowed without my written permission.

Title of Thesis:

LIQUID ATOMIZATION FOR AEROSOL APPLICATIONS

Author: [redacted]

Tingbao Chen

July 4, 1997

Date